Spring 2021

Mechanisms by which Metaflammation and Adiponectin Regulates Glucose and Lipid Metabolism

Xiruo Li
Yale University Graduate School of Arts and Sciences, xiruoli07@gmail.com

Abstract

Mechanisms by which Metaflammation and Adiponectin Regulates Glucose and Lipid Metabolism

Xiruo Li

2021

Obesity and Type 2 Diabetes mellitus (T2DM) are among the most serious global health problems as they are increasing in prevalence and related to many chronic diseases, including cardiovascular and cerebrovascular diseases, cancer and other metabolic disorders. Obesity increases the risk for T2DM through the development of low-grade inflammation and insulin resistance. Specifically, studies have shown that enhanced inflammation in adipose tissue is an essential player in the progression of insulin resistance and T2DM in obese individuals. However, how immune cells sense nutritional status and contribute to whole-body metabolism are largely unknown. In addition, most of the currently available therapies do not address the root cause of T2DM: insulin resistance. Pharmacological agents that improve diabetes have limited success due to side effects and decline in efficacy as most patients develop resistance over time. As such, understanding the pathogenesis of T2DM and finding new interventions to ameliorate insulin resistance are of great interest.

In this doctoral dissertation, I describe work that elucidates the nutritional regulation of macrophage function and its contribution to whole-body metabolism, as well as the mechanisms by which a new potential treatment, adiponectin, ameliorates insulin resistance. Protein O-GlcNAcylation is thought to be a metabolic sensor that modulates cell signaling. I showed that overnutrition stimulated nutrient-sensing O-linked β-N-acetylglucosamine (O-GlcNAc) signaling in macrophages and O-GlcNAc signaling was down-regulated during macrophage pro-inflammatory polarization. Further, mice with O-

GlcNAc transferase (Ogt) deletion in macrophages and other myeloid cells displayed enhanced macrophage pro-inflammatory activation in adipose tissue and lipolysis, increased ectopic lipid accumulation in peripheral tissues, and exacerbated tissue-specific and whole-body insulin resistance in diet-induced obese mice. O-GlcNAc signaling inhibited macrophage pro-inflammatory polarization by catalyzing ribosomal protein S6 kinase beta-1 (S6K1) serine 489 O-GlcNAcylation and suppressing S6K1 phosphorylation. These studies uncovered O-GlcNAc signaling as a novel homeostatic regulator at the interface of inflammation and metabolism and suggested that O-GlcNAc signaling may serve as a therapeutic target for obesity, diabetes, and other immune-related diseases.

Finally, I examined the mechanisms for the anti-diabetic effect of adiponectin. Adiponectin has emerged as a promising insulin-sensitizing adipokine and a potential therapy to treat T2DM; however, the mechanisms by which adiponectin administration improves insulin sensitivity were unclear. To address this question, I examined the effects of a 2-week continuous subcutaneous infusion of globular adiponectin (gAcrp30) or saline on glucose and lipid metabolism in a high-fat diet (HFD) fed mouse model. Whole-body and tissue-specific insulin action was assessed by a hyperinsulinemic-euglycemic clamp (HEC). gAcrp30-treated mice displayed reduced fasting plasma glucose and insulin concentrations and increased glucose infusion rate during the HEC, reflecting increased whole-body insulin sensitivity. Increased insulin sensitivity could be attributed to reduced endogenous glucose production and increased glucose uptake in muscle and adipose tissues. We found that these liver and muscle sensitivity improvements were associated with reductions in the plasma membrane-associated diacylglycerol (DAG) content, and contrary to prior studies, were independent of reductions in total ceramide content. These effects in turn led to decreased protein kinase Cε (PKCε) activation in liver, decreased PKCε/PKCθ activity in muscle, and improved insulin signaling in these tissues. I further demonstrated that globular adiponectin (gAcrp30) and full-length adiponectin (Acrp30)

reverse insulin resistance in HFD-fed mice through reductions in ectopic lipid in liver and muscle likely by stimulation of lipoprotein lipase (LPL) activity in white adipose tissue and increased epithelial nitric oxide synthase (eNOS)/ 5' AMP-activated protein kinase (AMPK) activation and fat oxidation in muscle.

Taken together, the work presented in the dissertation provides novel mechanistic insight into the regulation and function of O-GlcNAc signaling in the immunometabolism and the mechanisms by which adiponectin reverses HFD-induced liver and muscle insulin resistance in mice. As such, adiponectin and O-GlcNAc signaling activators, such as glutamine and glucosamine, could serve as viable treatment options for T2DM, insulin resistance and other obesity-associated morbidities.

Mechanisms by which Metaflammation and Adiponectin Regulates Glucose and Lipid Metabolism

A Dissertation
Presented to the Faculty of the Graduate School
of
Yale University
in Candidacy for the degree of
Doctor of Philosophy

by
Xiruo Li

Dissertation Director: Gerald I. Shulman

Dissertation Committee Chairman: Rachel Jamison Perry

June 2021

TABLE OF CONTENTS

ACKNOWLEDGMENTS

The Ph.D. study is a long and challenging journey, which requires many collaborations. This dissertation could not have come to its fruition without the generous support and help from other people. I am always grateful to many people who have enabled and enriched my journal:

I would love to express my sincerest gratitude to my advisor, Gerald Shulman, for his extraordinary mentorship and everything he has done to support my research and future career. Dr. Shulman not only taught me how to develop my research projects, but also shaped me to become a great scientist. He loves communicating with students and is always passionate about science and encouraged me a lot during those challenging moments in research that every scientist face at some point. I am also grateful for his support when I started exploring my future career. He always gives students the freedom to explore new possibilities and opportunities in their lives. I am very grateful to have had the opportunity to spend five years in his lab.

I am incredibly grateful to my thesis committee, Drs. Rachel Jamison Perry, Varman Samuel and Matthew Rodeheffer, to my DGS, David Zenisek, and to my outside reader, Dr. Ira Goldberg. Rachel is one of the most outstanding women scientists. She always gives me a hand whenever I need help and provides me with a lot of insightful feedback for my research. She also gave me lots of guidance in my scientific writing and helped me revise a lot of grammar mistakes I made. Her warm and uplifting words always encouraged me when I failed in my experiments. Varman is one of my models as a physician-scientist. He led me to open the door of the scientific research as early as the qualifying exam and taught me how to critically review scientific articles. He always asks me a lot of intriguing but sharp questions in my committee meeting, which I really need to think very hard to get answers. However, these questions turned out to be very critical in

the development of my research. Matt is always willing to provide help for my research and career. I remembered that I went to his lab to ask for help and he spent a lot of time teaching me how to analyze flow cytometry data. And his excellent expertise in adipose tissue shed new light on my experiments. David is very responsible, caring about graduate students and always taking time to attend everyone's committee meetings and defenses. I also want to thank my outside reader Ira for taking the time out of his busy schedule to read my thesis and attend my defense. Their guidance, support and insightful feedback have been invaluable to my Ph.D. study and my future career. I really learned a lot from them, and I appreciated their help and time along the journey.

I also want to thank my dearest friends and colleagues in Shulman lab, past and present, for their continuous assistance, support and guidance. Daniel F. Vatner was my rotation mentor and the intellectual father of my scientific research. I am grateful to Dan for his willingness to take the time to answer my questions and for mentoring me in a proper way to do science. I am also grateful to Leigh Goedeke for her kind assistance, thoughtful suggestions and stimulating discussions. She taught me several new techniques and help me revise my proposal and manuscript. Then I want to thank Kitt. She is a very warm person and really cares about my research and life. She always asks a lot of intriguing questions when I presented my research. Wanling Zhu has done a lot of mice surgeries for me and helped me a lot with my animal experiments. I would also love to thank Dongyan Zhang, Ali Nasiri, Mario Kahn, Gary Cline, Xian-Man Zhang, Panu Luukkonen, Gina Butrico and Ye Zhang for teaching me various experimental techniques with patience and providing me technical assistance whenever needed. I then want to thank my dear fellows, Kun Lyu, Brandon Hubbard, and Traci LaMoia. They are my "brothers in arms" and we encouraged and inspired each other during any difficult time. They are also very important friends of mine.

Many thanks to the many other scientists who offered me assistance and opportunity, to Yale University and the Department of Cellular and Molecular Physiology. To Xiaoyong Yang and Yunfan Yang, who allowed me to join an extremely interesting project and it was a great pleasure to work as a team. Their willingness to share their expertise complemented our lab's expertise and added another dimension to my training. I have much enjoyed the experience and learned a lot from Yunfan and other collaborators. To Michael Caplan and Emile Boulpaep, who provided new insights into my projects and asked me the tough question. To Jessie Rinehart, who helped me find potential binding proteins of adiponectin. Although the experiment didn't succeed in the end for some reason, I still want to thank him for his generous help. To all the other faculties, postdocs and other graduate students, who have fostered an extraordinary academic environment. Joining the physiology department is a very wise choice. That is not only because we had fancy dinners and several lunches with student-invited speakers each year, but I also got a lot of invaluable feedback from our faculties in the private sections after each RIP talk. We also had different career panels to explore different career paths. I have been provided with tremendous opportunities to learn, to improve and to grow in the physiology department. Last but not least, I would like to extend these thanks to my department's registrar, Leisa Strohmaier, who is always willing to assist me with my Ph.D. study.

On a personal note, I am grateful to my parents, Shuying and Zhihui. It is a huge source of comfort to know how much I am genuinely loved. Thank you for always supporting every decision I made and encouraging me to try different things and become a better me. It feels awesome to have a strong safety net! I would love to thank my friends who are always around me, helped me celebrate the victories and overcome difficulties during the Ph.D. study. My dear friends, Yiyun Cao, Peiqi Li, Runfeng Miao, Naijia Liu, Chen Chen, Sisi Zhou, Wenrui Li, Jun Zhao, Chao Zhang, Weiwei Han and so many others to name, have been my lights and brightened my view. I would love to thank my casing

partners and my friends, Daniel E. DeRosha, Ming Chen, Alisia Botthof, Woo Young Cho, Sol Bernardez Sarria and Colleen Lopez, for their kindness, support, and generosity. We spent a lot of time preparing job interviews. Without help from them, I cannot successfully land a job.

Last but not least, I want to thank my fiancé, Qisong Ren. We have known each other since high school and have been together for almost nine years. He is my knight in shining armor and my personal Superman. Whenever I need a hero, he comes in to save the day. When I thought I couldn't go on any longer, he gave me the strength I needed to keep moving forward. I want to thank him for every time he supported me and stood by my side, not only when I was faced with academic difficulties, but also when I was trying to prepare for my job interview. Words cannot fully express my feeling. I am so looking forward to starting the next new chapter, because I know he is there.

CHAPTER 1

Introduction to Obesity and Insulin Resistance

Obesity and Type 2 Diabetes mellitus (T2DM) are two of the major healthcare burdens of the 21st century, with an incidence that increases yearly (1). Obesity has almost tripled globally since the 1970s (2). More than 1.9 billion adults (40% of the world adult population) were overweight and more than 650 million were categorized as obese (3). T2DM currently affects more than 30.3 million people in the United States and the prevalence of diabetes is growing rapidly, mirroring an increase in the prevalence of obesity and overweight people **(Fig. 1)**. As the incidence and prevalence of diabetes continue to rise, the Centers for Disease Control and Prevention estimate one in three Americans will suffer from T2DM by 2050 (4). Obesity serves as an important risk factor for the development of numerous diseases, including T2DM, non-alcoholic fatty liver disease (NAFLD), cardiovascular diseases (CVD), more than one dozen cancers and some immune-related disorders. Insulin resistance plays a critical role in the pathogenesis of T2DM and other obesity-related diseases, such as NAFLD and CVD (5-7). As such, understanding the pathogenesis of insulin resistance and finding effective therapies have become essential to treat T2DM and obesity-related diseases.

Chronic obesity-associated inflammation, particularly in adipose tissue and liver, has been widely reported as a significant pathogenic factor associated with insulin resistance and T2D in both rodents and humans (8-10). In obese subjects, adipose tissue is enriched with pro-inflammatory immune cells such as macrophages and lymphocytes (8). These immune cells secrete excessive cytokines such as IL-6 and TNFα which have been shown to have lipolytic effects and increase ectopic lipid accumulation in insulin-responsive tissues (9, 11, 12). The relationship between chronic low-grade obesity-associated inflammation (metaflammation) and insulin resistance will be explored in Chapter 2.

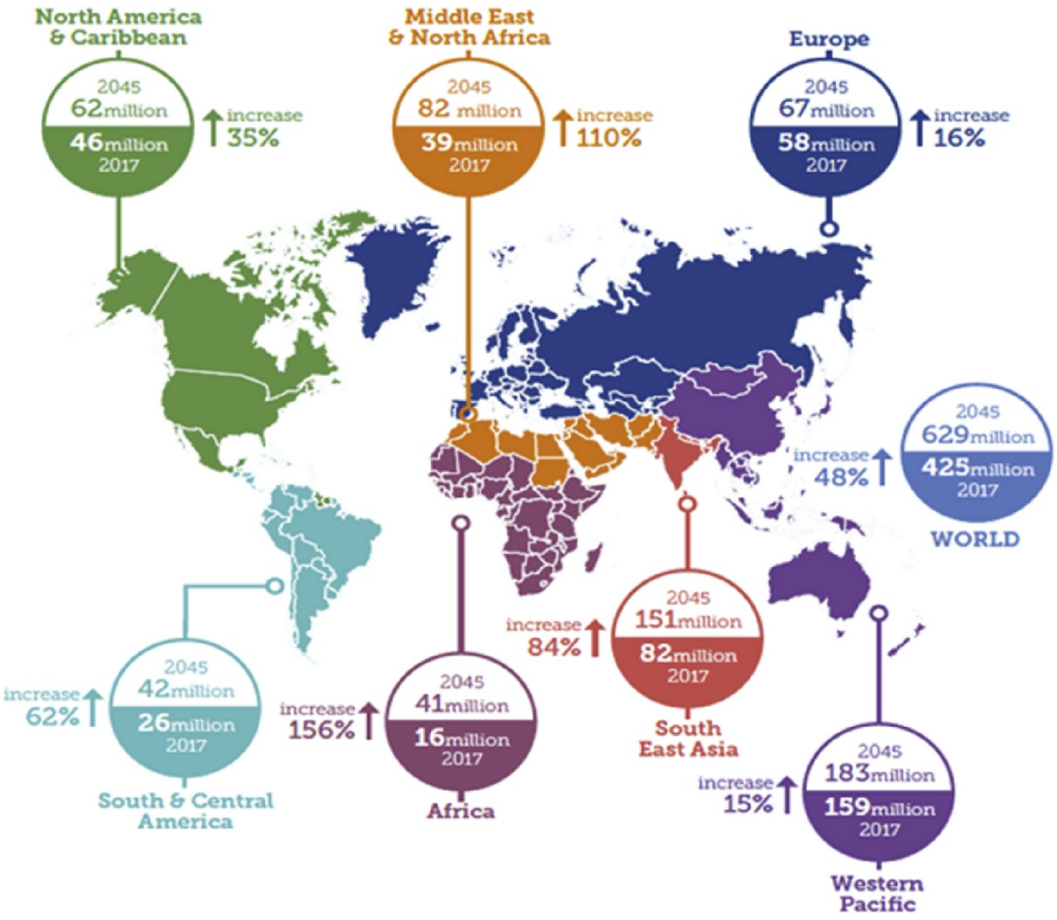

Figure 1. Number of people with diabetes worldwide and per region in 2017 and 2045 (20–79 years) (http://diabetesatlas.org/).

The association between ectopic lipids and insulin resistance is widely accepted (13-15). Although studies in normal weight, non-diabetic adults found that triglyceride (TAG) content was a stronger predictor of insulin resistance than circulating fatty acid in soleus muscle (16), experiments showed that TG concentrations are dissociated from insulin resistance (7, 16). One hypothesis proposed that its precursor, DAG may induce insulin resistance. Increased DAG level impairs insulin action via activation and membrane translocation of protein kinase Cε (PKCε) in liver(17, 18) and both PKCε and PKCθ in skeletal muscle, which will impair subsequent insulin receptor kinase (IRK) activity (14, 19, 20). Hepatic insulin resistance will lead to reduced suppression of gluconeogenesis and insulin resistance in muscle will result in reduced glucose uptake. In addition to liver and muscle, insulin resistance develops in white adipose tissue (WAT). In this condition, insulin fails to suppress WAT lipolysis, which will lead to increased free fatty acid delivery into liver and muscle to further raise TAG and DAG levels (6, 7). In addition to the direct effect of insulin, experiments from our laboratory have shown that fasting hyperglycemia in rodent models of T2D is caused by inappropriate increases in hepatic gluconeogenesis in the setting of increased white adipose tissue (WAT) lipolysis and increased glycerol and acetyl CoA delivery to the liver (9). Increased conversion of glycerol to glucose is driven by a substrate push mechanism and conversion of pyruvate to glucose is increased through allosteric activation of pyruvate carboxylase (PC) by acetyl CoA. Published papers regarding the insulin signaling and lipid-induced insulin resistance will be reviewed in Chapter 3.

Mitigating insulin resistance and achieving normoglycemia is a critical objective in the treatment of T2DM, which would reduce the risk of diabetes-associated complications (21, 22). Adiponectin has emerged as an anti-diabetic, anti-inflammatory and anti-atherogenic adipokine(23, 24). Adiponectin is an adipokine mostly secreted by adipose tissue. Studies in humans and monkeys showed that plasma adiponectin levels correlate

significantly with whole-body insulin sensitivity (25, 26). Overexpression or administration of adiponectin results in a decrease in hyperglycemia and improvement in systemic insulin sensitivity (23, 27), whereas adiponectin-deficient mice exhibit impaired insulin sensitivity and diabetes (24, 28). As such, adiponectin may serve as a viable treatment option for T2DM, insulin resistance and other obesity-related diseases. The current available therapies to treat T2DM and the proposed mechanisms of adiponectin's anti-diabetic effect will be discussed in Chapter 4.

With the context provided above, the remainder of the dissertation will describe the original research I conducted during my PhD that fulfilled the doctoral requirements of the Yale University Graduate School of Arts and Sciences. The research project to study how immune cells, especially macrophages in adipose tissues, sense nutritional clues and contribute to the whole-body metabolism will be described in Chapter 5. In this project, I used a novel O-GlcNAc transferase^{flox} (*Ogt*^{flox}) *LyzM*-Cre+/- (OGT MKO) mouse model by crossing *Ogt*^{flox} mice (provided by Dr. Steven Jones) with *LyzM*-Cre mice. Dr. Steven Jones' group found that although OGT deletion in cardiomyocyte did not cause any significant functional change in sham-operated mice, infarcted cardiomyocyte OGT KO mice and long-term OGT loss in cardiomyocyte significantly exacerbated cardiac dysfunction compared with WT (29, 30). This project reveals an intrinsic mechanism maintaining adipose tissue and whole-body metabolic homeostasis during overnutrition through macrophage O-GlcNAc signaling. Chapter 6 will describe a novel mechanism by which adiponectin reverses insulin resistance in high-fat diet fed mice, providing important therapeutic implications for treating insulin resistance and T2DM. Finally, Chapter 7 will summarize the whole dissertation research in a broader context and point out potential directions for future studies.

CHAPTER 2

Chronic Low-grade Inflammation in Adipose Tissues Links Obesity to Insulin Resistance and Type 2 Diabetes

In obesity, the chronic low-grade metabolic inflammation (metaflammation) develops in multiple organs such as adipose (31, 32), liver (33, 34), skeletal muscle (35, 36), pancreas (37, 38), brain (39, 40) and gut (41, 42) and is defined by increased infiltration and activation of innate and adaptive immune cells. Adipose tissue inflammation, the major and most well-characterized form of metaflammation, negatively impacts whole-body energy homeostasis and has been linked to the development of obesity-induced insulin resistance (32, 43, 44). In obesity, adipose tissue is enriched with pro-inflammatory immune cells such as macrophages (31), neutrophils (45), T cells (46) and B cells (47). These immune cells secrete excessive cytokines such as IL-6 and TNFα which have been shown to have lipolytic effects both in vitro and in vivo (11, 12, 48).

Macrophages, which are the primary immunue cells studied in the dissertation, are the most abundant innate immune cells infiltrating and accumulating into adipose tissues and constitute up to 40% of all adipose tissue cells (8, 49). It is suggested that macrophages are the primary sources of pro-inflammatory cytokines such as IL-6 and TNF-α (7). In obesity, adipose tissue macrophages are polarized into pro-inflammatory macrophages and secrete excessive pro-inflammatory cytokines, leading to increased adipose tissues lipolysis **(Fig. 2)**. Increased lipolysis leads to increased free fatty acid delivery into liver and skeletal muscle to raise TAG and diacylglycerol DAG levels. In addition, increased lipolysis has also been shown to drive increased rate of hepatic gluconeogenesis by increasing acetyl CoA levels as well as glycerol influx, causing fasting hyperglycemia (50).

Besides macrophages, many other immune cells (e.g., neutrophils, dendritic cells, mast cells, B cells, and T cells) reside in adipose tissue during obesity, playing a vital role in the development of adipose tissue inflammation and insulin resistance. Neutrophils are relatively rare in adipose tissue of lean mice (51), but they are the first immune cells recruited to adipose tissues after 3 days of HFD and prolonged for over 90 days (45, 52).

Neutrophils mediate insulin resistance in mice by producing TNF-α, MCP-1 and elastase, which impairs glucose uptake in adipose tissue and degrades IRS-1 (45, 53, 54). Dendritic cells accumulate in adipose tissue of HFD-fed mice and obese humans (55). Dendritic cells have been shown to induce insulin resistance by recruiting macrophages in adipose tissue and increasing pro-inflammatory cytokine IL-6 production (56, 57). Similarly, mast cells infiltrate into adipose tissue and significantly increase in the adipose tissue of mice and humans with obesity and T2DM (58, 59). Mast cells are regulated by IL-6 and IFN-γ but not by TNF-α and they promote inflammation in adipose tissue by mediating macrophage infiltration (58, 60). B cells and T cells also play essential roles in macrophage infiltration and activation (8). B cells in adipose tissue are quite unique and different from B cells found in other tissues (61). B cells significantly increase in the adipose tissue of obese mice and induce insulin resistance by producing chemokines and promoting the recruitment of neutrophils, T cells and macrophages (8, 51). B cells also produce immunoglobulin G antibodies and pro-inflammatory cytokines, which may also lead to increased inflammation in adipose tissue (47, 62). $CD3^+$ T cells are the second largest immune cell population in adipose tissue and are increased in obese mice (8). T cells can be further divided into $CD4^+$ and $CD8^+$ T cells. $CD8^+$ T cells are increased in the adipose tissue and promote chemotaxis and macrophage activation in obesity (46). The abundance of pro-inflammatory $CD3^+CD4^+$ T helper (Th1) cells is increased in obesity, while the number of anti-inflammatory $CD3^+CD4^+$Th2 cells and $CD3^+CD4^+FOXP3^+$ (Treg) cells is reduced, which contribute to increased inflammation and reduced insulin sensitivity (8, 63, 64).

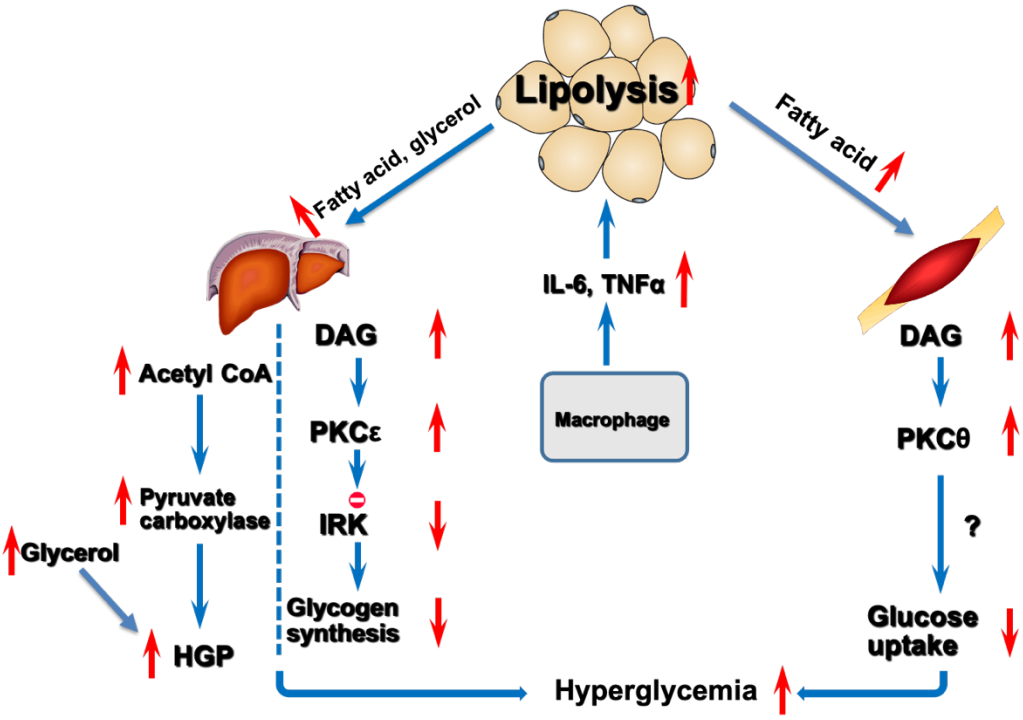

Figure 2. Schematic representations of the metaflammation-lipolysis-insulin resistance model.

Chapter 3

Lipid-Induced Insulin Resistance

It is well known that insulin resistance and T2DM are closely associated with obesity and ectopic lipid accumulation (6, 65). In the early stages of obesity, healthy adipose tissue expansion buffers the excessive calorie intake and limits net energy flow into lean body components such as liver and skeletal muscle. However, in the chronic stage of obesity, disrupted energy buffering capacity of adipose tissue causes energy spillover in the form of accelerated lipolysis, leading to ectopic lipid accumulation and subsequent metabolic syndromes, such as hepatic steatosis and insulin resistance (65).

DAGs and ceramides have emerged as the two best-studied ectopic lipids that have been proposed to mediate lipid-induced insulin resistance (66). DAG is an important intermediate in TAG metabolism and an essential second messenger that can activate PKC. Numerous studies have demonstrated the association between DAG and insulin resistance. Previous studies in human liver and muscle biopsies have shown that total DAG content was more strongly associated with insulin resistance in liver and muscle than other putative mediators of insulin resistance (67, 68). More evidence suggests that DAG in liver and muscle was significantly correlated with insulin resistance (suppression of glucose production, HOMA-IR, insulin signaling cascade and etc.) (19, 69, 70). In subjects with hepatic insulin resistance, *sn*-1,2-DAG accumulates in the liver and activates PKCε (71). Insulin receptor kinase (IRK) Thr1160 has been recently identified as a PKCε substrate and IRK phosphorylation destabilizes the active configuration of the IRK, leading to impaired IRK activity and downstream insulin signaling (17). In subjects with muscle insulin resistance, *sn*-1,2-DAG activates PKCθ and further increases insulin receptor substrate (IRS)-1 serine phosphorylation, which inhibits insulin-stimulated IRS-1 tyrosine phosphorylation and downstream insulin signaling (68, 72-74).

Ceramide is another potential mediator of insulin resistance in liver and muscle (75-78). Two major mechanisms have been proposed to explain ceramide-induced insulin resistance (79-81). The first mechanism is that ceramides activate PKCζ, resulting in

reduced translocation of protein kinase B (Akt) to the plasma membrane and impaired downstream insulin action. Another mechanism is that ceramides activate protein kinase 2A, which could further dephosphorylate and inactivate Akt.

Chapter 4

Current Treatments for Type 2 Diabetes and an Introduction to Adiponectin

T2DM is one of the leading causes of mortality in the adult population worldwide (82, 83) and plays a critical predisposing role in the pathogenesis of metabolic syndrome, nonalcoholic fatty liver disease (NAFLD) and cardiovascular disease (CVD) (5-7, 84). A combination of lifestyle changes and pharmacological treatment is important to achieve great metabolic control in diabetes patients (85). The current available treatments for T2MD and a potential novel therapy, adiponectin will be briefly reviewed.

Metformin is considered as the first-line treatment for T2DM. In the intestines, metformin can change the composition of gut microbiota and activates mucosal AMP-activated protein-kinase (AMPK) that maintains the integrity of the intestinal barrier (86, 87). In the liver, metformin can inhibit gluconeogenesis by several mechanisms (88). The most frequent side effects of metformin are gastrointestinal and metformin reduces intestinal absorption of vitamin B12 (85). Sulfonylureas and meglitinides can stimulate insulin release by similar mechanisms (89). Sulfonylureas are a classic first or second-line therapy for patients with T2DM (90). The main problems related to sulfonylureas and meglitinides are loss of efficacy due to beta cell dysfunction, hypoglycemia, weight gain and cardiovascular risk (91-96). The alpha-glucosidase inhibitors delay carbohydrate absorption and digestion, resulting in a reduction in postprandial hyperglycemia and TAGs (97, 98). The side effects are mainly gastrointestinal and α-glucosidase inhibitors can produce asymptomatic elevation of liver enzymes (98, 99).

Thiazolidinediones (TDZs) increase insulin sensitivity, activate peroxisome proliferator-activated receptors (PPARs) and preserve pancreatic beta cell function (85). The main side effects of TDZs are weight gain and heart failure (100, 101). Dipeptidyl peptidase-4 inhibitors (iDPP4) are used as monotherapy in patients inadequately controlled by diet and exercise, and dual therapy in combination with metformin, TZDs and insulin. iDPP4 inhibit DPP4, an enzyme that rapidly inactivates incretins (GLP1 and GIP), and therefore increase incretin concentrations, which can further improve insulin

secretion and inhibit glucagon (85). The side effects of iDPP4 are rare. Sodium glucose co-transporter-2 inhibitors (iSGLT2) inhibit renal reabsorption of glucose, increase its excretion and reduce hyperglycemia in patients with T2DM, resulting in a reduction in weight and blood pressure (102). Urogenital tract infections, orthostatic hypotension and volume depletion are the main side effects of iSGLT2 (103).

Almost all currently available therapies have side effects, and they are often inadequate. Lots of studies have been shown that current therapies are valuable for reducing microvascular complications, but are not effective in reducing cardiovascular events, probably even being harmful in those with advanced type 2 diabetes (104, 105). So cardiovascular safety of anti-diabetic medications has become another essential requirement for new medications. In addition, given that current treatment approaches do not prevent or slow the loss of β-cell function, there is clearly an urgent need for alternative approaches. As such, these obstacles highlight a clear scientific and health priority for developing more effective treatments for T2DM and insulin resistance. Adiponectin has emerged as an anti-diabetic, anti-inflammatory and anti-atherogenic adipokine produced exclusively by adipocytes as the form of full-length and globular adiponectin (23, 24). Globular adiponectin is generated by proteolytic cleavage of full-length adiponectin (106). Adiponectin forms different multimers and is present in serum in trimer, hexamer or high molecular weight form (106). Almost all adiponectin appears to exist as full-length adiponectin in plasma, globular adiponectin only accounts for a relatively small amount. But globular adiponectin is more potent than the full-length adiponectin. Plasma adiponectin levels in humans range from 0.5 to 30 μg/ml, which is about 1000-fold higher than the concentrations of most other hormones such as leptin and insulin (107). Plasma adiponectin levels are decreased in obesity, insulin resistance and T2DM (108, 109). Administration of adiponectin has been shown to produce a rapid glucose-lowering effect and ameliorate insulin resistance in mice (110-112). Studies in humans and monkeys

showed that plasma adiponectin levels correlate significantly with whole-body insulin sensitivity (25, 26). Overexpression or administration of adiponectin results in a decrease in hyperglycemia, improvement in systemic insulin sensitivity, protection cardiovascular health and maintenance of β-cell function (23, 27, 113, 114), whereas adiponectin-deficient mice exhibit impaired insulin sensitivity and diabetes (24, 28).

The effect of adiponectin seems to be mediated by several mechanisms **(Fig. 3)**. In the liver, adiponectin has been shown to reduce hepatic glucose production in isolated hepatocytes (111) by activating AMPK and consequently reducing the expression of gluconeogenic proteins such as PEPCK and G6Pase (115). Full-length adiponectin can also enhance fatty acid oxidation in liver slices by increasing the phosphorylation of ACC in an AMPK-dependent pathway (116) and reduce fatty acid synthesis by suppressing LKB1/AMPK/SREBP1c pathways (115, 117). However, Yaumachi et al. found that globular adiponectin cannot activate hepatic AMPK signaling pathways. So the underlying mechanisms by which globular adiponectin reduces hepatic triglyceride (TAG) are still unclear (112). Similarly, in the muscle, adiponectin can reduce TAG content and improve peripheral insulin sensitivity by increasing fatty acid oxidation in an AMPK/ACC dependent pathway and through modulation of calcium influx (23, 115, 118). An alternative mechanism proposed to explain adiponectin's insulin sensitizing effect is by stimulating ceramidase activity and reducing liver ceramide content, which is independent of AMPK (114).

However, there are a lot of controversial studies regarding insulin signaling pathways. For example, numerous studies have dissociated ceramide content from insulin sensitivity (66, 67, 119, 120), calling into question the physiologic relevance of this finding. Our study will be critical to clarify those controversies. Furthermore, notably, most of the mechanistic studies were performed *in vitro* or *ex vivo*, lacking *in vivo* studies that model physiologic metabolism and the complex stimuli involved in regulating these processes.

Furthermore, direct effects of adiponectin on insulin signaling molecules, rates of endogenous glucose production (EGP), tissue-specific glucose uptake and tissue-specific rates of mitochondrial oxidation remain poorly investigated. Thus, understanding the underlying mechanisms of adiponectin would unveil a novel pathway affecting diabetes susceptibility.

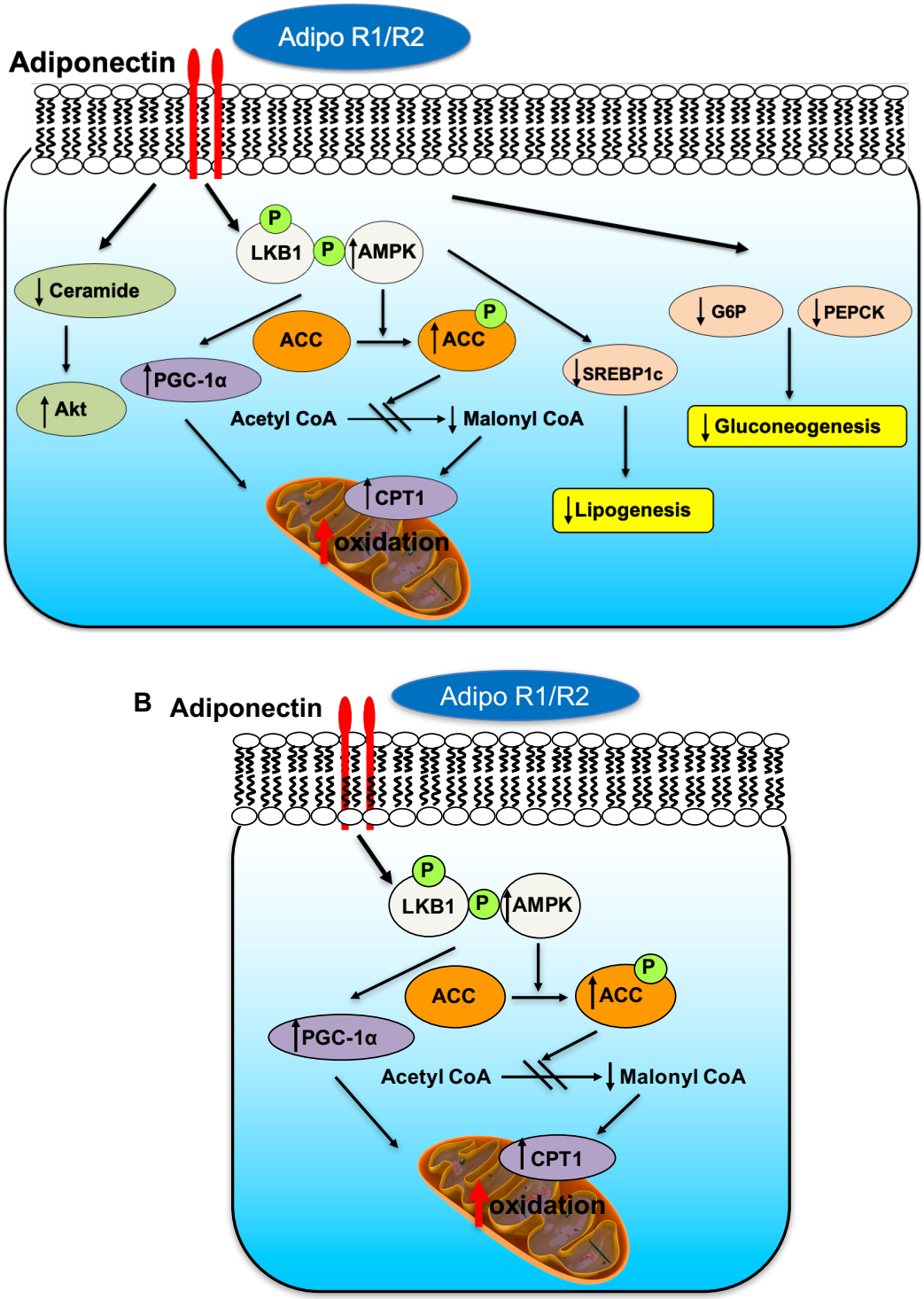

Figure 3. Schematic representations of the molecular mechanisms by which adiponectin reduces plasma glucose levels and decreases fat in liver (A) and skeletal muscle (B).

Chapter 5

OGT suppresses S6K1-mediated macrophage inflammation and metabolic disturbance

ABSTRACT

Enhanced inflammation is believed to contribute to overnutrition-induced metabolic disturbance. Nutrient flux has also been shown to be essential for immune cell activation. Here, we report an unexpected role of nutrient-sensing *O*-linked β-N-acetylglucosamine (*O*-GlcNAc) signaling in suppressing macrophage pro-inflammatory activation and preventing diet-induced metabolic dysfunction. Overnutrition stimulates an increase in *O*-GlcNAc signaling in macrophages. *O*-GlcNAc signaling is down-regulated during macrophage pro-inflammatory activation. Suppressing *O*-GlcNAc signaling by *O*-GlcNAc transferase (OGT) knockout enhances macrophage pro-inflammatory polarization, promotes adipose tissue inflammation and lipolysis, increases lipid accumulation in peripheral tissues, and exacerbates tissue-specific and whole-body insulin resistance in high fat diet-induced obese mice. OGT inhibits macrophage pro-inflammatory activation by catalyzing ribosomal protein S6 kinase beta-1 (S6K1) *O*-GlcNAcylation and suppressing S6K1 phosphorylation and mTORC1 signaling. These findings thus identify macrophage *O*-GlcNAc signaling as a homeostatic mechanism maintaining whole-body metabolism in the setting of overnutrition[1].

[1] Other contributors to this work include Yunfan Yang, Harding Luan, Bichen Zhang, Kaisi Zhang, Jin Hyun Nam, Zongyu Li, Minnie Fu, Alexander Munk, Dongyan Zhang, Simeng Wang, Yuyang Liu, João Paulo Albuquerque, Qunxiang Ong, Rui Li, Qi Wang, Marie E. Robert, Rachel J. Perry, Dongjun Chung, Gerald I. Shulman, Xiaoyong Yang

INTRODUCTION

Modern global healthcare faces challenges that are different from past generations, as embodied by the prevalence of obesity worldwide. Obesity and associated insulin resistance play a pivotal role in the pathogenesis of type 2 diabetes, nonalcoholic fatty liver disease, atherosclerotic heart disease and other disorders (65, 121). The association between obesity and the immune system has long been appreciated. The vicious cycle of inflammation between metabolic organs and immune cells in obese individuals is of major importance to the development of whole-body insulin resistance and metabolic dysfunction (122-125). For example, changes in adipose tissue microenvironment caused by chemokine release, adipocyte death, and other changes. during obesity lead to macrophage infiltration and pro-inflammatory activation, which further lead to detrimental effects on insulin action in metabolic tissues and contributes to whole-body insulin resistance (50, 126, 127). On the other hand, metabolic rewiring has been shown to be essential for immune cell maturation and acquisition of functional competency (128, 129). For example, classical (M1-like; pro-inflammatory) activation of macrophages is coupled to increased glycolysis, reduced mitochondrial oxidative phosphorylation and fragmented TCA cycle, while alternative (M2-like; anti-inflammatory) activation of macrophages are characterized by changes in iron metabolism, fatty acid oxidation, glutamine metabolism, and UDP-GlcNAc pathway (130, 131). Despite the growing knowledge of the function of immune cells in tissue and whole-body metabolism and an emerging role of metabolic pathways in immune cell activation and immune responses, how immune cells sense and integrate nutritional cues and how the nutrient-sensing mechanisms control immune cell activation and whole-body metabolism remain overarching questions in the field.

O-GlcNAcylation is a nutrient-sensing post-translational modification that involves the attachment of a single *O*-linked β-N-acetylglucosamine (*O*-GlcNAc) moiety to proteins (132-134). Nutrients including glucose, amino acid, fatty acid, and nucleotide flux into the

hexosamine biosynthetic pathway (HBP) to generate the donor molecule for *O*-GlcNAcylation, uridine diphosphate GlcNAc (UDP-GlcNAc). A single pair of enzymes, *O*-GlcNAc transferase (OGT) and *O*-GlcNAcase (OGA), catalyze the addition and removal of *O*-GlcNAc moieties from serine and threonine residues of nuclear, cytoplasmic, and mitochondrial proteins, respectively. *O*-GlcNAc signaling, the dynamic and reversible modification in cells, has been shown to fluctuate with the availability of nutrients and regulate numerous signaling pathways (135-139). Dysregulated *O*-GlcNAc homeostasis has been linked to chronic human diseases associated with metabolic dysregulation, such as obesity, diabetes, cardiovascular diseases, Alzheimer's disease, and cancer (140-142). Studies have shown that *O*-GlcNAcylation dampens insulin signaling both in vitro and in vivo (134, 135, 143). Key metabolic regulators such as protein kinase B (Akt), forkhead box protein O1 (FOXO1), carnitine palmitoyltransferase 2 (CPT2) and peroxisome proliferator-activated receptor-γ coactivator (PGC-1α), can be regulated by *O*-GlcNAcylation (144-147). *O*-GlcNAcylation was discovered in immune cells over 30 years ago and has been shown to regulate several immune signaling pathways in vitro, such as extracellular signal-regulated kinase (ERK), c-Jun N-terminal kinase (JNK), p38 mitogen-activated protein kinase, and nuclear factor κB (NF-κB) signaling pathways (135-137, 148-150). However, the function of *O*-GlcNAc signaling in immune regulation, especially during metabolic perturbations, remains elusive.

In obesity and insulin resistance, chronic low-grade inflammation develops in multiple organs such as adipose tissue, liver and skeletal muscle, which is reflected by immune cell infiltration and elevated pro-inflammatory cytokine production (8, 31, 34, 35, 122, 123, 125). Macrophages are the primary cell type responsible for immune responses in metabolic tissues (127, 151). Adipose tissue inflammation is characterized by macrophage infiltration and has been linked to impaired whole-body energy homeostasis (50, 127, 152). Approximately 10-15% of the stromal cells in adipose tissue are

macrophages in lean mice, whereas it increases up to 60% of in obese mice (31, 153). Furthermore, macrophages are capable of acquiring diverse functions in response to physiological and environmental signals. Classically activated (M1-like) macrophages produce pro-inflammatory cytokines and promote insulin resistance, while alternatively activated (M2-like) macrophages produce anti-inflammatory cytokines and are associated with insulin sensitivity and the lean phenotype (154, 155).

Here, we explored the role of *O*-GlcNAc signaling in macrophage activation and metabolic regulation in a mouse model of diet-induced obesity. We observed an increase in macrophage *O*-GlcNAc signaling during overnutrition and a transient decrease in *O*-GlcNAc signaling during macrophage pro-inflammatory polarization. Loss of OGT enhances macrophage pro-inflammatory activation in adipose tissue, which leads to enhanced adipocyte lipolysis, ectopic lipid accumulation in liver and muscle, and whole-body insulin resistance. These data elucidate an anti-inflammatory role for *O*-GlcNAc signaling through inhibiting macrophage pro-inflammatory activation and provide a molecular link between overnutrition, inflammation and metabolic dysfunction.

RESULTS

O-GlcNAc signaling is altered during overnutrition and macrophage activation.

To study the nutritional regulation of macrophage function, we first examined how macrophages respond to different nutrient environments in vitro. Mouse peritoneal macrophages and bone marrow-derived macrophages (BMDMs) were first maintained in a culture medium containing physiological (5 mM) glucose and then challenged with 25 mM glucose or 0.3 mM palmitate to mimic glucolipotoxic conditions in type 2 diabetes. Glucosamine (GlcN) was used as a positive control to boost HBP and O-GlcNAcylation. Both conditions and GlcN led to enhanced overall *O*-GlcNAcylation levels, but not OGT and OGA levels, in cultured macrophages **(Fig. 1*A* and S1*A*)**. Moreover, peritoneal macrophages cocultured with epididymal white adipose tissue (AT) from the high-fat diet (HFD)-fed mice have increased overall *O*-GlcNAcylation levels, but not OGT and OGA levels, as compared to macrophages cocultured with AT from normal chow (NC)-fed mice **(Fig. 1*B*)**. These results suggest that overnutrition stimulates an increase of *O*-GlcNAc signaling in macrophages in vitro, possibly by boosting the HBP pathway.

We then sought to determine the activity of *O*-GlcNAc signaling during macrophage activation. Gene expression profiles retrieved from the Gene Expression Omnibus repository showed the level of OGT transcripts was decreased by ~20% in LPS/IFNγ polarized M1-like human macrophages, while no change in OGA transcriptional level was found (156) **(Fig. S1*B*)**. To further determine the activation of *O*-GlcNAc signaling during macrophage activation, we induced pro-inflammatory M1 [M(LPS)] and anti-inflammatory M2 [M(IL-4)] polarization by using lipopolysaccharides (LPS) and interleukin-4 (IL-4) respectively in mouse peritoneal macrophages, BMDMs, and macrophage cell line RAW 264.7. Consistent with the changes observed in human macrophages, quantitative real-time PCR (qRT-PCR) analysis showed that OGT transcriptional level was decreased during LPS-induced M1 polarization but not IL-4-

induced M2 polarization, without any difference in OGA transcripts **(Fig. 1*C* and S1*C*)**. Next, we examined the activation of *O*-GlcNAc signaling at the protein level in BMDMs. The overall *O*-GlcNAc modification level was decreased by 25-40% during M1 polarization, accompanied by a ~45% decrease in the OGT protein level **(Fig. 1*D* and S1*D*)**. A transient elevation of overall *O*-GlcNAc modification, but no significant changes in OGT and OGA protein levels, were observed during M2 polarization **(Fig. S1*E*)**. These results demonstrate that *O*-GlcNAc signaling is temporarily suppressed during M1 polarization and transiently enhanced at the onset of M2 polarization.

We then examined the dynamic changes of overall O-GlcNAcylation levels in various subpopulations of adipose tissue macrophages during HFD feeding by using flow cytometry **(Fig. 1*E, F* and S1*F-I* and *S*2)**. F4/80 served as a pan macrophage marker. CD11c and CD206 were used as markers for M1-like and M2-like macrophages, respectively. MGL1, highly expressed in resident population of adipose tissue macrophages, and CCR2, critical for macrophage recruitment to inflammation sites, were also used as markers (157-159). The results showed that: (1) $MGL1^+$ macrophages generally have higher overall *O*-GlcNAcylation levels, as compared to $CCR2^+$ macrophages; (2) $CD206^+$ M2-like macrophages generally have higher overall *O*-GlcNAcylation levels, as compared to $CD11c^+$ M1-like macrophages; (3) Macrophage *O*-GlcNAc signaling is enhanced or maintained at a similar level at the early stage of obesity (1-week and 4-week HFD feeding) but decreased at the late stage of obesity (12-week HFD feeding), as compared to the NC-fed mice. Based on these results, we hypothesized that macrophage *O*-GlcNAc signaling may have an anti-inflammatory function and involves in maintaining metabolic homeostasis, especially at the early stage of obesity.

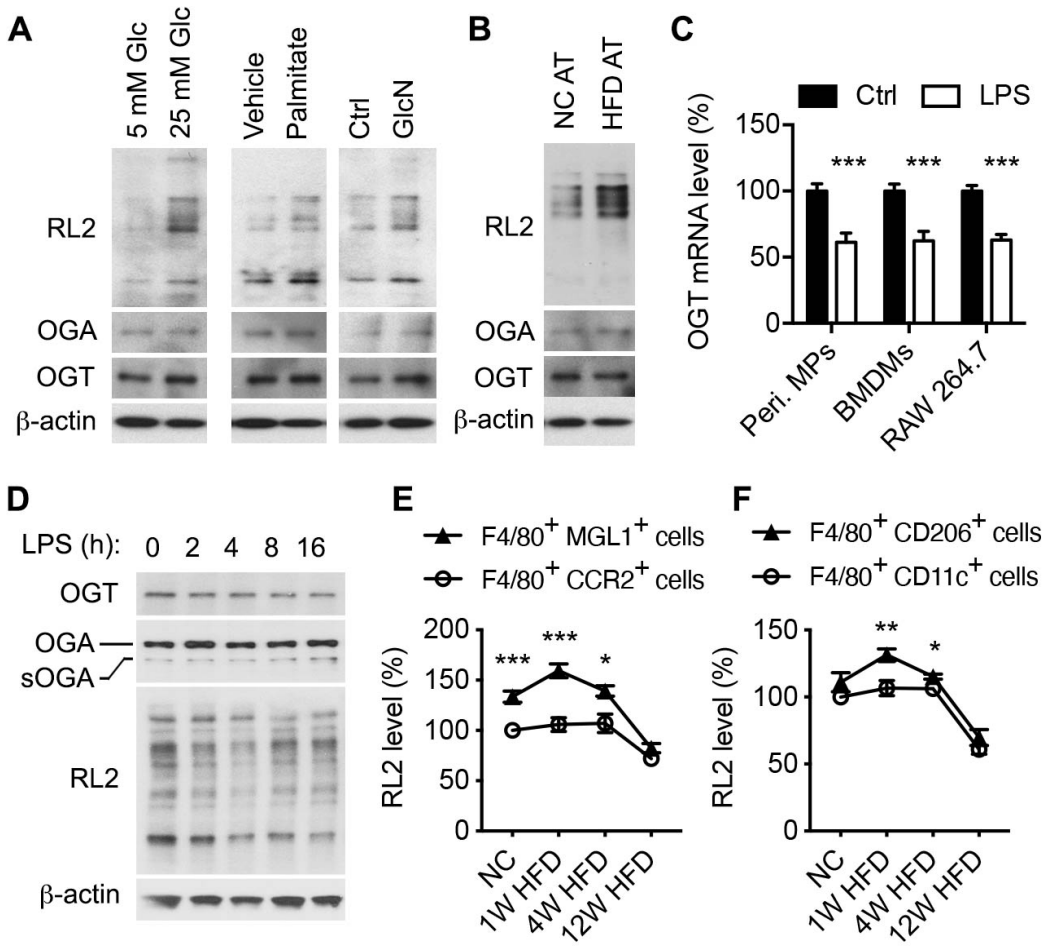

Figure 1. Nutrient-sensing *O*-GlcNAc signaling is regulated during overnutrition and macrophage activation. (*A*) Western blot analysis of OGT, OGA, and overall *O*-GlcNAcylation levels in mouse peritoneal macrophages after 2 hours treatment. "Vehicle" was 0.2% BSA and "Ctrl" was culture medium. Glucosamine (GlcN) was used as a positive control. RL2 recognizes *O*-GlcNAc modification on proteins. (*B*) Western blot analysis of OGT, OGA, and overall *O*-GlcNAcylation levels in mouse peritoneal macrophages co-cultured with epididymal white adipose tissue (AT) of normal chow (NC)-fed and high fat diet (HFD)-fed mice for 2 hours. (*C*) *Ogt* mRNA level in mouse peritoneal macrophages (peri. MPs), mouse bone marrow-derived macrophages (BMDMs), and RAW 264.7 macrophage cells (n = 4-8). LPS was used to stimulate M1 polarization. (*D*) Representative western blots of OGT, OGA and overall *O*-GlcNAcylation levels in mouse

BMDMs. LPS was used to stimulate M1 polarization. (*E* and *F*) Flow cytometric analysis of average intensity of O-GlcNAc (RL2) staining of macrophage subpopulations including $F4/80^+$ $CCR2^+$ cells, $F4/80^+$ $MGL1^+$ cells (*E*), $F4/80^+$ $CD11c^+$ M1-like macrophages, and $F4/80^+$ $CD206^+$ M2-like macrophages (*F*) in the stromal vascular fraction (SVF) of epididymal white adipose tissue (eWAT) from NC-fed, 1-week HFD-fed, 4-week HFD-fed, and 12-week HFD-fed WT mice (n = 4-6). Data are shown as mean ± SEM. *$p < 0.05$, **$p < 0.01$, ***$p < 0.001$ by unpaired Student's t-test.

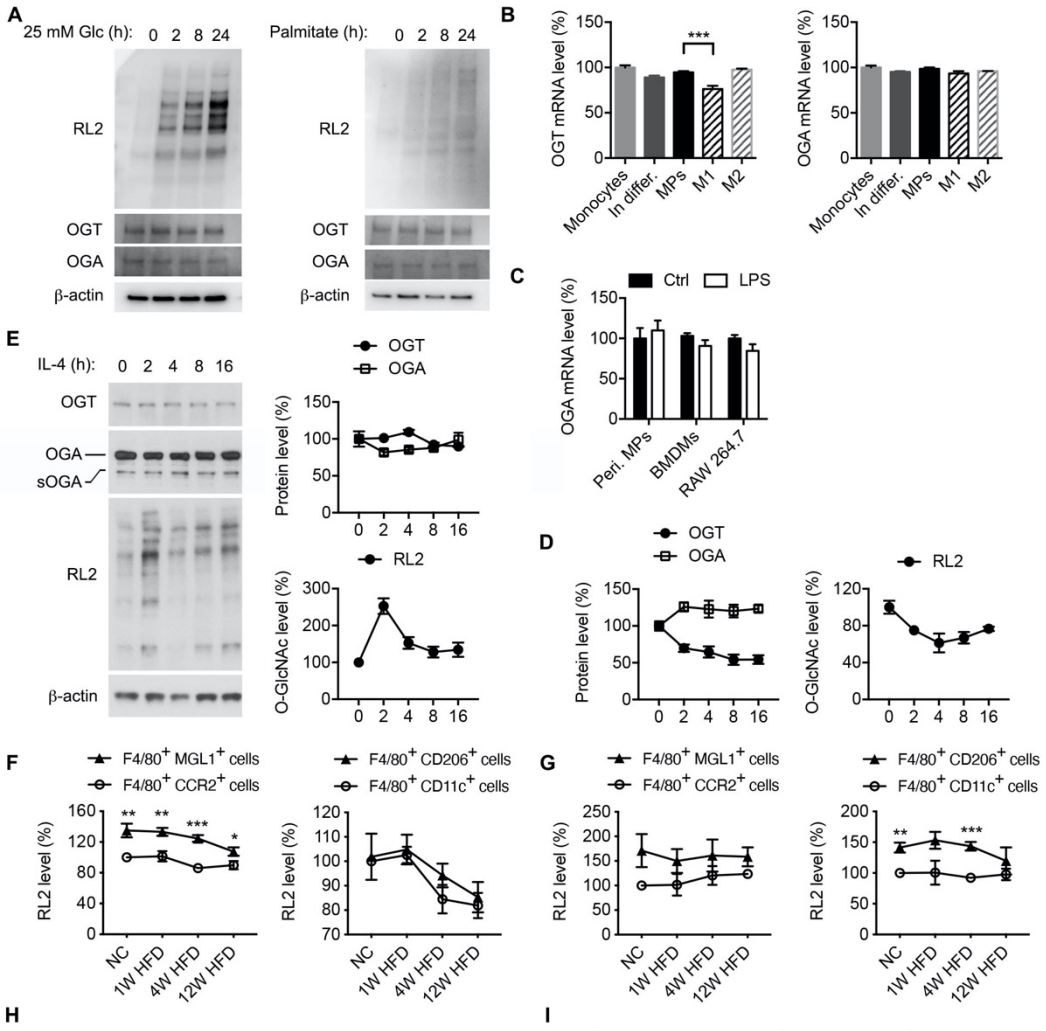

F4/80+ MGL1+ cells	Significance
NC vs. 1W HFD	*
NC vs. 4W HFD	ns
NC vs. 12W HFD	***

F4/80+ CCR2+ cells	Significance
NC vs. 1W HFD	ns
NC vs. 4W HFD	ns
NC vs. 12W HFD	*

F4/80+ CD206+ cells	Significance
NC vs. 1W HFD	*
NC vs. 4W HFD	ns
NC vs. 12W HFD	***

F4/80+ CD11c+ cells	Significance
NC vs. 1W HFD	ns
NC vs. 4W HFD	ns
NC vs. 12W HFD	***

Figure S1. Macrophage *O*-GlcNAc signaling is regulated during overnutrition and macrophage activation. (*A*) Western blots showing the levels of overall *O*-GlcNAcylation (RL2), OGT, OGA, and β-actin in bone marrow derived macrophages (BMDMs) with 0, 2, 8, and 24 hours of incubation with 25 mM glucose (Glc) or 0.3 mM palmitate. (*B*) *Ogt* and *Oga* mRNA levels in primary human peripheral blood monocytes, cells in the monocyte-macrophage differentiation process (In differ.), *in vitro* differentiated macrophages (MPs),

and M1- and M2-polarized macrophages (*n* = 3). Data were retrieved from Gene Expression Omnibus repository (GSE47122). (*C*) *Oga* mRNA levels in mouse peritoneal macrophages (peri. MPs), mouse bone marrow-derived macrophages (BMDMs), and RAW 264.7 macrophage cells (*n* = 4-8). LPS was used to stimulate M1 polarization. (*D*) Quantitative analysis of OGT, OGA and overall *O*-GlcNAcylation levels in mouse BMDMs as shown in Fig. 1*D* (*n* = 3). (*E*) Representative western blots and quantitative analysis of OGT, OGA and overall O-GlcNAcylation levels in mouse BMDMs. IL-4 was used to stimulate M2 polarization (*n* = 5). (*F* and *G*) Flow cytometric analysis of average intensity of *O*-GlcNAc (RL2) staining of macrophage subpopulations including $F4/80^+$ $CCR2^+$ cells, $F4/80^+$ $MGL1^+$ cells, $CD11c^+$ M1-like macrophages, and $CD206^+$ M2-like macrophages in the stromal vascular fraction (SVF) of inguinal white adipose tissue (iWAT) (*F*) and interscapular brown adipose tissue (BAT) (*G*) from NC-fed, 1-week high fat diet (HFD)-fed, 4-week HFD-fed, and 12-week HFD-fed WT mice. (*H* and *I*) Statistical analysis of macrophage subpopulations in the SVF of epididymal white adipose tissue (eWAT) from NC-fed, 1-week HFD-fed, 4-week HFD-fed, and 12-week HFD-fed WT mice (*n* = 4-6). Data are shown as mean ± SEM. ns: not significant, **p* < 0.05, ***p* < 0.01, ****p* < 0.001 by one-way ANOVA with Dunnett multiple comparisons for (*B*)*,* (*H*) *and* (*I*). **p* < 0.05, ***p* < 0.01, ****p* < 0.001 by unpaired Student's t-test for other graphs.

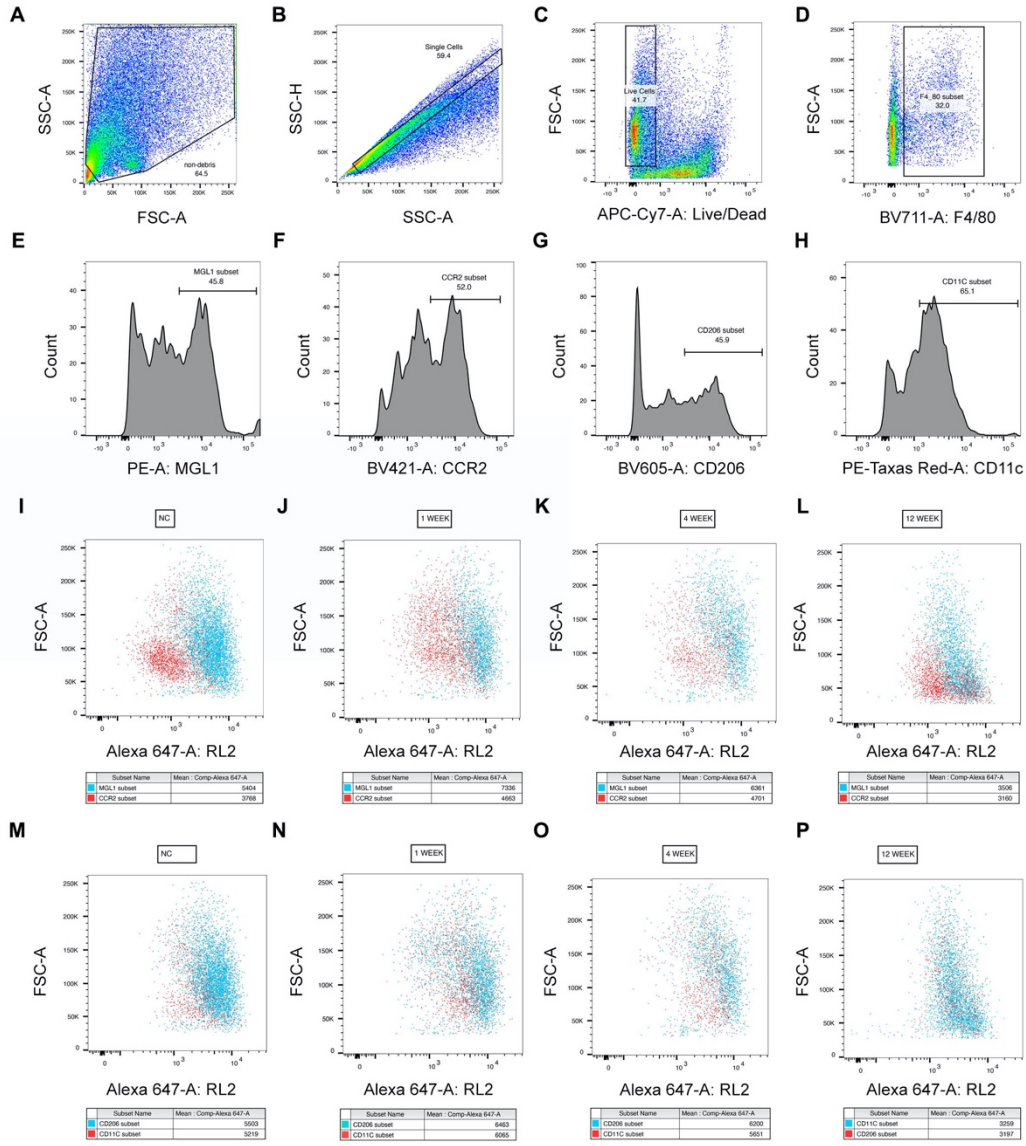

Figure S2. *O*-GlcNAcylation level in various subpopulations of adipose tissue macrophages during HFD feeding. (*A-H*) Gating strategy of macrophage subpopulations in the SVF of eWAT. Debris (*A*) and doublet cells (*B*) were excluded according to forward scatter profiles (FSC-A) and side scatter profiles (SSC-A and SSC-H). Subsequently, Live/Dead Dye staining were used to exclude dead cells (*C*), and F4/80$^+$ cells were selected (*D*). Macrophages (F4/80$^+$ cells) were plotted according to MGL1 or CCR2 expression to show F4/80$^+$ MGL1$^+$ cells (MGL1: a tissue-resident macrophage marker) (*E*) and F4/80$^+$ CCR2$^+$ cells (CCR2: an infiltrated macrophage marker) (*F*).

Similarly, macrophages were plotted according to CD206 or CD11c expression to identify F4/80$^+$ CD11c$^+$ cells (CD11c$^+$ M1-like macrophages) (*G*) and F4/80$^+$ CD206$^+$ cells (CD206$^+$ M2-like macrophages) (*H*). (*I*-*L*) Representative flow cytometry dot plots of overall *O*-GlcNAcylation levels in F4/80$^+$ CCR2$^+$ cells (CCR2 subset) and F4/80$^+$ MGL1$^+$ cells (MGL1 subset) in the SVF of eWAT from NC-fed (*I*), 1-week HFD-fed (*J*), 4-week HFD-fed (*K*), and 12-week HFD-fed (*L*) WT mice. (*M*-*P*) Representative flow cytometry dot plots of overall *O*-GlcNAcylation levels in CD11c$^+$ M1-like macrophages (CD11c subset) and CD206$^+$ M2-like macrophages (CD206 subset) in the SVF of eWAT from NC-fed (*M*), 1-week HFD-fed (*N*), 4-week HFD-fed (*O*), and 12-week HFD-fed (*P*) WT mice.

Macrophage *Ogt* knockout mice are prone to diet-induced metabolic dysfunction.

To test our hypothesis, we bred the Ogt^{flox} strain with the *LysM*-Cre transgenic line to generate a mouse line with *Ogt* deletion in macrophages and other myeloid cells (hereafter termed OGT MKO mice) **(Fig. S3*A*-*C*)** and provided them with *ad libitum* access to NC and HFD. Flow cytometric analysis showed that OGT KO preferentially affect *O*-GlcNAc signaling in $CCR2^+$ macrophages **(Fig. S3*D*)**. OGT MKO mice fed NC showed no difference in body weight, body composition, and whole-body insulin sensitivity compared to their wild-type (WT) littermates **(Fig. S3*E*-*K*)**. We then challenged the mice with HFD. OGT MKO mice gained slightly more body weight and fat mass compared to their WT controls after 12 weeks of HFD feeding, which could be attributed to increased food intake **(Fig. 2*A*, *B* and S3*L*)**. In contrast, there is no difference in lean mass, oxygen consumption (VO_2), respiratory exchange ratio (RER), physical activity and energy expenditure **(Fig. 2*C* and S3*M*-*P*)**. Increases in tissue weights of subcutaneous inguinal white adipose tissue (iWAT) and interscapular brown adipose tissue (BAT), but not epididymal white adipose tissue (eWAT), were observed in OGT MKO mice **(Fig. S4*A*-*C*)**. Despite an increase in BAT mass, the core body temperature of OGT MKO mice dropped more quickly than WT mice during an acute cold challenge **(Fig. S4*D*)**, which is likely due to BAT whitening **(Fig. S4*E*)**.

Whole-body glucose metabolism of HFD-fed WT and OGT MKO mice was assessed by intraperitoneal glucose tolerance test (GTT), insulin tolerance test (ITT), and hyperinsulinemic-euglycemic clamps before their body weight diverge **(Fig. 2*A* and S4*F*-*H*)**. OGT MKO mice showed a 2-fold increase in plasma insulin levels after overnight fasting without any significant difference in fasting plasma glucose, non-esterified fatty acid (NEFA) or triacylglycerol (TAG) concentrations **(Fig. S4*I*-*L*)**, reflecting whole-body insulin resistance. GTT and ITT showed that OGT MKO mice had impaired glucose metabolism and insulin resistance as compared to WT controls **(Fig. S4*M*-*Q*)**, which is

also illustrated by an increase in the homeostatic model assessment for insulin resistance (HOMA-IR) **(Fig. S4*R*)**. During the hyperinsulinemic-euglycemic clamp, OGT MKO mice exhibited a marked impairment in whole-body insulin sensitivity as reflected by a ~55% decline in the glucose infusion (GINF) rate required to maintain euglycemia **(Fig. 2*D* and Fig. S4*S*, *T*)**. Despite no difference in the basal endogenous glucose production (EGP) rate, the EGP during the clamp was significantly higher in OGT MKO mice **(Fig. 2*E*)**, demonstrating impaired hepatic insulin sensitivity. The increased EGP during the clamp may be attributable to increased acetyl-CoA **(Fig. S4*U*)**, an allosteric activator of pyruvate carboxylase (50). We also observed a reduced whole-body glucose turnover rate in OGT MKO mice **(Fig. 2*F*)**, which could be at least partially attributed to reduced glucose uptake in eWAT, BAT, and gastrocnemius muscle **(Fig. 2*G*)**. Together, these results demonstrate that loss of macrophage OGT exacerbates diet-induced whole-body insulin resistance independent of body weight changes.

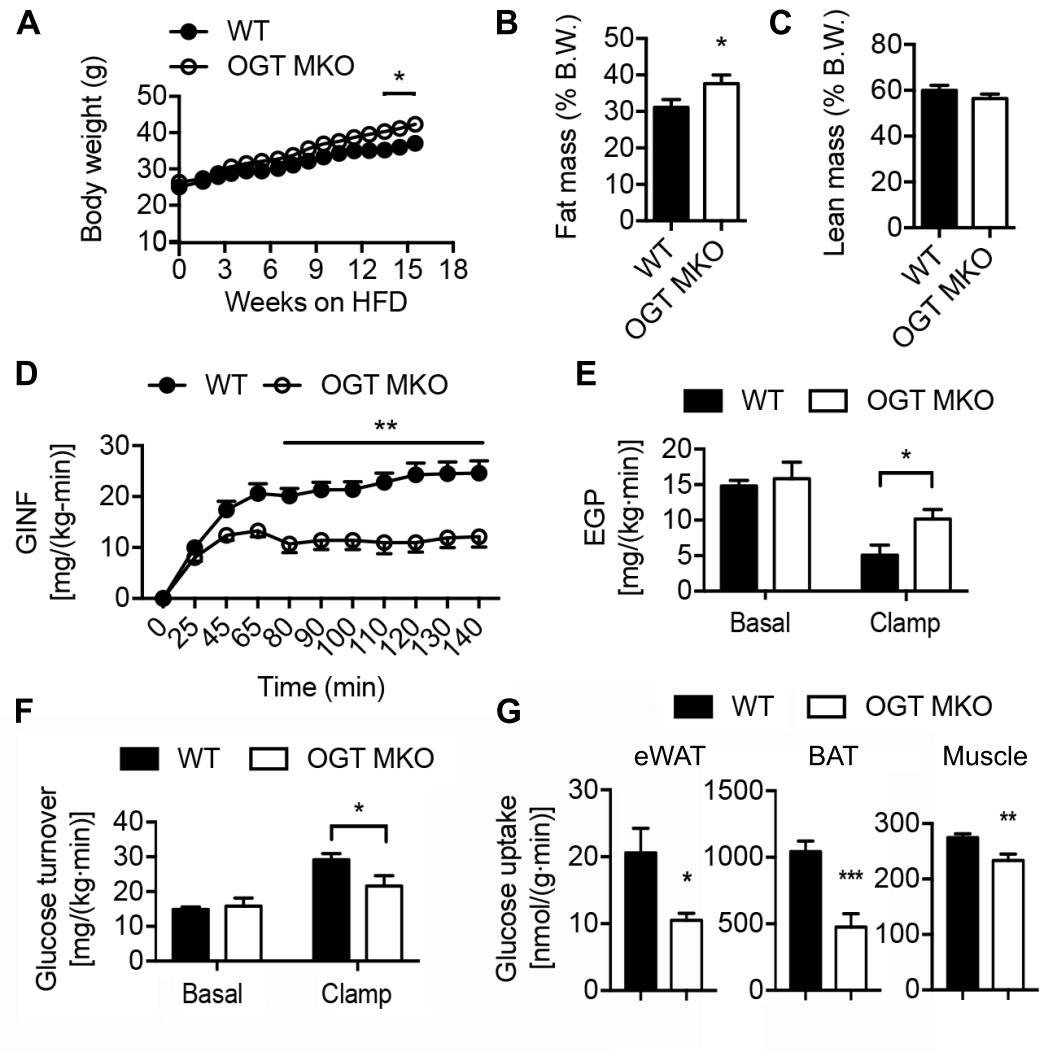

Figure 2. OGT MKO mice are prone to diet-induced metabolic dysfunction. (*A*) Body weight of HFD-fed WT and OGT MKO mice. (*B* and *C*) Fat mass (*B*) and lean mass (*C*) of 18-week HFD-fed WT and OGT MKO mice (n = 12-19). (*D*) Glucose infusion (GINF) rate to maintain euglycemia during hyperinsulinemic-euglycemic clamps in 8-week HFD-fed WT and OGT MKO mice. (*E* and *F*) Endogenous glucose production (EGP) rate (*E*) and whole-body glucose turnover rate (*F*) in both basal (without insulin stimulation) and clamps (with insulin stimulation) states in 8-week HFD-fed WT and OGT MKO mice. (*G*) Glucose uptake in eWAT, BAT and gastrocnemius muscle under insulin-stimulated condition in 8-week HFD-fed WT and OGT MKO mice (n = 5-8). Data are shown as mean ± SEM. *p < 0.05, **p < 0.01, ***p < 0.001 by unpaired Student's t-test.

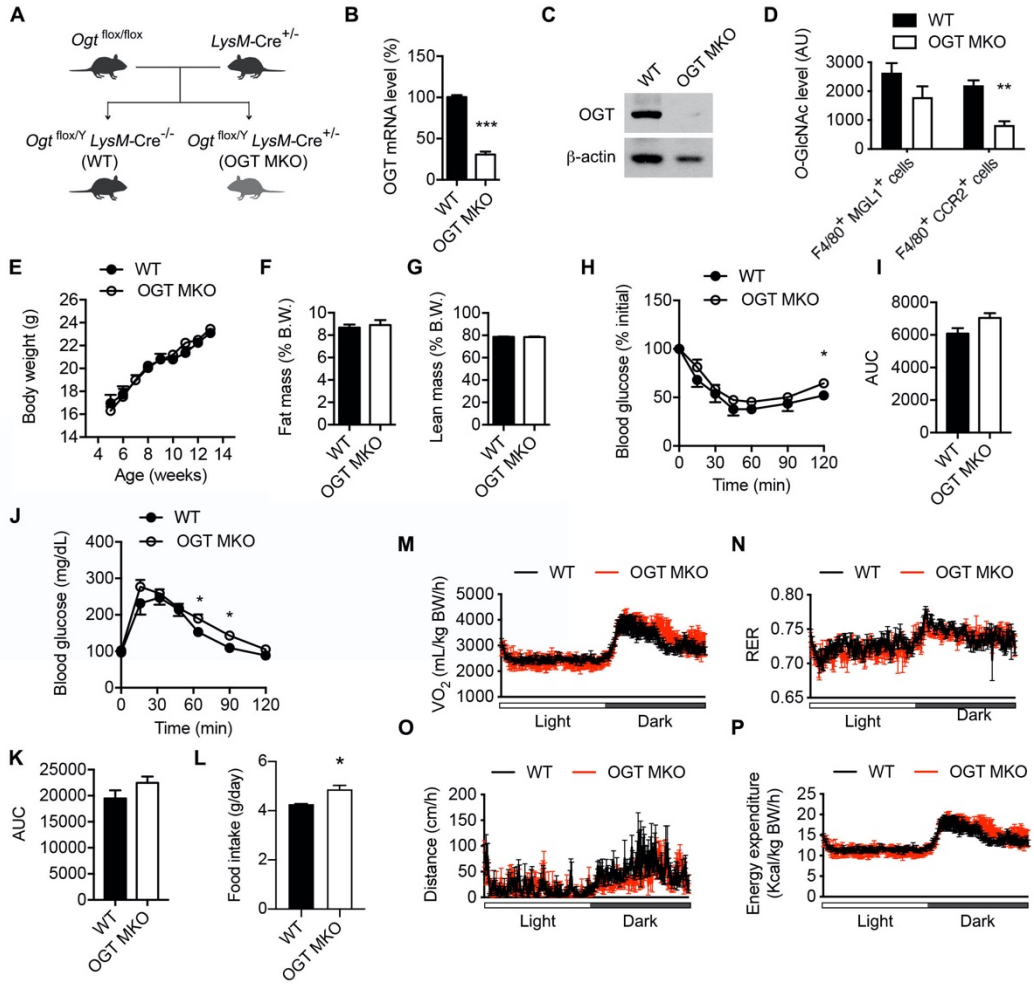

Figure S3. NC-fed OGT MKO mice have normal glucose metabolism, while HFD-fed OGT MKO have impaired glucose metabolism and increased food intake. (*A*) The scheme for generating myeloid cell-specific *Ogt* knockout (OGT MKO) and wide type (WT) control mice. (*B* and *C*) qRT-PCR (n = 7-12) and western blot analysis showing the mRNA and protein levels in peritoneal macrophages isolated from WT and OGT MKO mice. (*D*) Flow cytometric analysis of average intensity of *O*-GlcNAc (RL2) staining of F4/80$^+$ CCR2$^+$ cells and F4/80$^+$ MGL1$^+$ cells in the SVFs of eWAT from 12-week HFD-fed WT and OGT MKO mice (n = 5). (*E-G*) Body weight (*E*) (n = 5) and body composition (*F* and *G*) (n = 17) of normal chow (NC)-fed WT and OGT MKO mice. (*H-K*) Insulin tolerance test (*H* and *I*) and glucose tolerance test (*J* and *K*) in NC-fed WT and OGT MKO mice. (*L*) Average daily

food intake of 12-week HFD-fed WT and OGT MKO mice. (*M*-*P*) Whole-body oxygen consumption rates (*M*), respiratory exchange ratios (RERs) (*N*), physical activities (*O*), and energy expenditure (*P*) of 12-week HFD-fed WT and OGT MKO mice ($n = 4$). Data are shown as mean ± SEM. *$p < 0.05$, **$p < 0.01$, ***$p < 0.001$ by unpaired Student's t-test.

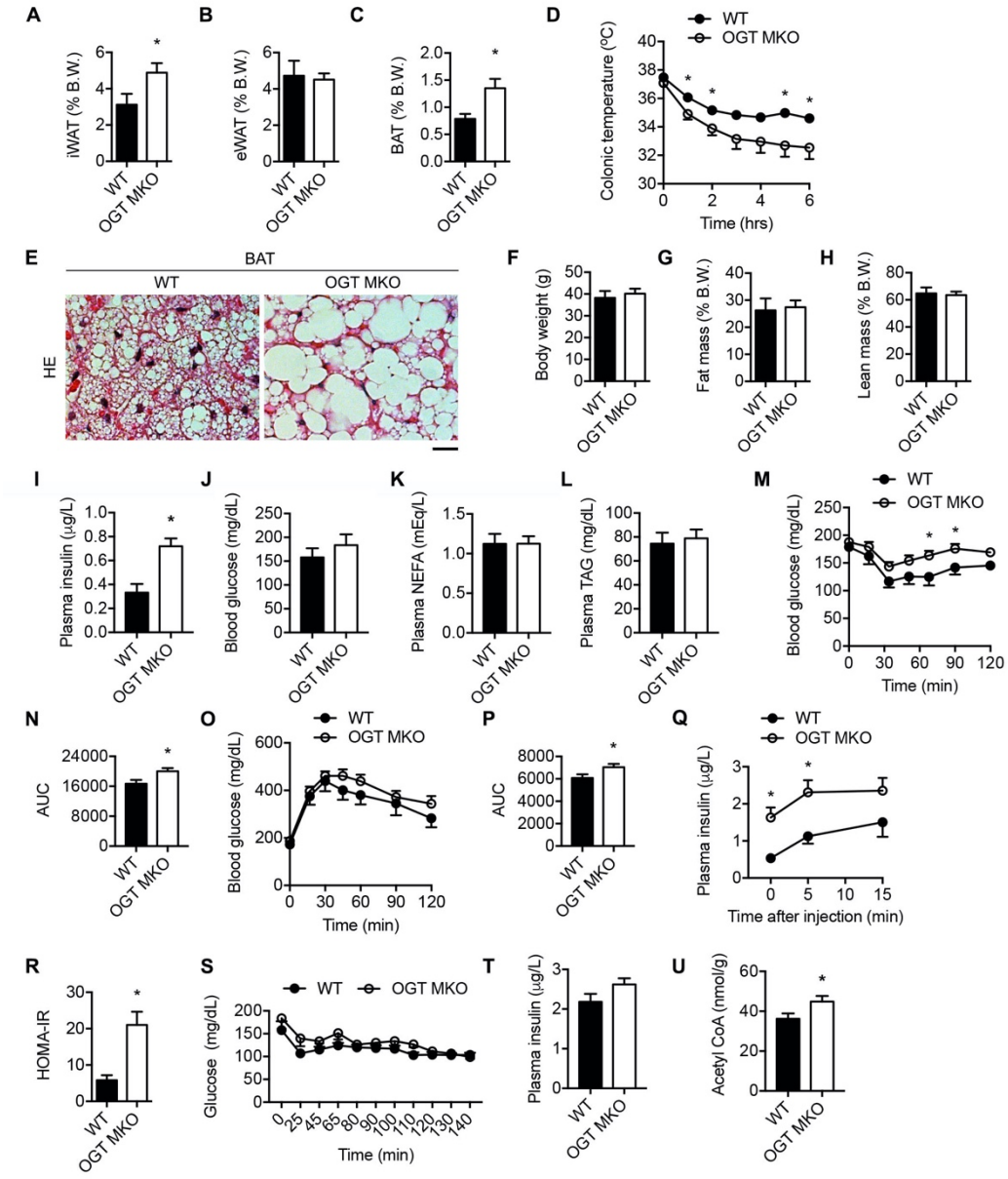

Figure S4. Impaired BAT function and insulin sensitivity in HFD-fed OGT MKO mice. (*A*-*C*) Tissue weights of inguinal white adipose tissue (iWAT) (*A*), eWAT (*B*), and intrascapular brown adipose tissue (BAT) (*C*) of 18-week HFD-fed WT and OGT MKO mice (n = 7-12). (*D*) Cold challenge test in 12-week HFD-fed WT and OGT MKO mice (n = 8-14). (*E*) Hematoxylin and eosin (H&E) staining of BAT from HFD-fed WT and OGT MKO mice. Scale bar, 20 μm. (*F*-*H*) Body weight (*F*) and body composition (*G* and *H*) of 8-week HFD-fed WT and OGT MKO mice. (*I* and *J*) Plasma insulin and blood glucose

concentrations of 8-week HFD WT and OGT MKO mice after overnight fasting (*n* = 6-14). (*K* and *L*) Plasma non-esterified fatty acid (NEFA) (*K*) and triglyceride (TAG) (*L*) levels of 8-week HFD WT and OGT MKO mice after overnight fasting (*n* = 5-6). (*M* and *N*) Plasma glucose concentrations (*M*) and $AUC_{glucose}$ (*N*) during the insulin tolerance test (ITT) in 12-week HFD-fed WT and MKO mice. (*O*-*Q*) Plasma glucose concentrations (*O*), $AUC_{glucose}$ (*P*) and insulin concentrations (*Q*) during the intraperitoneal glucose tolerance test (GTT) in 12-week HFD-fed WT and MKO mice. $AUC_{glucose}$ was calculated using the trapezoidal rule. (*R*) Homeostasis model assessment of insulin resistance (HOMA-IR) in 12-week HFD-fed WT and OGT MKO mice (*n* = 5-14). (*S*) Plasma glucose levels during hyperinsulinemic-euglycemic clamps in 8-week HFD-fed WT and OGT MKO mice (*n* = 5-8). (*T* and *U*) Plasma insulin concentrations (*T*) and hepatic acetyl-CoA contents (*U*) of 8-week HFD WT and OGT MKO mice at the end of the hyperinsulinemic-euglycemic clamps (*n* = 6). Data are shown as mean ± SEM. $*p < 0.05$ by unpaired Student's t-test.

Loss of macrophage OGT promotes inflammation, adipose tissue lipolysis, and ectopic lipid accumulation and insulin resistance.

We then assessed the activation of insulin signaling in peripheral tissues of HFD-fed WT and OGT MKO mice. The phosphorylation of insulin receptor (IR) kinase and Akt were reduced in liver, gastrocnemius muscle and eWAT of OGT MKO mice during the clamp, indicating impaired insulin signaling **(Fig. 3*A*, *B* and S5*A*)**. Ectopic lipid accumulation is closely associated with insulin resistance (6, 65). To explore the underlying mechanism of insulin resistance in OGT MKO mice, levels of TAGs and diacylglycerols (DAGs) in liver and skeletal muscle were determined and the results showed that OGT MKO mice had a 2-3 fold increase in TAG content in liver and muscle **(Fig. 3*C* and *D*)**. Consistently, a fatty liver phenotype including increased liver weight, pale-colored liver and histopathologic features of steatosis was observed in OGT MKO mice **(Fig. S5*B-E*)**. A 1.5-3 fold increase in DAG content was also found in all tested compartments (membrane, lipid droplets and cytosol) in both liver and muscle of OGT MKO mice **(Fig. 3*E*, *F* and Fig. S5*F-I*)**. Previous studies demonstrated that membrane DAG induces peripheral insulin resistance by promoting the membrane translocation of PKCε in liver and PKCθ in skeletal muscle (17, 20). Consistently, OGT MKO mice showed increased PKCε translocation from cytosol to the membrane in liver and increased PKCθ and PKCε translocation in muscle **(Fig. 3*G-I* and Fig. S5*J*, *K*)**. In contrast, no difference in hepatic and muscle ceramide content was observed **(Fig. S5*L* and *M*)**. Taken together, these data suggest that loss of macrophage OGT promotes diet-induced whole-body insulin resistance by enhancing ectopic lipid accumulation and activating the DAG-PKC pathway in liver and skeletal muscle.

Next, we sought to understand the cause of ectopic lipid accumulation in peripheral tissues of OGT MKO mice. Studies have shown that excessive adipose tissue lipolysis plays an essential pathogenic role in diet-induced insulin resistance by enhancing fatty

acid flux into metabolic tissues (50, 160, 161). Consistent with this idea, OGT MKO mice had increased fatty acid turnover rates during the clamp **(Fig. 3*J*)**, suggesting that loss of macrophage OGT impaired insulin suppression of adipose tissue lipolysis. We then performed an ex vivo lipolysis assay with freshly prepared tissue trunks of WATs from HFD-fed WT and OGT MKO mice. The results showed that CL-316,243 (a β3-adrenergic receptor agonist)-stimulated lipolysis was significantly enhanced in sWAT and eWATs of OGT MKO mice **(Fig. 3*K* and *L*)**. To explore the underlying mechanism, we obtained cultured mature adipocytes differentiated from stromal vascular fraction (SVF) of mouse eWAT. Then we examined the effects of in vitro cultured WT and OGT KO macrophages on adipocyte lipolysis in contact (coculture) and non-contact (transwell) manners. The results showed that both WT and OGT KO macrophages stimulated adipocyte lipolysis in a cell-cell contact-independent manner. More importantly, compared to WT macrophages, OGT KO macrophages were more potent to stimulate adipocyte lipolysis **(Fig. 3*M*)**, demonstrating an essential role for macrophage OGT in suppressing adipocyte lipolysis through secreted factors. Previous studies have shown that inflammatory cytokines are important regulators of adipocyte lipolysis (50, 162). We then determined the levels of pro-inflammatory cytokines including TNF-α and IL-6 in the serum of 8-week HFD-fed WT and OGT MKO mice and observed a 3-4 fold increase in OGT MKO mice **(Fig. 3*N* and *O*)**. Further analysis and histological analysis of hematoxylin-eosin (H&E) staining showed that TNF-α and IL-6 levels were increased by ~25% in eWAT of OGT MKO mice, but no significant difference in hepatic inflammation **(Fig. 3*P-S* and S5*E*)**, showing that adipose tissue is a primary target of macrophage-induced inflammation. Taken together, these data indicate that macrophage OGT depletion promotes adipose tissue inflammation and lipolysis, enhances fatty acid flux into liver and muscle, and finally leads to ectopic lipid accumulation and DAG-PKC-mediated insulin resistance in these metabolic tissues.

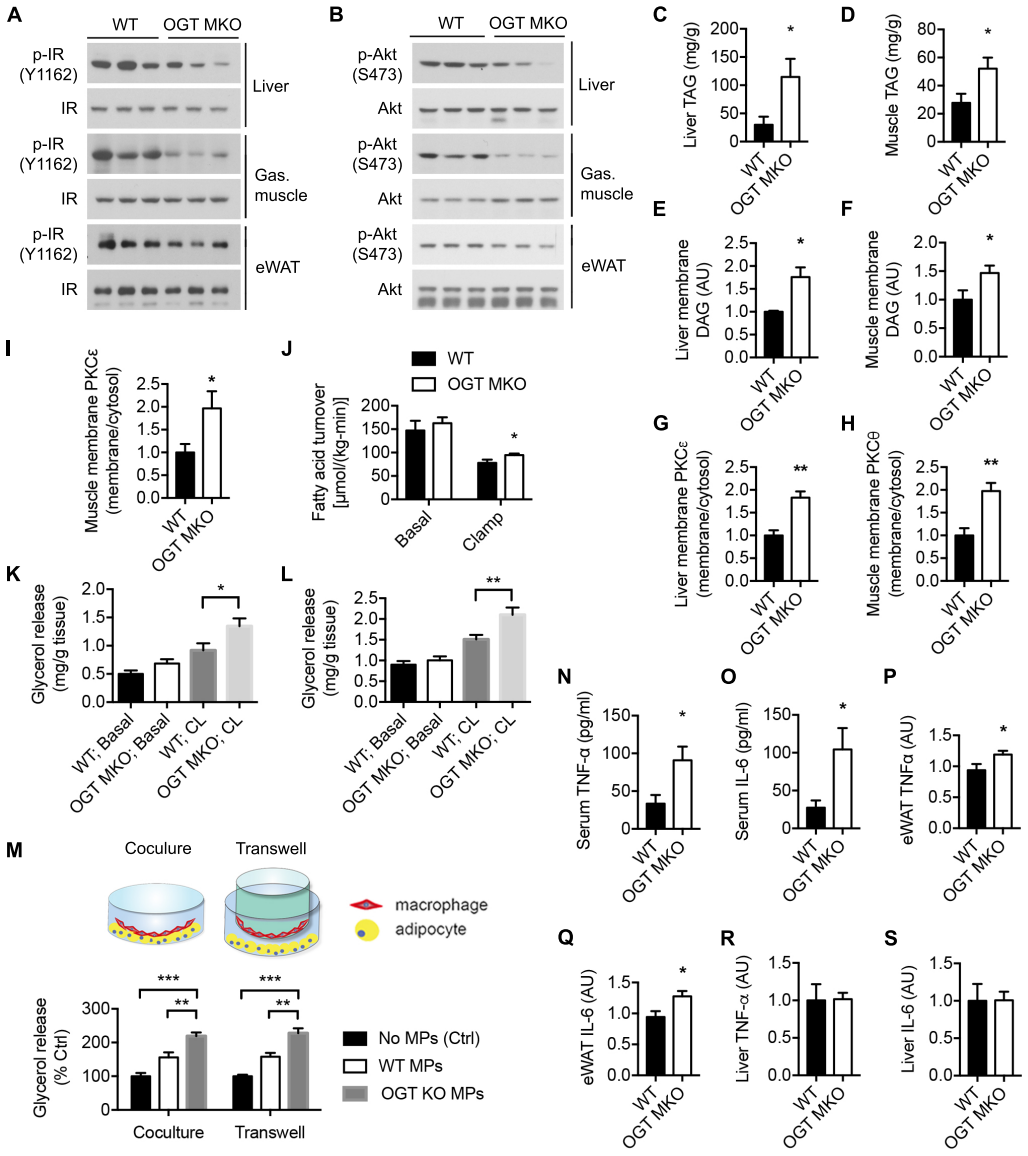

Figure 3. Loss of macrophage OGT promotes inflammation, adipose tissue lipolysis, and ectopic lipid accumulation and insulin resistance in liver and muscle independent of body weight changes. (*A*) Western blots of insulin-stimulated insulin receptor (IR) phosphorylation (Y1162) in liver, gastrocnemius muscle and eWAT of 8-week HFD-fed WT and OGT MKO mice after overnight fasting. (*B*) Western blots of insulin-stimulated Akt phosphorylation (S473) in liver, gastrocnemius muscle and eWAT of 8-week HFD-fed WT and OGT MKO mice after overnight fasting. (*C* and *D*) Triglyceride (TAG) levels in liver (n = 4) and gastrocnemius muscle (n = 9-11) of 12-week HFD-fed WT

and OGT MKO mice. (*E* and *F*) Membrane diacylglycerol (DAG) levels in liver and gastrocnemius muscle of 12-week HFD-fed WT and OGT MKO mice (*n* = 6-14). (*G*) Hepatic membrane/cytosolic PKCε ratio in 12-week HFD-fed WT and OGT MKO mice. (*H* and *I*) Membrane/cytosolic PKCθ and PKCε ratio in gastrocnemius muscle of 12-week HFD-fed WT and OGT MKO mice (*n* = 5). (*J*) Whole-body fatty acid turnover of 8-week HFD-fed WT and OGT MKO mice (*n* = 6). (*K* and *L*) Basal and stimulated (10 μM CL-316,243) lipolysis measured by glycerol released from tissue trunks of iWAT (*K*) and eWAT (*L*) of 12-week HFD-fed WT and OGT MKO mice (*n* = 10-12). (*M*) Scheme and glycerol release rate of in vitro cultured adipocyte when co-cultured with WT and OGT KO peritoneal macrophages in contact (Coculture) and non-contact (Transwell) manners. (*N*-*S*) TNF-α and IL-6 levels in serum (*N* and *O*), eWATs (*P* and *Q*) and livers (*R* and *S*) of 8-week HFD-fed WT and OGT MKO mice. Data are shown as mean ± SEM (*n* = 5-8). *p < 0.05, **$p < 0.01$, ***$p < 0.001$ by two-way ANOVA with Dunnett multiple comparisons for (*K*), (*L*) and (*M*). *$p < 0.05$, **$p < 0.01$ by unpaired Student's t-test for other panels.

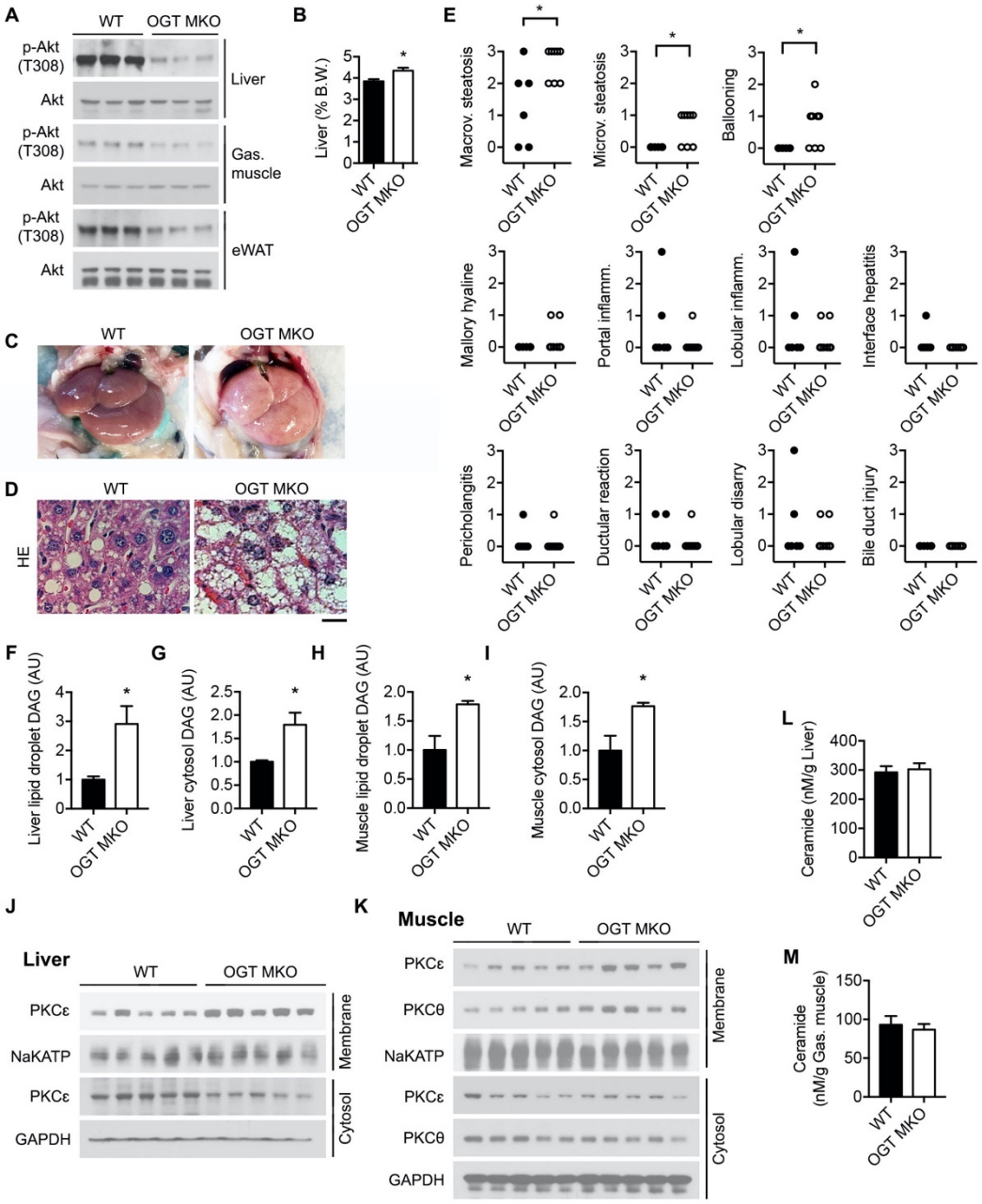

Figure S5. Increased hepatic steatosis and enhanced liver and muscle insulin resistance in HFD-fed OGT MKO mice. (*A*) Western blots of Akt phosphorylation(T308) in liver, gastrocnemius muscle and eWAT. (*B-D*) Tissue weights (*B*) (*n* = 7-12), images (*C*) and H&E staining (*D*) of liver from 12-week HFD-fed WT and OGT MKO mice. Scale bar, 20 μm. (*E*) Blinded histological scoring of liver staining to evaluate hepatic steatosis and liver inflammation and liver injury in 12-week HFD-fed WT and OGT MKO mice. (*F-I*) DAG

levels in lipid droplet fraction and cytosolic fraction in liver (*F* and *G*) and gastrocnemius muscle (*H* and *I*) of 12-week HFD-fed WT and OGT MKO mice (n = 6-14). (*J* and *K*) Western blots showing levels of PKCε in membrane fraction and cytosolic fraction of liver (*J*) and levels of PKCε and PKCθ in membrane fraction and cytosolic fraction of gastrocnemius muscle (*K*). (*L* and *M*) Ceramide contents in liver (*L*) and gastrocnemius muscle (*M*) of 12-week HFD-fed WT and OGT MKO mice (n = 4-6). Data are shown as mean ± SEM. *$p < 0.05$ by Mann-Whitney test for (*E*). *$p < 0.05$ by unpaired Student's t-test for other graphs.

Loss of macrophage OGT promotes adipose tissue inflammation.

To determine the role of macrophage OGT in adipose tissue inflammation, flow cytometric analysis of adipose tissue macrophages and macrophage subpopulations was performed. In WT mice, 12-week HFD feeding induced a 2.5-fold increase of $CCR2^+$ macrophages in eWAT as compared to iWAT, while no difference in $MGL1^+$ macrophages was found **(Fig. S6*A* and *B*)**. Macrophages ($F4/80^+$ cells) comprised 10% of SVF cells in BAT and 30-40% in iWAT and eWAT **(Fig. S6*C*)**. In 12-week HFD-fed OGT MKO mice, a significant increase in the number of total macrophages was found in BAT (~2.5 fold), but not in iWAT and eWAT, as compared to WT mice **(Fig. S6*D* and S7*A*)**. Nevertheless, a ~2-4 fold increase of $F4/80^+$ $CD11c^+$ macrophages in all examined adipose tissues and a ~40-50% decrease of $F4/80^+$ $CD206^+$ macrophages in iWAT and eWAT (per gram of tissue) were observed **(Fig. 4*A*, S6*E, F* and S7*B*)**.

We identified a ~2.5 fold increase in the number of crown-like structures (CLSs) formed by pro-inflammatory macrophages surrounding necrotic adipocytes in the whole-mount adipose tissue staining of iWAT and eWAT from OGT MKO mice **(Fig. 4*B* and *C*)**, which is consistent with enhanced accumulation of pro-inflammatory $CD11c^+$ M1-like macrophages in WATs of OGT MKO mice. qRT-PCR analysis showed that the expression of macrophage pro-inflammatory polarization markers, *Il-6* and *Nos2*, was increased in various adipose tissues of OGT MKO mice compared with WT mice, without difference in *Arg1* expression, an M2 polarization marker **(Fig. 4*D*, *E* and S7*C*)**. These data demonstrate that loss of macrophage OGT aggravates adipose tissue inflammation by promoting pro-inflammatory macrophage activation and/or infiltration, which may contribute to increased WAT lipolysis.

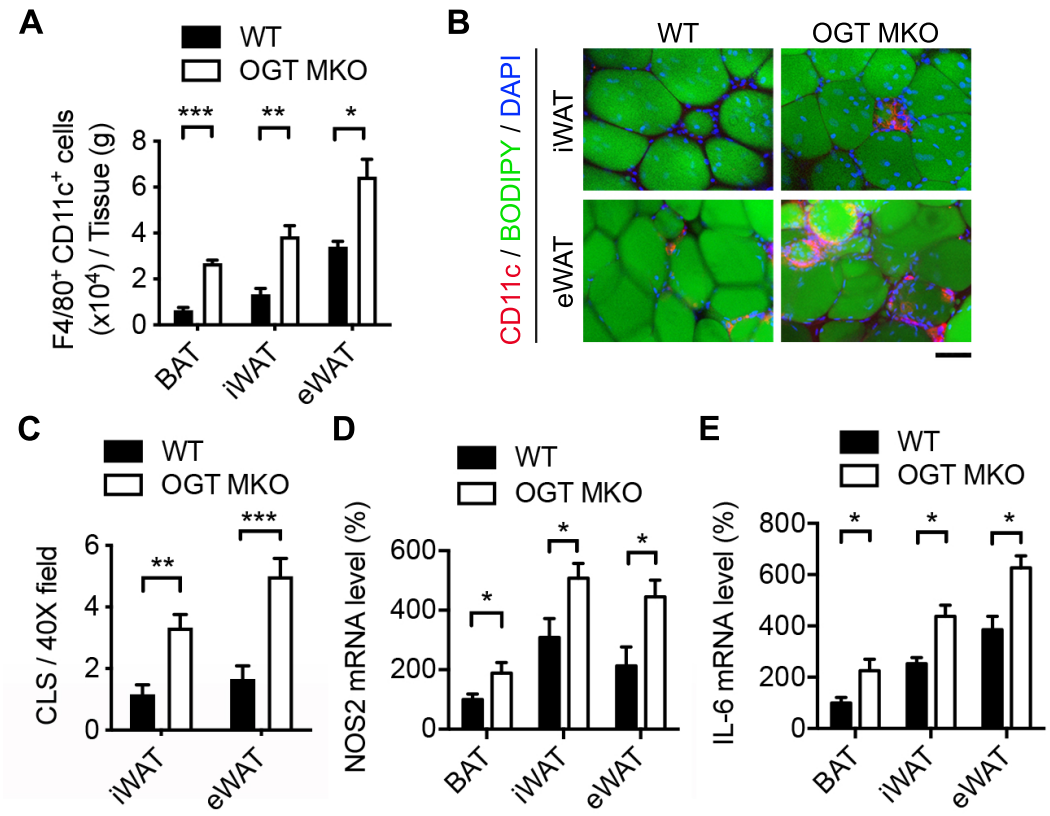

Figure 4. Loss of macrophage OGT promotes adipose tissue inflammation. (*A*) Quantification of flow cytometric analysis of F4/80$^+$ CD11c$^+$ cells in BAT, iWAT and eWAT from 12-week HFD-fed WT and OGT MKO mice (n = 4). (*B*) Whole-mount staining of iWAT and eWAT of 12-week HFD-fed WT and OGT MKO mice showing adipocytes (BODIPY FL, stains lipids) and macrophages (CD11c$^+$ cells) in crown-like structures (CLSs). Scale bar, 80 μm. (*C*) Quantitative results of CLSs in iWAT and eWAT of 12-week HFD-fed WT and OGT MKO mice (n = 6). (*D* and *E*) *Nos2* and *Il-6* mRNA levels in BAT, iWAT, and eWAT of 12-week HFD-fed WT and OGT MKO mice (n = 4-8). Data are shown as mean ± SEM. *p < 0.05, **p < 0.01, ***p < 0.001 by unpaired Student's t-test.

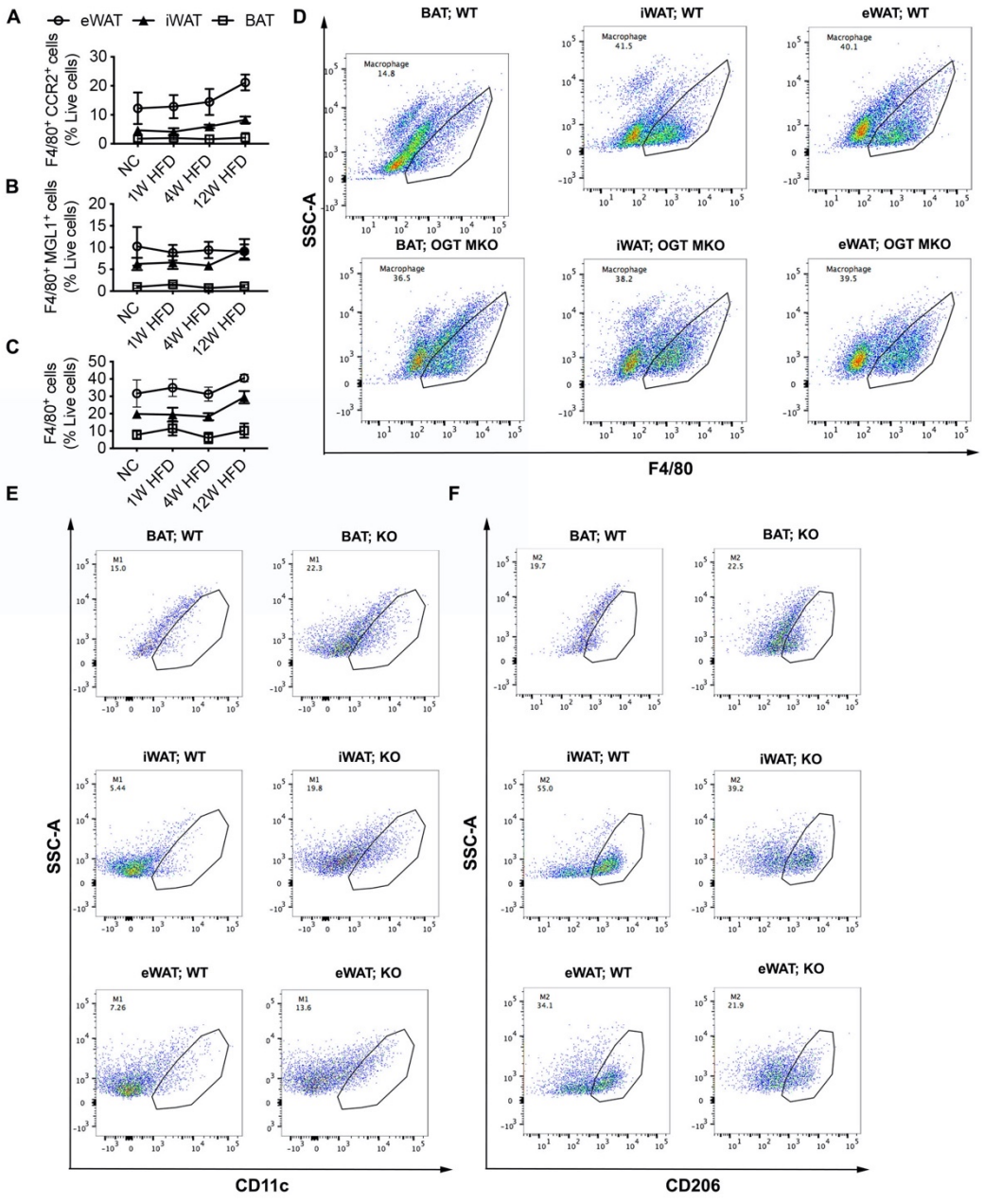

Figure S6. HFD-fed OGT MKO mice have enhanced accumulation of M1-like macrophages in adipose tissue as compared with HFD-fed WT mice. (*A*-*C*) Flow cytometric analysis of macrophage subpopulations including F4/80$^+$ CCR2$^+$ cells (*A*), F4/80$^+$ MGL1$^+$ cells (*B*), and overall macrophages (F4/80$^+$ cells) (*C*) in the SVF of eWAT, iWAT, and BAT from NC-fed, 1-week HFD-fed, 4-week HFD-fed, and 12-week HFD-fed WT mice (n = 4-6). (*D*) Representative flow cytometry dot plots showing macrophages

(F4/80$^+$ cells) in SVF of adipose tissue from HFD-fed WT and OGT MKO mice. (*E* and *F*) Representative dot plots showing CD11c$^+$ cells and CD206$^+$ cells gated through F4/80$^+$ cells shown in (*D*).

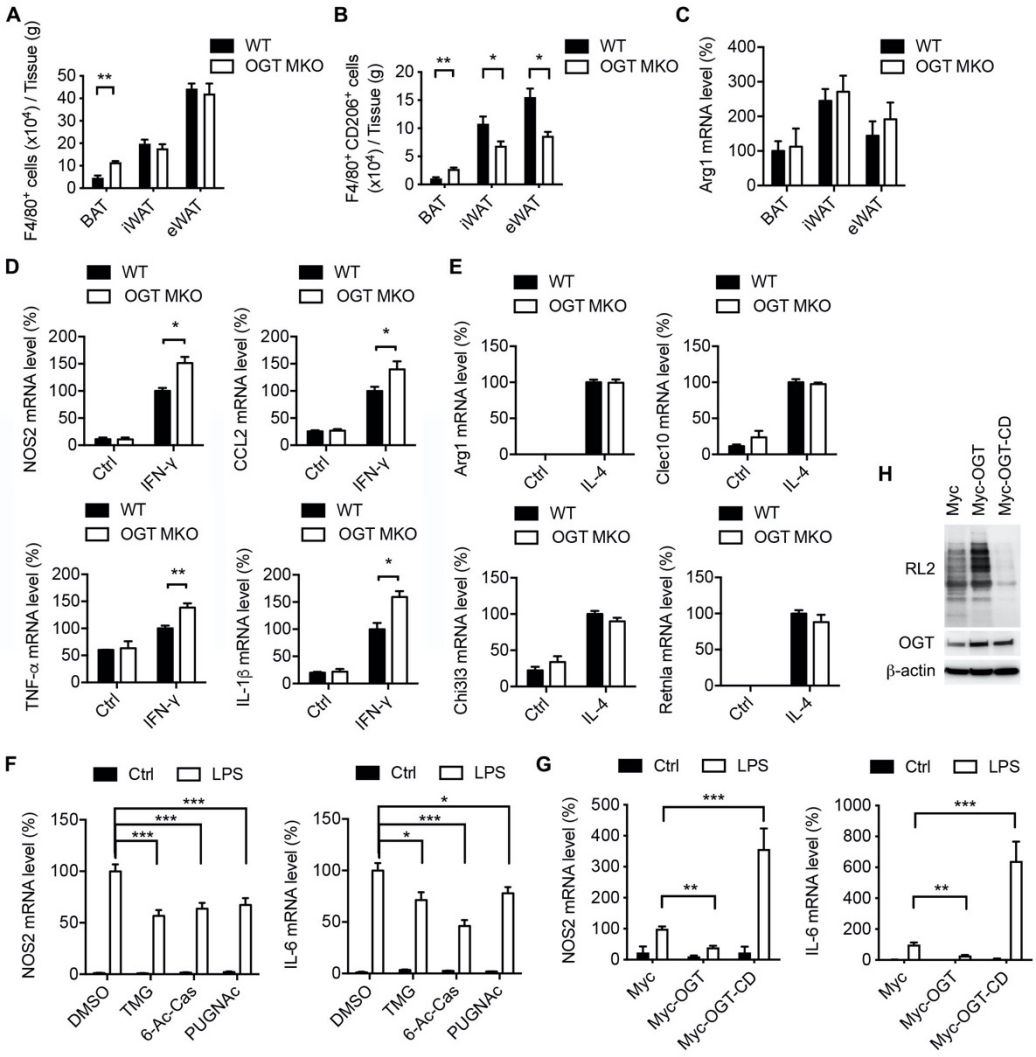

Figure S7. *O*-GlcNAc signaling is involved in macrophage M1 polarization, but not M2 polarization. (*A* and *B*) Quantification of flow cytometric analysis of macrophages (F4/80$^+$ cells) and CD206$^+$ M2-like macrophages in the SVF of BAT, iWAT and eWAT from 12-week HFD-fed WT and OGT MKO mice. (*C*) *Arg1* mRNA level in BAT, iWAT, and eWAT of 12-week HFD-fed WT and OGT MKO mice (*n* = 4). (*D*) *Nos2*, *Ccl2*, *TNF-α*, and *pro-Il-1b* mRNA levels in WT and OGT KO BMDMs. IFN-γ was used to stimulate M1 polarization. (*E*) *Arg1*, *Clec10*, *Chi3l3*, and *Retnla* mRNA levels in WT and OGT KO BMDMs. IL-4 was used to stimulate M2 polarization (*n* = 6). (*F*) *Nos2* and *Il-6* mRNA levels in DMSO-, thiamet-G (TMG)-, 6-Acetamido-6-deoxy-castanospermine (6-Ac-Cas)-, and

PUGNAc-treated RAW 264.7 cells under unstimulated and LPS-stimulated conditions. (*G*) *Nos2* and *Il-6* mRNA levels in Myc-, Myc-OGT-, and Myc-OGT-CD-overexpressing RAW 264.7 cells under unstimulated and LPS-stimulated conditions ($n = 3$). (*H*) Western blots showing levels of overall *O*-GlcNAcylation (RL2), OGT, and β-actin of BMDMs overexpressing Myc, Myc-OGT and Myc-OGT-CD (D925N). Data are shown as mean ± SEM. $^{*}p < 0.05$, $^{**}p < 0.01$, $^{***}p < 0.001$ by two-way ANOVA with Dunnett multiple comparisons for (*F*) and (*G*). $^{*}p < 0.05$, $^{**}p < 0.01$ by unpaired Student's t-test for other panels.

***O*-GlcNAc signaling suppresses macrophage pro-inflammatory activation.**

Based on the above results, we hypothesized that *O*-GlcNAc signaling plays a suppressive role in macrophage pro-inflammatory activation. M1-like polarized macrophages are known to exhibit an elongated and spreading morphology with pseudopod-like protrusions (163). LPS-induced peritoneal macrophage activation was analyzed and we defined the spread cells as "activated cells" and the round-shaped cells as "resting cells" **(Fig. 5*B*)**. Bright-field imaging showed that OGT KO group had a 2-3 fold increase in the percentage of activated cells, as compared to the WT group, under both unstimulated and LPS-stimulated (30 minutes) conditions **(Fig. 5*A-C*)**, suggesting loss of OGT accelerates and promotes LPS-induced macrophage pro-inflammatory activation. We then treated WT and OGT KO BMDMs with fluorescein-labeled zymosan particles and found that OGT KO BMDMs internalized ~75% more zymosan particles compared to WT BMDMs **(Fig. 5*D-F*)**, suggesting loss of OGT enhances macrophage phagocytic activity. Finally, qRT-PCR analysis showed that loss of OGT enhanced the expression of LPS-induced M1 markers including *Nos2*, *Ccl2*, *TNF-α*, and *Il-6* or *pro-Il-1b* by 100-200% and IFN-γ- induced M1 markers by 50-100% **(Fig. 5*G* and S7*D*)**, but had no effect on IL-4-induced M2 markers expression including *Arg1*, *Clec10a*, *Chi3l3*, and *Retnla* **(Fig. S7*E*)**. Together, these data demonstrate a specific role of OGT in suppressing macrophage pro-inflammatory polarization.

To gain further insight into the role of *O*-GlcNAc signaling in macrophage pro-inflammatory polarization, *O*-GlcNAc signaling was interrogated in BMDMs and RAW 264.7 cells by treatment with various OGA inhibitors: thiamet-G (TMG), 6-Acetamido-6-deoxy-castanospermine (6-Ac-Cas) and PUGNAc. The results showed that the pharmacological inhibition of OGA suppressed the expression of LPS-induced M1 markers, *Nos2* and *Il-6,* by 40-60% **(Fig. 5*H* and S7*F*)**. Consistent with this finding, OGT overexpression suppressed LPS-induced *Nos2* and *Il-6* expression by 40-60%, while

overexpression of the dominant negative OGT catalytic dead mutant (OGT-CD, D925N) significantly enhanced LPS-induced *Nos2* and *Il-6* expression **(Fig. 5*I* and S7*G*, *H*)**. Taken together, these results demonstrate a suppressive role of *O*-GlcNAc signaling in macrophage pro-inflammatory activation.

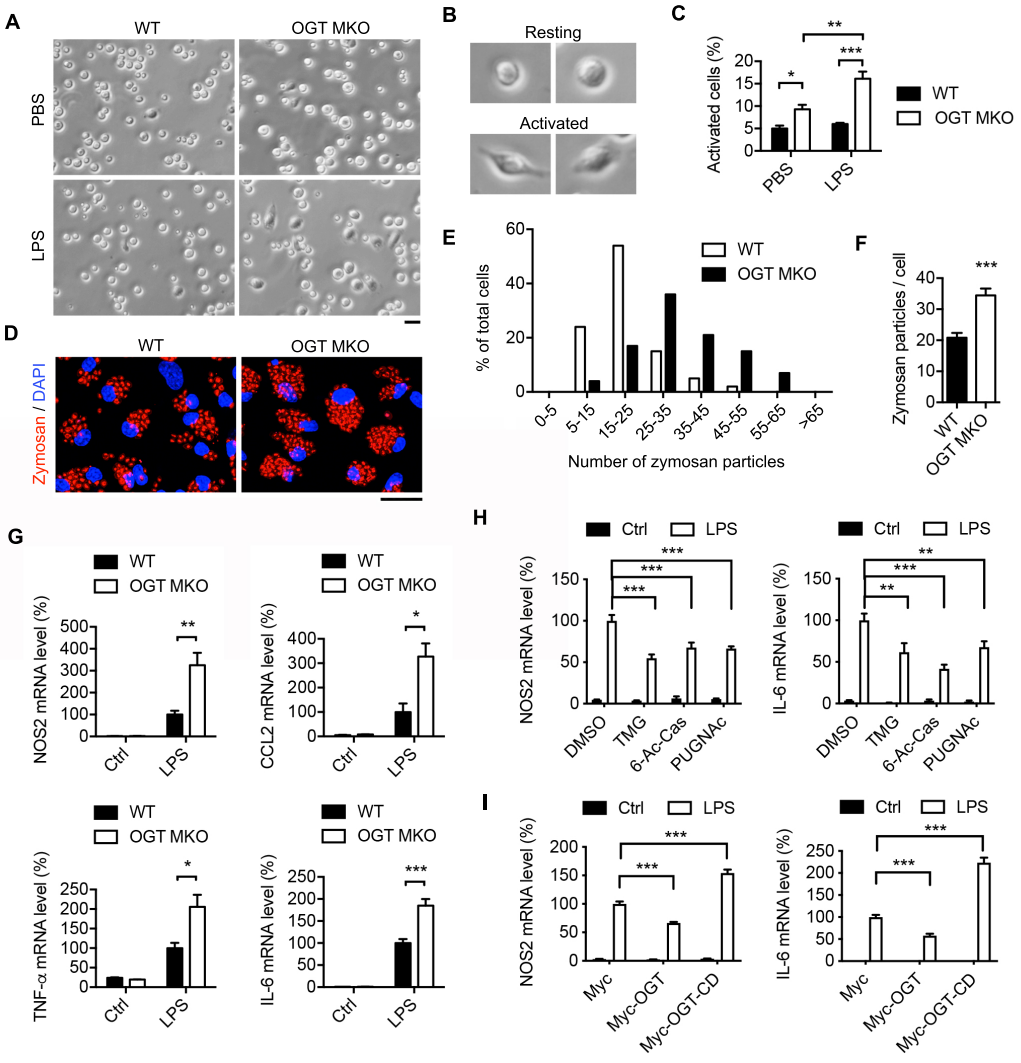

Figure 5. *O*-GlcNAc signaling suppresses macrophage pro-inflammatory activation. (*A-C*) Bright field imaging and statistical analysis of unstimulated and LPS-stimulated activation of peritoneal macrophages isolated from WT and OGT MKO mice (*n* = 4-8). Scale bars, 20 μm. (*D-F*) Fluorescence imaging and statistical analysis of phagocytosis of zymosan particles by WT and OGT KO BMDMs. Scale bar, 20 μm. (*G*) Macrophage M1 marker *Nos2*, *Ccl2*, *TNF-α*, and *Il-6* mRNA levels in un-stimulated and LPS-stimulated WT and OGT KO BMDMs (*n* = 3-6). (*H*) *Nos2* and *Il-6* mRNA levels in DMSO-, thiamet-G (TMG)-, 6-Acetamido-6-deoxy-castanospermine (6-Ac-Cas)-, and PUGNAc-treated BMDMs under unstimulated and LPS-stimulated conditions (*n* = 6). (*I*) *Nos2* and *Il-6*

mRNA levels in Myc-, Myc-OGT-, and Myc-OGT-CD-overexpressing BMDMs under unstimulated and LPS-stimulated conditions (n = 4). Data are shown as mean ± SEM. *p < 0.05, **p < 0.01, ***p < 0.001 by two-way ANOVA with Dunnett multiple comparisons for (*C*), (*H*), and (*I*). *p < 0.05, **p < 0.01, ***p < 0.001 by unpaired Student's t-test for other panels.

RNA sequencing analysis reveals a preferential regulation of macrophage pro-inflammatory polarization by OGT.

Macrophage activation involves extensive transcriptional rewiring (130). To assess the role of OGT in the systemic reprogramming during macrophage activation, we performed RNA sequencing-based transcriptional profiling for unstimulated (M0), LPS-stimulated (M1) and IL-4-stimulated (M2) WT and OGT KO BMDMs. Overall, the heat map of differentially expressed genes (DEGs) showed that loss of OGT led to a significantly increased expression of a large set of genes and a decreased expression of a small set of genes in M0, M1 and M2 polarized BMDMs **(Fig. 6*A*)**. These results demonstrate a prevalent role of OGT in suppressing macrophage activation at the transcriptional level. Strikingly, DEGs between WT and OGT KO BMDMs in M0 and M2 groups shared a similar expression pattern, whereas DEGs in the M1 group showed a very unique pattern **(Fig. 6*A*)**. Venn diagram showing the overlap of DEGs between every two groups also support the same conclusion **(Fig. S8*A*)**. Then all three groups of DEGs were overlaid with a group of genes identified as macrophage-related genes (164, 165). Nine DEGs were found to be present in all groups, suggesting a robust OGT-mediated regulation of these genes. Again, a larger set of macrophage-related DEGs were found to be specifically present in the M1 group (57 in M1 vs. 19 in M2 and 14 in M0) **(Fig. S8*B*)**. Together, these results suggest that OGT in macrophages preferentially regulates macrophage M1 polarization, which is consistent with our previous results showing that loss of OGT affects LPS- and IFN-γ- induced M1 polarization but not IL-4-induced M2 polarization **(Fig. 5*G* and S7*D*, *E*)**. The expression of selected M1 and M2 markers determined by RNA sequencing were also analyzed. Consistent with the previous results, loss of OGT enhanced the expression of M1 markers in LPS-treated BMDMs but did not affect the expression of M2 markers in IL-4-treated BMDMs **(Fig. 6*B* and S8*C*)**.

Gene set enrichment analysis (GSEA) for the Gene Ontology terms showed that loss of OGT in M1-polarized BMDMs enhanced the expression of genes that are highly enriched in the following GO terms: cytokine production, regulation of cytokine production, defense response, positive regulation of multicellular process, and immune response **(Fig. S8*D*)**, supporting a role of OGT in suppressing macrophage M1 activation and inflammation. Genes enriched in GO terms including myeloid cell differentiation and myeloid leukocyte differentiation were down-regulated in M1-polarized OGT KO BMDMs **(Fig. S8*D*)**. To determine whether macrophage maturation is affected by OGT, qRT-PCR analysis was performed and similar levels of *F4/80*, a macrophage marker, was observed in WT and OGT KO BMDMs **(Fig. S8*E*)**, demonstrating that *LyzM*-Cre-mediated OGT KO does not affect monocyte-macrophage differentiation. GSEA comparing M1- and M2-activated pathways between WT and OGT KO BMDMs showed that two pathways, inflammatory response and signaling receptor binding, were significantly enhanced in M1-polarized OGT KO BMDMs **(Fig. S8*F* and *G*)**, suggesting that OGT may suppress macrophage M1 polarization by inhibiting signaling pathways involved in an inflammatory response.

To provide additional insights into the mechanism by which OGT regulates macrophage M1 polarization, top DEGs between WT and OGT KO BMDMs in the M1 group were shown in a Volcano plot **(Fig. 6*C*)**. Among the top up-regulated DEGs in OGT KO BMDMs, genes closely related to M1 polarization including *Il12b*, *Ccl22*, *Nos2*, *Ifng*, *Ccr7*, and *Ifnb1* were found. A large portion of the up-regulated DEGs including *Clic5*, *Dnase1l3*, *Kynu*, *Adra2b*, *Rasgrf1*, *Tspan10*, *Dll4*, *Hamp*, and *Gpihbp1* have been known to play important roles in macrophage M1 polarization. Also, a small set of genes known to be involved in macrophage regulation including *Mmp9*, *Dcstamp*, *Cyp2s1*, and *Mgat5b* were identified in the top down-regulated DEGs **(Fig. 6*C*)**. Together, these results

demonstrate a profound role of OGT-mediated transcriptional rewiring in the suppression of macrophage pro-inflammatory polarization.

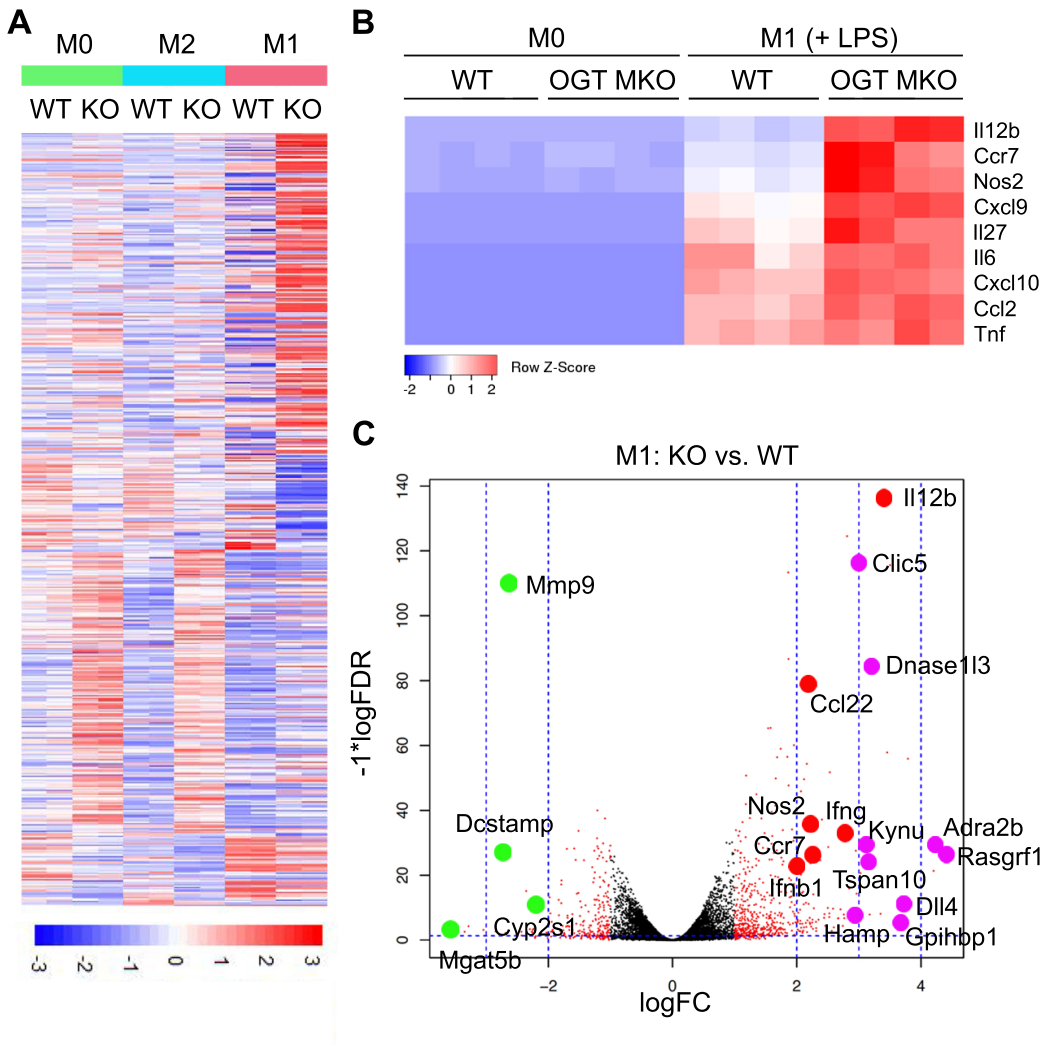

Fig. 6. RNA sequencing analysis reveals a preferential regulation of macrophage M1 polarization by OGT. (*A*) Heat map showing the differentially expressed genes (DEGs) between WT and OGT KO BMDMs, where colors indicate counts per million (cpm) values scaled by row (n =4). (*B*) Heat maps of expression levels of M1 macrophage markers determined by RNA sequencing. (*C*) Volcano plot showing top DEGs between M1-polarized WT and OGT KO BMDMs. Red dot-labelled genes are up-regulated in OGT KO BMDMs and are closely related to M1 polarization. Purple and green dot-labelled genes have known functions related to M1 polarization and are up- and down-regulated in OGT KO BMDMs, respectively.

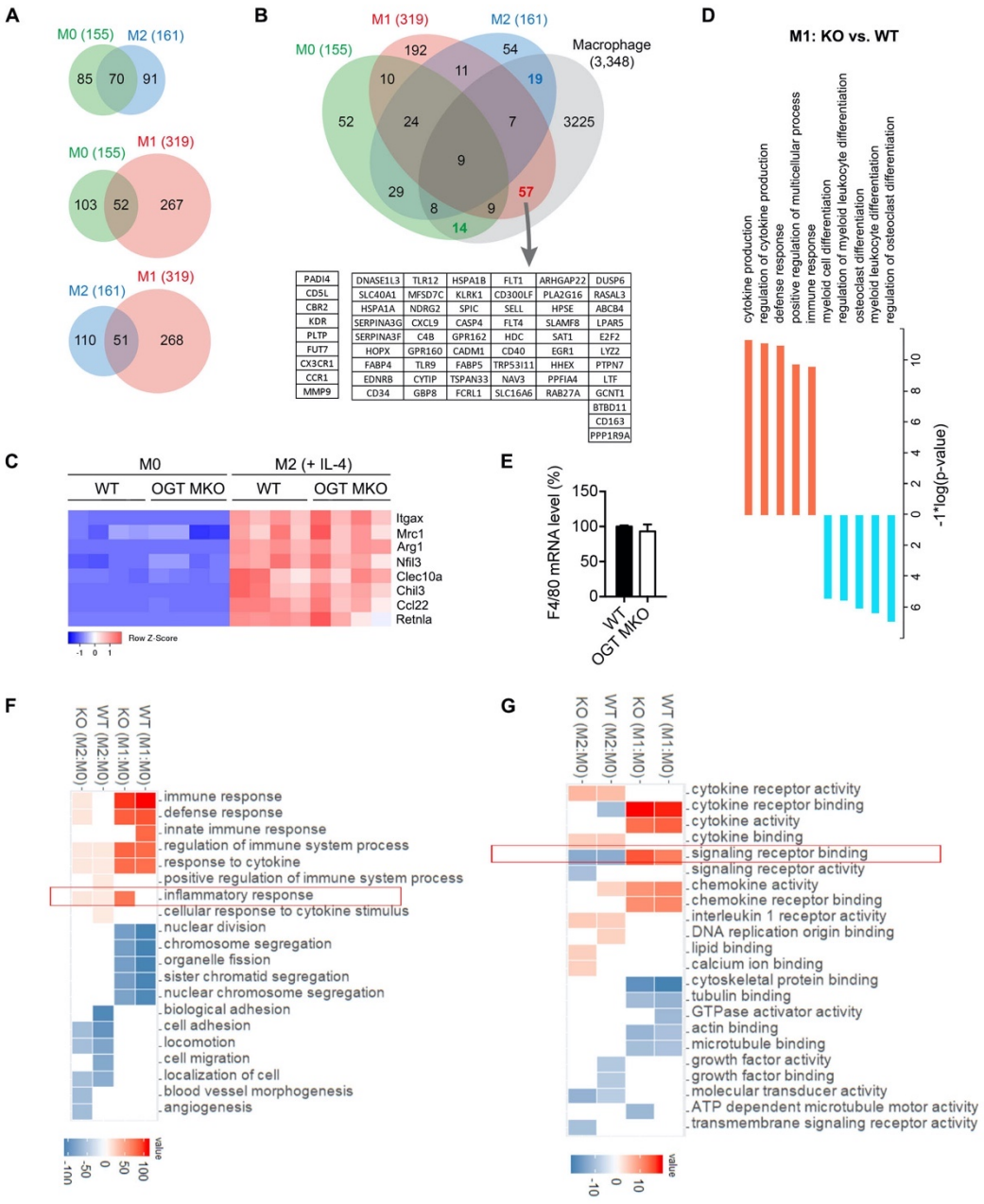

Figure S8. RNA sequencing analysis of M1- and M2-polarized WT and OGT KO BMDMs. (*A*) Venn diagram showing the overlap of DEGs (between WT and OGT KO BMDMs) between different polarization groups (M0 and M2; M0 and M1; and M2 and M1). (*B*) Venn diagram showing the overlap among DEGs (between WT and OGT KO BMDMs) from different polarization groups and macrophage-related genes. (*C*) Heat maps of expression levels of M2 macrophage markers determined by RNA sequencing. (*D*) Gene

set enrichment analysis (GSEA) of DEGs between M1-polarized WT and OGT KO BMDMs for Gene Ontology terms. x axis indicates –log10-transformed p-values of GSEA, multiplied by +1 and -1 for up- and down-regulated pathways, respectively. (*E*) F4/80 mRNA levels in in vitro differentiated WT and OGT KO BMDMs (n = 6). (*F* and *G*) Heat maps showing the differentially regulated biological (*F*) and molecular (*G*) pathways in M1- and M2-polarized WT and OGT KO BMDMs, where cell colors in the heatmap show –log10-transformed p-values of GSEA, multiplied by +1 and -1 for up- and down-regulated pathways, respectively. The most up-regulated pathway in each analysis was marked with a red box over the heatmap.

OGT inhibits macrophage pro-inflammatory activation by suppressing mTORC1/S6K1 signaling.

To understand the molecular mechanism by which *O*-GlcNAc signaling suppresses pro-inflammatory macrophage activation, we assessed the activation of several signaling pathways essential for macrophage pro-inflammatory polarization in WT and OGT KO BMDMs. We observed loss of OGT significantly enhanced LPS-induced activation of mTORC1/ribosomal protein S6 kinase beta-1 (S6K1) and NF-κB signaling but not the activation of ERK, JNK, AKT, and p38 signaling **(Fig. 7*A*)**. Moreover, TMG treatment suppressed LPS-induced S6K1 activation in BMDMs **(Fig. S9*A*)**. To determine the role of NF-κB and mTORC1/S6K1 signaling in OGT-mediated macrophage pro-inflammatory polarization, we first treated WT and OGT KO BMDMs with PF-04708671 (S6K1 inhibitor) and rapamycin (mTORC1 inhibitor), and then with LPS to induce pro-inflammatory M1 polarization. qRT-PCR analysis showed that blocking mTORC1/S6K1 signaling, but not NF-κB signaling, completely abolished the enhancement of *Nos2* and *Il-6* expression in OGT KO macrophages upon LPS stimulation, suggesting that OGT suppresses macrophage M1 polarization by inhibiting mTORC1/S6K1 pathway **(Fig. 7*B*, *C* and S9*B-E*)**.

To determine how OGT regulates mTORC1 signaling, we first tested if tuberous sclerosis complex 2 (TSC2), a key regulator of mTORC1 signaling, can be modified by *O*-GlcNAcylation. Our previous proteome-wide analysis of OGT-binding proteins in HEK 293T cells showed that TSC2 is among the 853 putative OGT-binding proteins (145) **(Fig. S9*F*)**. However, we were not able to detect any notable *O*-GlcNAcylation on TSC2, even in OGT-overexpressing cells **(Fig. S9*G*)**. Moreover, the levels of TSC2 phosphorylation on multiple sites were not changed in OGT KO macrophages **(Fig. S9*H*)**, suggesting that OGT may not affect TSC2 activity. S6K1 is a major mTORC1 downstream signaling molecule. A previous study showed that ribosomal protein S6 kinase-like 1 (S6LK), which

shares ~40% homology with S6K1, can be modified by *O*-GlcNAcylation (166). We observed a robust interaction between exogenous OGT and S6K1 in HeLa cells and RAW 264.7 cells **(Fig. 7*D* and S10*A*)**. OGT overexpression in HeLa cells and RAW 264.7 cells led to enhanced *O*-GlcNAcylation and decreased serine phosphorylation on S6K1 **(Fig. 7*E* and S10*B*)**, indicating a competition between S6K1 *O*-GlcNAcylation and phosphorylation. We then sought to identify the glycosylation sites on S6K1. Based on a list of potential *O*-GlcNAcylation sites predicted by two independent online computational prediction analyses (167, 168), a series of S6K1 single-site mutants were generated and how these mutations affect overall S6K1 *O*-GlcNAcylation was determined. The results showed that the mutation of serine 489 to alanine (S489A) largely eliminated overall S6K1 *O*-GlcNAcylation in HeLa cells and RAW 264.7 cells **(Fig. 7*F* and S10*C-E*)**, indicating that serine 489 is the primary site for S6K1 *O*-GlcNAcylation.

To establish the functional relevance of S6K1 *O*-GlcNAcylation in macrophage activation, we examined the effect of S6K1 *O*-GlcNAcylation on S6K1 phosphorylation in RAW 264.7 cells. The results showed that eliminating S6K1 serine 489 *O*-GlcNAcylation enhanced S6K1 phosphorylation at serine 418 and threonine 229 **(Fig. 7*G*)**, supporting the notion that loss of S6K1 *O*-GlcNAcylation at serine 489 promotes S6K1 phosphorylation at the C-terminus autoinhibitory domain, which further facilitates phosphorylation and activation of its N-terminal kinase domain (169-171). Consistently, LPS-induced pro-inflammatory M1 polarization was enhanced by 40-70% in RAW 264.7 cells overexpressing HA-S6K1-S489A mutation, as compared to HA- and HA-S6K1-overexpressing cells **(Fig. 7*H*, and S10*F-H*)**. These studies indicate that OGT suppresses macrophage pro-inflammatory polarization by modulating S6K1 *O*-GlcNAcylation/phosphorylation and S6K1 activation **(Fig. 7*I*)**.

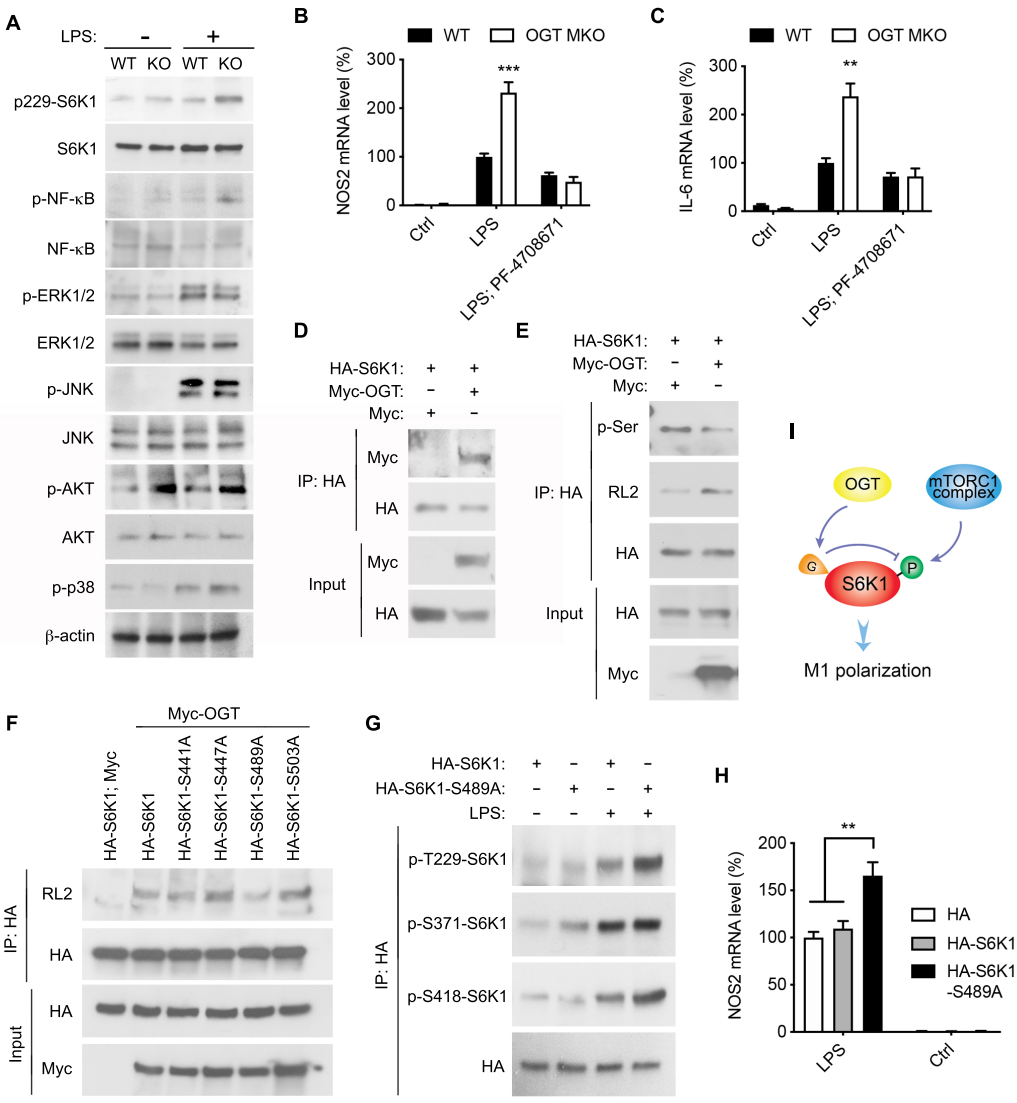

Figure 7. OGT inhibits macrophage pro-inflammatory polarization by suppressing mTORC1/S6K1 signaling. (*A*) Western blot analysis showing the activation of S6K1, NF-κB, ERK, JNK, p38 MAPK, AKT in unstimulated and LPS-stimulated (30 minutes) WT and OGT KO peritoneal macrophages. (*B* and *C*) *Nos2* and *Il-6* mRNA levels in unstimulated, LPS-stimulated, and PF-04708671-pretreated LPS-stimulated WT and OGT KO BMDMs (n = 4). (*D*) Immunoprecipitation (IP) and western blot analysis showing the interaction between exogenously expressed HA-S6K1 and Myc-OGT in HeLa cells. (*E*) IP and western blot analysis showing that OGT overexpression enhances S6K1 *O*-GlcNAcylation

and decreases S6K1 serine phosphorylation in HeLa cells. (*F*) IP and western blot analysis showing that serine 489 to alanine (S489A) mutation in S6K1 greatly abolished the overall *O*-GlcNAcylation on S6K1 in HeLa cells. (*G*) IP and western blot analysis showing that S489A mutation in S6K1 enhanced LPS-induced S6K1 phosphorylation on Threonine 229 (T229) and S418 in RAW 264.7 cells. (*H*) *Nos2* mRNA levels in untreated and LPS-stimulated RAW 264.7 cells overexpressing HA, HA-S6K1 and HA-S6K1-S489A (n = 4-6). (*I*) Molecular model for OGT function in mTORC1/S6K1 signaling. Data are shown as mean ± SEM. $^{**}p < 0.01$ by two-way ANOVA with Dunnett multiple comparisons for (*H*). $^{**}p < 0.01$, $^{***}p < 0.001$ by unpaired Student's t-test for other panels.

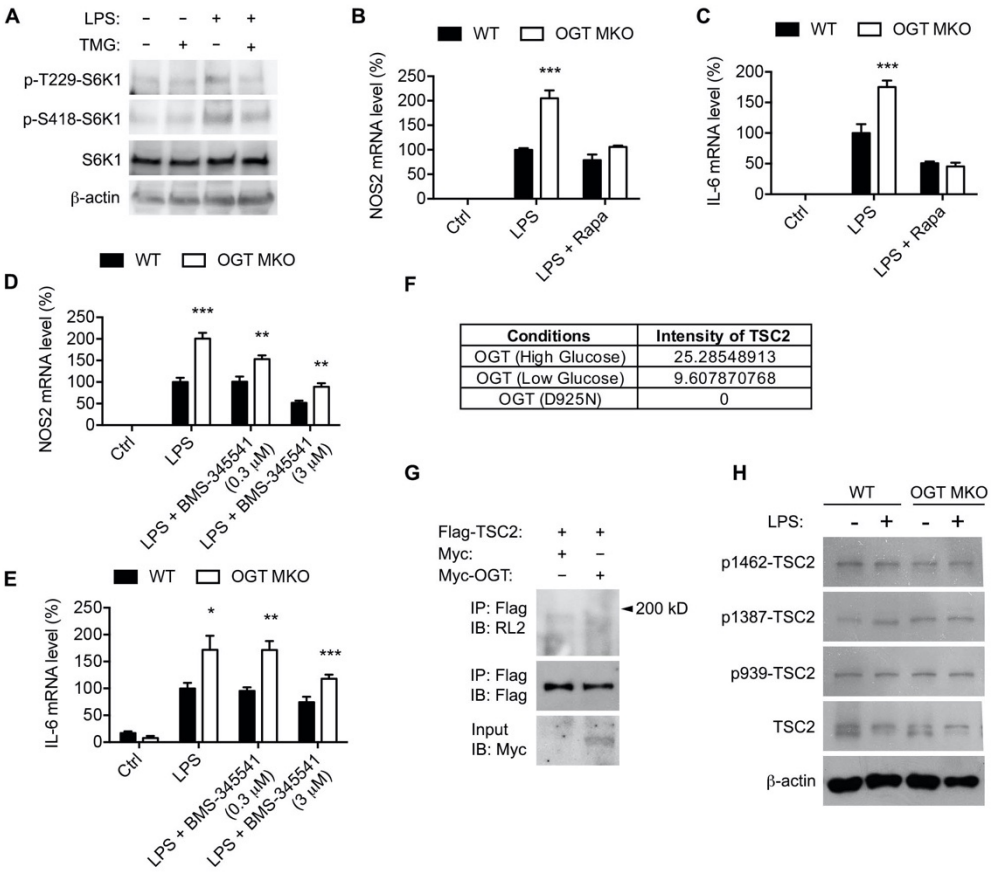

Figure S9. Suppressing NF-κB signaling does not rescue the enhanced M1 polarization in OGT KO macrophages. (*A*) Western blot analysis of S6K1 and its phosphorylation in untreated and TMG-pretreated BMDMs. LPS treatment (30 minutes) was used to stimulate M1 polarization. (*B* and *C*) *Nos2* and *Il-6* mRNA levels in unstimulated, LPS-stimulated, and rapamycin (Rapa)-pretreated LPS-stimulated WT and OGT KO peritoneal macrophages (n = 4-8). (*D* and *E*) *Nos2* and *Il-6* mRNA levels in unstimulated, LPS-stimulated, and BMS-345541-pretreated LPS-stimulated WT and OGT KO peritoneal macrophages. BMS-345541, an IκB kinase inhibitor, was used to inhibit NF-κB signaling (n = 6). (*F*) Intensities of Tuberin (TSC2) binding to OGT under various conditions determined by our proteome-wide analysis of OGT-binding proteins in HEK 293T cells. (*G*) Immunoprecipitation (IP) and western blot analysis showing no interaction was found between exogenously expressed Flag-TSC2 and Myc-OGT in HEK 293T cells.

(*H*) Western blot analysis of TSC2 and its phosphorylation in unstimulated and LPS-stimulated (30 minutes) WT and OGT KO peritoneal macrophages. Data are shown as mean ± SEM. *$p < 0.05$, **$p < 0.01$, ***$p < 0.001$ by unpaired Student's t-test.

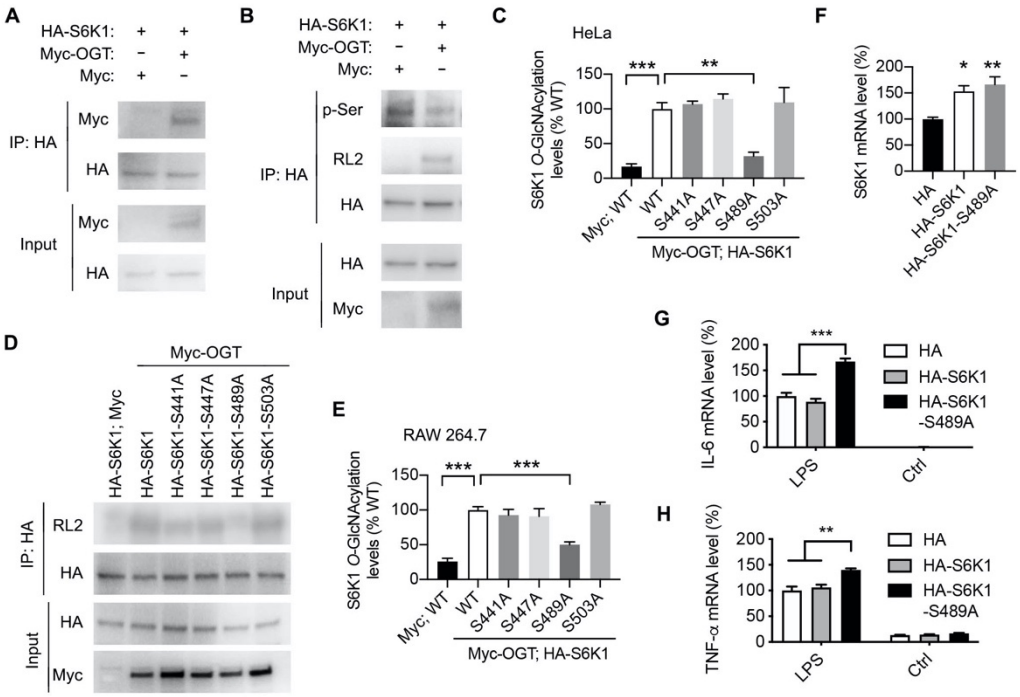

Figure S10. OGT inhibits macrophage pro-inflammatory polarization by regulating S6K1. (*A*) IP and western blot analysis showing the interaction between exogenously expressed HA-S6K1 and Myc-OGT in RAW 264.7 cells. (*B*) IP and western blot analysis showing that OGT overexpression enhances S6K1 *O*-GlcNAcylation and decreases S6K1 serine phosphorylation in RAW 264.7 cells. (*C*) Statistical analysis showing that serine 489 to alanine (S489A) mutation in S6K1 largely abolished the overall *O*-GlcNAcylation on S6K1 in HeLa cells (n = 3). (*D* and *E*) IP (*D*) and statistical analysis (*E*) showing that S489A mutation in S6K1 greatly abolished S6K1 *O*-GlcNAcylation in RAW 264.7 cells (n = 3). (*F*) *S6K1* mRNA level in RAW 264.7 cells with ectopically expressed HA, HA-S6K1 and HA-S6K1-S489A (n = 4). (*G* and *H*) *Il-6* and *TNF-α* mRNA levels in untreated and LPS-stimulated RAW 264.7 cells overexpressing HA tag, HA-S6K1 and HA-S6K1-S489A (n = 4-6). Data are shown as mean ± SEM. *p < 0.05, **p < 0.01 by one-way ANOVA with Dunnett multiple comparisons for (*F*). **p < 0.01, ***p < 0.001 by two-way ANOVA with Dunnett multiple comparisons for other graphs.

DISCUSSION

In this study, we demonstrate that macrophage *O*-GlcNAc signaling plays a profound role in suppressing adipose tissue inflammation and insulin resistance. Recent studies have expanded our knowledge about the functional and molecular integration of metabolic and inflammatory pathways. Hyperglycemia and energy surplus associated with obesity and metabolic syndrome have been shown to promote inflammatory responses through various mechanisms (172, 173). Changes in glucose uptake, glycolysis, and UDP-GlcNAc biosynthesis were observed during macrophage polarization (130, 131). Additionally, free fatty acids have been shown to activate inflammatory pathways and impair insulin action in adipose tissue (174). These findings prompted us to postulate that nutrient-sensing *O*-GlcNAc signaling serves as a link between overnutrition and insulin resistance by regulating macrophage function in metabolic tissues. However, only few studies have attempted to directly evaluate the role of *O*-GlcNAc signaling in macrophage activation and contradictory results were reported (175-177). Here, using in vitro and in vivo models, we demonstrate that *O*-GlcNAc signaling suppresses macrophage pro-inflammatory M1-like polarization and is dispensable for anti-inflammatory M2-like polarization, which supports an immunosuppressive role of *O*-GlcNAc signaling in macrophage activation.

Increasing evidence has established a causative link between pro-inflammatory macrophage and insulin resistance in both rodents and human (50, 155). Previous studies have shown that suppressing macrophage pro-inflammatory activation or entirely depleting the macrophage population is protective against diet-induced metabolic dysregulation (178, 179). Consistent with this, we found that genetic ablation of OGT in macrophages results in increased adipose tissue inflammation and excessive adipose tissue lipolysis, thus leading to increases in ectopic lipid accumulation and whole-body insulin resistance. Our study provides compelling evidence for the existence of a

protective mechanism against inflammation through *O*-GlcNAc signaling in obesity. *O*-GlcNAc signaling enables macrophages to sense external nutrients and restrains macrophage pro-inflammatory activation, which contributes to adipose tissue and whole-body metabolic homeostasis. We speculate that macrophage *O*-GlcNAc signaling is part of a homeostatic mechanism maintaining metabolic homeostasis at the early stage of obesity. However, pro-inflammatory stimuli, such as adipocyte cell death and pro-inflammatory cytokines secreted by other cells, are aggravated by prolonged HFD feeding. Eventually, the protective mechanism is pushed to the limit and becomes dysfunctional in severely obese animals. Consistent with this idea, a study showed that pro-inflammatory macrophages in mouse epididymal fat appear 3 weeks after the initiation of HFD feeding. In contrast, the accumulation of neutrophils peaks at day 3 after initiating HFD feeding (180). These results suggest that the pro-inflammatory activation of macrophages is inhibited at an early stage of exposure to excess amounts of nutrients.

mTOR signaling lies at the core of nutrient-sensing and inflammatory pathways (181). Previous studies implicate that TSC1, an upstream regulator of mTORC1, orchestrates macrophage M1 and M2 activation via separate pathways. Loss of TSC1 promotes M1-like activation by stimulating the ERK pathway, while inhibiting M2-like activation by suppressing the ERK and C/EBPβ pathways (182, 183). Several studies have suggested that obesity is associated with increased mTOR activity, and deficiency of the downstream mediator S6K1 can protect mice against diet- and age-induced insulin resistance (184, 185). The current study has identified OGT as a key regulator of the mTOR/S6K1 pathway. We have shown that *O*-GlcNAcylation suppresses mTORC1 signaling by directly regulating S6K1. S6K1 *O*-GlcNAcylation inhibits sequential phosphorylation required for kinase activation, resulting in suppression of pro-inflammatory gene transcription. Suppression of mTORC1/S6K1 pathway abrogates the effect of OGT deletion on LPS-induced M1 activation, suggesting that S6K1 is integral to

OGT-mediated macrophage regulation. Therefore, our study provides novel mechanistic insight into the regulation and the function of mTORC1/S6K1 pathway in immunometabolism.

Macrophages display considerable plasticity with M1 and M2 activation states at two extremes. How macrophages acquire diverse activation states in response to metabolic cues is still largely unknown. A previous study showed that mTOR/MYC signaling enhances *O*-GlcNAc signaling by promoting OGT protein expression (186). The AMP-activated protein kinase (AMPK) pathway is the other nutrient-sensing pathway involved in macrophage polarization, and AMPK can negatively regulate the mTOR pathway (187). Furthermore, there is evidence that *O*-GlcNAcylation of AMPK regulates its enzymatic activity (188). Taken together, it is likely that OGT, mTORC1 and AMPK pathways form a complex nutrient-sensing network that underpins a spectrum of macrophage activation states.

In summary, this study demonstrates *O*-GlcNAc signaling as a novel homeostatic regulator at the interface of inflammation and metabolism. The results have important implications for our understanding of the integration of metabolism and immunity, an evolutionary need for survival (189). Future studies to explore how macrophage *O*-GlcNAc signaling integrates nutritional signals to dictate the immune response would help develop new immunomodulatory strategies to treat chronic metabolic diseases. Glutamine and glucosamine, the popular nutritional supplements implicated in immunometabolism, both are known to fuel the hexosamine biosynthetic pathway and promote *O*-GlcNAc signaling. Studies have shown that human adipose glutamine levels correlate inversely with fat mass and white fat inflammation (190). Glutamine supplementation attenuates adipose tissue inflammation and reduces metabolic risk in rodents (190, 191). Supplementing glucosamine in HFD-fed rats improves glucose metabolism and reduces visceral fat mass (192). Further investigation is warranted to determine whether *O*-GlcNAc signaling in

immune cells is involved in these processes. It is worth noting that glucosamine also protects against sepsis-induced tissue injury and septic death in mouse and zebrafish models (177). Therefore, the immunosuppressive function of *O*-GlcNAc signaling may have broader implications in both obesity-associated morbidity and immune-related diseases.

METHODS

Animals

Ogt^{flox} mice were crossed with *LyzM*-Cre mice to generate *Ogt*^{flox} *LyzM*-Cre-/- (WT) and *Ogt*^{flox} *LyzM*-Cre+/- (OGT MKO) mice. *Ogt*^{flox} mice were described previously (193) and were kindly provided by Dr. Steven Jones at the University of Louisville. *LyzM*-Cre mice were from The Jackson Laboratory (Catalog No. 004781). All mice were housed in a 12 h: 12 h light-dark cycle at 25 °C. Unless otherwise specified, mice were free to access water and food and were maintained on a normal chow diet. High fat fed mice were given *ad libitum* access to a high fat diet (D12492, Research Diets) when they were 6-9 weeks old. Male mice were used for the experiments. All animal experiments were performed in accordance with protocols approved by Yale University's Institutional Animal Care and Use Committee. Body weights were recorded every week. Body composition was measured by nuclear magnetic resonance relaxometry using an EchoMRI system. Freshly dissected tissues were used to determine tissue weights. For metabolic cage analysis, single-housed mice were first acclimated in metabolic chambers for 3 days. Then gas exchange, energy expenditure, and physical activity were recorded for 4 days. Average daily food intake of each mouse was measured by weighing the food every day at the same time continuously for 3 days.

Biochemical Analyses

Blood glucose concentrations were measured by using a Nova Max Glucometer or the YSI 2700 Select Biochemistry Analyzer. Plasma insulin concentrations were measured by ELISA (Millipore) or radioimmunoassay (Millipore). Plasma non-esterified fatty acid (NEFA) and triglyceride concentrations were measured by using a Wako kit and the Sekisui triglyceride-SL reagent respectively. Serum inflammatory cytokine (IL-6 and TNF-α) concentrations were measured by ELISA (BD OptEIA) assay.

Tissue Analyses

Liver and skeletal muscle triglyceride contents were measured as previously described (194). Briefly, lipids were extracted from liver and gastrocnemius muscle using 2:1 chloroform:methanol and measured by using the Sekisui triglyceride-SL reagent spectrophotometrically. Tissue acetyl-CoA, diacylglycerols, and ceramide concentrations were measured by liquid chromatography/mass spectrometry/mass spectrometry (LC-MS/MS) (19, 50, 195). For the measurement of inflammatory cytokine (IL-6 and TNF-α) levels, tissues were first homogenized in PBS and then centrifuged at 4°C to obtain supernatant. The supernatants were then analyzed by ELISA (BD OptEIA) assay.

Glucose tolerance test and insulin tolerance test

For glucose tolerance test, mice were fasted overnight and injected intraperitoneally with a single dose of glucose (1.5 g/kg body weight), then tail-vein blood was taken at designated times and blood glucose levels were determined using a Nova Max Glucometer. For insulin tolerance test, mice were fasted for 6 hours in the morning and injected intraperitoneally with a single dose of insulin (1 U/kg body weight for all NC-fed mice and 1.5 U/kg body weight for all HFD-fed mice), then blood glucose levels were measured as described above.

Basal and hyperinsulinemic-euglycemic clamp study

An indwelling catheter was placed in the jugular vein seven days before the clamp study. Mice were fasted overnight the day before the study. To measure whole-body lipolysis, a 120 minutes basal infusion with [3-^{3}H] glucose (HPLC purified; PerkinElmer) and [$^{13}C_{16}$] potassium palmitate (Cambridge Isotopes) was performed as described (50). Blood was collected from the tail vein at 120 minutes. After the basal period, a 140-minute

hyperinsulinemic-euglycemic clamp was performed by infusing a continuous rate of insulin (10 mU/[kg-min] for 3 minutes and 3 mU/[kg-min] for 140 minutes) and variable rates of 20% dextrose to maintain euglycemia along with the infusion of [$^{13}C_{16}$] sodium palmitate, while periodic tail vein blood sampling was performed. In the last 55 minutes of the clamp period, 10 µCi 2 deoxy-[1-^{14}C] glucose (2-DG) was injected to measure tissue-specific glucose uptake. At 140 minutes, a final blood sample was collected and the mice were euthanized by intravenous injection of sodium pentobarbital. Liver, gastrocnemius muscle, white and brown adipose tissues were freeze-clamped in pre-cooled in liquid nitrogen and stored at -80 °C for further analyses.

Flux measurements

The specific activity of [3-^{3}H] glucose in plasma samples collected at the steady state during basal and clamp study was measured by using a liquid scintillation counter as previously described (50). During basal, endogenous glucose production (EGP) is the only source of glucose appearance whose rate equals to glucose turnover rate at steady state, therefore EGP = glucose turnover rate. During clamp, EGP and glucose infusion together contribute to glucose appearance, therefore EGP = glucose turnover rate - glucose infusion rate. [$^{13}C_{16}$] palmitate enrichments were measured using gas chromatography-mass spectrometry (GC/MS) as previously described (196). Palmitate turnover = ([$^{13}C_{16}$] palmitate tracer enrichment/[$^{13}C_{16}$] palmitate plasma enrichment-1) x infusion rate. The fatty acid turnover was measured by correcting for the percentage of palmate in total fatty acids (197).

Cold challenge

For thermogenesis studies, single-housed mice were transferred from room temperature to 4 °C for 6 hours. Core body temperature was examined in conscious mice

using a rectal thermometer. During this process, food was removed but the mice had free access to water and the bedding material was left in the cage.

Cell culture and treatments

All cells were cultured at 37 °C in 5% CO_2. RAW 264.7, HeLa, and HEK 293T cells were from the American Type Culture Collection and were cultured in DMEM (GIBCO) supplemented with 10% FBS (GIBCO). Plasmids were transfected into cells by using FuGENE HD (Promega) or jetPEI-Macrophage (Polyplus-transfection). For primary adipocyte culture, the stromal vascular fraction (SVF) of the mouse epididymal white fat was isolated, cultured and differentiated into adipocytes as described previously (198). Murine resident peritoneal macrophages and bone marrow-derived macrophages (BMDMs) were isolated and generated as described (199). To test the effects of OGA inhibitors, macrophages were pretreated with 10 μM TMG, 6-Ac-Cas, or PUGNAc for 6 hours. Then LPS was added (in the presence of OGA inhibitors) to stimulate M1 polarization. Similarly, PF-04708671 (1 μM), BMS-345541, and rapamycin (100 nM) were added 1 hour prior to the LPS treatment.

Macrophage polarization and phagocytosis assay

BMDMs and peritoneal macrophages were treated with LPS (100 ng/ml, unless specified otherwise) to induce M1 polarization. A higher concentration of LPS (1 μg/ml) was used to induce M1 polarization in RAW 264.7 cells. IL-4 (10 ng/ml) was used to induce M2 polarization in BMDMs and peritoneal macrophages. Unless otherwise stated, macrophages were collected 30 minutes later for cell signaling analysis or 12 hours later for qRT-PCR analysis. For the phagocytosis assay, BMDMs were cultured in M-CSF-free medium for 24 hours and then incubated with opsonized fluorescently labeled zymosan A bioparticles (Thermo Fisher) for 1 hour at 37°C. Then phagocytosis was stopped by adding

cold PBS. BMDMs were washed, fixed, and counterstained with DAPI for fluorescence microscopy.

Quantitative real-time PCR and RNA-seq

Total RNA was isolated from untreated, LPS-treated, and IL-4-treated (12 hours unless otherwise stated) WT and OGT KO BMDMs using TRIzol Reagent (Invitrogen). Then total RNA samples were used for cDNA synthesis (iScript cDNA Synthesis Kit) and SYBR Green-based quantitative real-time PCR analysis (Bio-Rad). The level of *36b4* was used as internal control. Primer sequences are: *36b4*-F (5'-AGATGCAGCAGATCCGCAT-3'), *36b4*-R (5'-GTTCTTGCCCATCAGCACC-3'); *Ogt*-F (5'-AAGAGGCACGCATTTTTGAC-3'), *Ogt*-R (5'-ATGGGGTTGCAGTTCGATAG-3'); *Oga*-F (5'-CTCAGAGGCTGAGAAAATAATGTTGAG-3'), *Oga*-R (5'-AAGGGAAGTTGGCAAGGAAAGT-3'); *Nos2*-F (5'-TTCTGTGCTGTCCCAGTGAG-3'), *Nos2*-R (5'-TGAAGAAAACCCCTTGTGCT-3'); *Il6*-F (5'-GAGGATACCACTCCCAACAGACC-3'), *Il6*-R (5'-AAGTGCATCATCGTTGTTCATACA-3'); *TNF-α*-F (5'-CATCTTCTCAAAATTCGAGTGACAA-3'), *TNF-α*-R (5'-TGGGAGTAGACAAGGTACAACCC-3'); *Ccl2*-F (5'-ATTGGGATCATCTTGCTGGT-3'), *Ccl2*-R (5'-CCTGCTGTTCACAGTTGCC-3'); *pro-Il1b*-F (5'-AAGAGCTTCAGGCAGGCAGTATCA-3'), *pro-Il1b*-R (5'-ATGAGTCACAGAGGATGGGCTCTT-3'); *Arg1*-F (5'-TTTTTCCAGCAGACCAGCTT-3'), *Arg1*-R (5'-AGAGATTATCGGAGCGCCTT-3'); *Clec10*-F (5'-CTCTGGAGAGCACAGTGGAG-3'), *Clec10*-R (5'-ACTTCCGAGCCGTTGTTCT-3'); *Retnla*-F (5'-CTGGATTGGCAAGAAGTTCC-3'), *Retnla*-R (5'-CCCTTCTCATCTGCATCTCC-3'); *Chi3l3*-F (5'-TTTCTCCAGTGTAGCCATCCTT-3'), *Chi3l3*-R (5'-TCTGGGTACAAGATCCCTGAA-3'). For RNA-seq, total RNA was isolated by using the RNeasy Plus Mini Kit (QIAGEN). RNA integrity was examined by

electrophoresis for quality control purpose. Then the RNA samples were used to generate eukaryotic transcriptome libraries. The sequencing was performed on the HiSeq PE-150 platform with 30m reads. For RNA-seq analysis, total RNA-seq reads were mapped to iGenome UCSC MM10 gene annotation using TopHat (200) version 2.1.0. Mapped reads were summarized for each gene using HTSeq (201) version 0.9.1. Differential expression analysis was implemented using edgeR (202, 203) version 3.22.5 with FDR = 0.05 and at least 1 absolute log2 fold change. Gene set enrichment analysis was implemented using the ToppGene Suite (https://toppgene.cchmc.org/).

Western blotting and immunoprecipitation

Cells were lysed in lysis buffer containing 1% Nonidet P-40, 50 mM Tris-HCl, 150 mM NaCl, 0.1 mM EDTA together with proteinase inhibitors and protein phosphatase inhibitors. Protein lysates were then denatured by heating in laemmli sample buffer containing SDS and β-mercaptoethanol, resolved by SDS-PAGE, and transferred to PVDF membranes (Millipore). The membranes were blocked with 5% skimmed milk or bovine serum albumin (BSA), incubated with primary antibodies first, and then with horseradish peroxidase-conjugated secondary antibodies (Cell Signaling Technology). Proteins were visualized with ECL western blotting substrate (Pierce). For protein kinase Cε (PKCε) and PKCθ translocation, cytoplasm and plasma membrane fractions were separated by ultracentrifugation as previously described (67, 71). For immunoprecipitation, cell lysates were incubated with antibody-conjugated agarose beads at 4 °C overnight. The beads were then washed and boiled in laemmli sample buffer, and the proteins were examined by western blotting.

Reagents and plasmids

Antibodies against *O*-GlcNAc [RL2] (ab2739), phosphoserine [PSR-45], NaK-ATPase [464.6] and OGA (EPR7154(B)) (Abcam); OGT (D1D8Q), JNK1 (2C6), phospho-JNK (81E11), phospho-Akt (Ser473) (587F11), phospho-Akt (Thr308) (244F9), Akt (9272), phospho-p38 (D3F9), phospho-ERK 1/2 (D13.14.4E), ERK 1/2 (137F5), phospho-TSC2 (Thr1462) (3611), phospho-TSC2 (Ser1387) (D2R3A), phospho-TSC2 (Ser939) (3615), TSC2 (D93F12), phospho-IR (Y1162) (3024), IR (3020), and GAPDH (14C10) (Cell Signaling Technology); S6K1 (DK7994), phospho-S6K1 (Thr229) (DK7994), phospho-S6K1 (Ser371) (DK3904), and phospho-S6K1 (Ser418) (AC0176) (eBioscience); NF-κB p65 (A-12), and p-NF-κB p65 (Ser 536), and Myc (9E10) (Santa Cruz Biotechnology); Flag (M2), HA (H3663), and β-actin (A5441) (Sigma-Aldrich); PKCε (610086) and PKCθ (610090) (BD Bioscience) were purchased from the indicated sources. PF-04708671, BMS-345541, and rapamycin (Cayman Chemical), TMG (Carbosynth), and PUGNAc (Sigma-Aldrich) were from indicated sources. LPS (B5S-36-01, InvivoGen), mouse IL-4 (5208, Cell Signaling Technology), IFN-γ (2728403, Millipore), and rmM-CSF (416-ML, R&D Systems) were from the indicated sources. Mammalian expression plasmids pCMV-Myc-hOGT and catalytic dead pCMV-Myc-hOGT-G598S (catalytic dead) were described and kindly provided by Dr. Xiaochun Yu at the University of Michigan. pRK7-HA-S6K1-WT encoding HA-tagged rat S6K1 was from Addgene (Plasmid #8984). HA-S6K1 mutants were generated using QuikChange II site-directed mutagenesis kit (Agilent).

Lipolysis assay

For white adipose tissue ex vivo lipolysis assay, freshly dissected adipose tissue was cut into small explants (~3 mm diameter), washed in PBS, and transferred to Krebs-Ringer buffer with 3 mM HEPES and 1% free fatty acid-free BSA and incubated in a 37 °C shaker. Media samples were collected at selected time points. The amount of free glycerol released into the medium was measured using the Free Glycerol Reagent (Sigma-Aldrich).

To determine lipolysis in cultured adipocytes, SVFs of the mouse epididymal white fat were isolated and differentiated into mature adipocytes as previously described (198). Peritoneal macrophages were plated directly on top of the adipocytes or in a transwell (0.4 μM pore size) inserted into the adipocyte culture medium. The macrophages were stimulated with LPS (100 ng/ml, 30 minutes) and then the cells were washed with PBS and incubated in phenol red-free medium. The amount of released glycerol was determined by using the Free Glycerol Reagent (Sigma-Aldrich).

Flow cytometry

For flow cytometry analysis, SVFs of mouse adipose tissues were isolated as described previously (198). In brief, mouse adipose tissue was dissected and minced into fine pieces on ice. Then, adipose tissues were digested to get single cell suspensions. Digestion buffer and mature adipocytes were removed by centrifugation. The pellets were collected, resuspend in FACS buffer (1X DPBS, 2 mM EDTA, and 1% FBS), filtered through 70 μm filters, and centrifuged again to obtain SVFs. Generally, 1×10^6 cells were used for staining. For cell surface marker staining, the following fluorochrome-conjugated antibodies from Biolegend were added: F4/80 (BM8, 1:200 dilution), CD11c (N418, 1:100), CD206 (C068C2, 1:100), MGL1 (LOM-8.7, 1:200), CCR2 (SA203G11, 1:200), and CD16/CD32 (Fc block, 93, 1:1000). Zombie NIR™ Fixable Viability Kit (Biolegend) was used to determine live cells. If intracellular staining for O-GlcNAcylation was required, cells were then fixed and permeabilized by using Fixation/Permeabilization Solution Kit (Biosciences). Cells were then washed and incubated with AlexaFluor 647-conjugated O-GlcNAc antibody (RL2, Novus Biologicals, 1:800). Stained SVFs were filtered through 40 μm filters and analyzed by a BD LSRII flow cytometer. The results were analyzed by using FlowJo.

Histology

Animals were sacrificed and tissues were collected, fixed (4% paraformaldehyde, overnight at 4 °C), dehydrated, and embedded in paraffin. Tissue sections were then prepared by using a microtome and stained with hematoxylin-eosin (H&E) staining. Blinded histological scoring of liver slides was performed by an experienced pathologist.

Whole-mount adipose tissue staining

To visualize macrophages in adipose tissue, freshly prepared whole mounted adipose tissue (~4 mm x 4 mm x 2 mm) was fixed in a mild fixative (1% paraformaldehyde, 30 minutes), penetrated in a mild detergent buffer (0.5% Tween 20, 30 minutes), and stained with Alexa Fluor 647-conjugated anti-CD11c antibody (N418, BioLegend), BODIPY FL, and DAPI. The stained tissue was mounted and imaged as described (204).

Statistical analysis

Data were plotted and statistically evaluated using GraphPad Prism version 7.0a (GraphPad Software). Results were presented as mean ± SEM. Two-condition comparisons were performed using unpaired two-tailed Student's t-test. For nonparametric comparison of means, Mann-Whitney test was used. For multiple-conditions comparisons, one-way or two-way ANOVA with Dunnett multiple comparisons was used. Differences that are statistically significant were plotted as $p < 0.05$ (∗), $p < 0.01$ (∗∗), and $p < 0.001$ (∗∗∗).

Chapter 6

Mechanisms by Which Adiponectin Reverses High Fat Diet-induced Insulin Resistance in Mice

ABSTRACT

Adiponectin has emerged as a potential therapy for type 2 diabetes mellitus, but the molecular mechanism by which adiponectin reverses insulin resistance remains unclear. Two-weeks of globular adiponectin (gAcrp30) treatment reduced fasting plasma glucose, triglyceride (TAG) and insulin concentrations and reversed whole-body insulin resistance, which could be attributed to both improved insulin-mediated suppression of endogenous glucose production and increased insulin-stimulated glucose uptake in muscle and adipose tissues. These improvements in liver and muscle sensitivity were associated with reductions in liver and muscle TAG and plasma membrane (PM) associated diacylglycerol (DAG) content and occurred independently of reductions in total ceramide content. Reductions of PM DAG content in the liver and skeletal muscle were associated with reduced PKCε translocation in liver and reduced PKCθ and PKCε translocation in skeletal muscle resulting in increased insulin-stimulated insulin receptor tyrosine1162 phosphorylation, IRS-1/IRS-2-associated PI3-kinase activity and Akt-serine phosphorylation. Both gAcrp30 and full-length adiponectin (Acrp30) treatment increased eNOS/AMPK activation in muscle and muscle fatty acid oxidation. gAcrp30 and Acrp30 infusions also increased plasma triglyceride uptake in eWAT, which could be attributed to increased lipoprotein lipase (LPL) activity. These data suggest that adiponectin and adiponectin-related molecules reverse lipid-induced liver and muscle insulin resistance by reducing ectopic lipid storage in these organs resulting in decreased membrane DAG-induced nPKC activity and increased insulin signaling. Adiponectin mediates these effects by both promoting the storage of plasma triglyceride in eWAT likely through stimulation of LPL, as well as by stimulation of AMPK in muscle resulting in increased muscle fat oxidation.[2]

[2] Other contributors to this work include Dongyan Zhang, Daniel F. Vatner, Leigh Goedeke, Sandro M. Hirabara, Ye Zhang, Rachel J. Perry, and Gerald I. Shulman

INTRODUCTION

Type 2 diabetes mellitus (T2DM) is one of the leading causes of morbidity and mortality in the adult population worldwide (82, 205) and is associated with disease in many organ systems, including nonalcoholic fatty liver disease (NAFLD) and atherosclerotic vascular disease (ASCVD) (5-7, 84). Insulin resistance plays a critical role in the pathogenesis of T2DM and metabolic syndrome. The adipokine adiponectin has emerged as a potential anti-diabetic, anti-inflammatory and anti-atherogenic factor (23, 24). Unlike adipokines such as leptin, plasma adiponectin levels are inversely correlated with adiposity and decreased in obesity, insulin resistance and T2DM (108, 109). Adiponectin is present in human plasma as full-length adiponectin (Acrp30) and as a C-terminal globular fragment (gAcrp30) (110, 118, 206). The C-terminal globular fragment is produced by proteolytic cleavage and is thought to be the pharmacologically active moiety (110). A wide variety of explanations for adiponectin's glucose-lowering and insulin-sensitizing properties has been proposed, which have been derived predominantly from *in vitro and ex vivo* studies, including: suppression of gluconeogenesis (111, 115, 207); increased 5' AMP-activated protein kinase (AMPK)/ acetyl-CoA carboxylase (ACC)-dependent fatty acid oxidation in liver and muscle (23, 115, 118, 208); and reduced hepatic ceramide content by activation of hepatic ceramidase (114). A clear, consistent model for adiponectin’s action *in vivo* is lacking, and the mechanisms by which adiponectin ameliorates insulin resistance are a matter of active debate.

The association between ectopic lipid and insulin resistance in the liver and skeletal muscle is widely recognized (13-15). Diacylglycerols (DAGs) and ceramides are the two best-studied mediators of lipid-induced insulin resistance. Ceramides have been shown to impair insulin action at the level of protein kinase B (Akt) phosphorylation, through activation of protein kinase Cζ (PKCζ) and/or protein phosphatase 2A (81, 209, 210). In contrast, plasma membrane *sn*-1,2-DAGs, which has been shown to be the key

DAG stereoisomer, impair insulin action via activation of novel PKCs (nPKCs), including PKCε in liver (17, 18, 66) and both PKCθ and PKCe in skeletal muscle (68, 211). PKCe activation subsequently impairs insulin receptor kinase (IRK) tyrosine kinase activity and PKCq activation impairs insulin signaling at the level of IRS-1/IRS-2 associated PI3-kinase activity (14, 19, 20). Insulin resistance in the liver leads to reduced insulin-stimulated hepatic glycogen synthesis and defects in insulin suppression of hepatic glucose production, while insulin resistance in the skeletal muscle leads to reduced insulin-stimulated muscle glucose transport. In the setting of white adipose tissue (WAT) insulin resistance, WAT lipolysis is resistant to suppression by insulin, leading to increased non-esterified fatty acid (NEFA) delivery to the liver and muscle, which may further promote increased liver and muscle ectopic lipid content (6, 7, 161, 212).

Given that prior studies have demonstrated that increased plasma adiponectin concentrations lead to accretion of WAT and improved glycemia in mice (213, 214), we hypothesized that the insulin-sensitizing properties of adiponectin might be due to protection against ectopic lipid deposition in insulin-responsive tissues. To address this hypothesis, we performed a comprehensive series of studies to assess the effects of two-week gAcrp30 and Acrp30 treatment on multiple metabolic fluxes using a combination of stable- and radio-labeled isotopic tracers, in a high fat diet (HFD)-fed mouse model of lipid-induced insulin resistance. Here, we demonstrate that two weeks of gAcrp30 treatment reverses whole-body insulin resistance in HFD-fed mice by reducing plasma membrane DAG content, resulting in decreased translocation of PKCε to the plasma membrane in liver and decreased PKCε/ PKCθ translocation in skeletal muscle leading to increased insulin signaling in both of these tissues. This reduction in ectopic lipid storage in liver and muscle could be attributed to increased lipoprotein lipase activity in epididymal WAT (eWAT), resulting in increased lipid uptake in eWAT, as well as activation of AMPK in muscle, which in turn promoted increased fatty acid oxidation in skeletal muscle. Taken

together, these results provide new insights into the mechanisms by which adiponectin reverses insulin resistance *in vivo*.

RESULTS

Two-week globular adiponectin treatment ameliorates lipid-induced insulin resistance

In order to examine the effect of long-term exposure to increased globular adiponectin (gAcrp30) on glucose metabolism, we performed continuous subcutaneous gAcrp30 infusions (2.5μg/day) in 12-week HFD-fed mice for two weeks. As expected, plasma adiponectin concentrations increased in the gAcrp30-treated mice compared with control mice **(Fig. 1*A*)**. To assess the effect of gAcrp30 on energy balance, metabolic cages were utilized and whole-body energy expenditure was determined by indirect calorimetry. Consistent with the lack of difference in body weight or body composition **(Fig. 1*B* and 1*C*)**, we observed no effect of gAcrp30 on whole-body oxygen consumption, carbon dioxide production, energy expenditure, caloric intake, respiratory exchange ratio, drinking or activity **(Fig. 1*D*-1*J*)**.

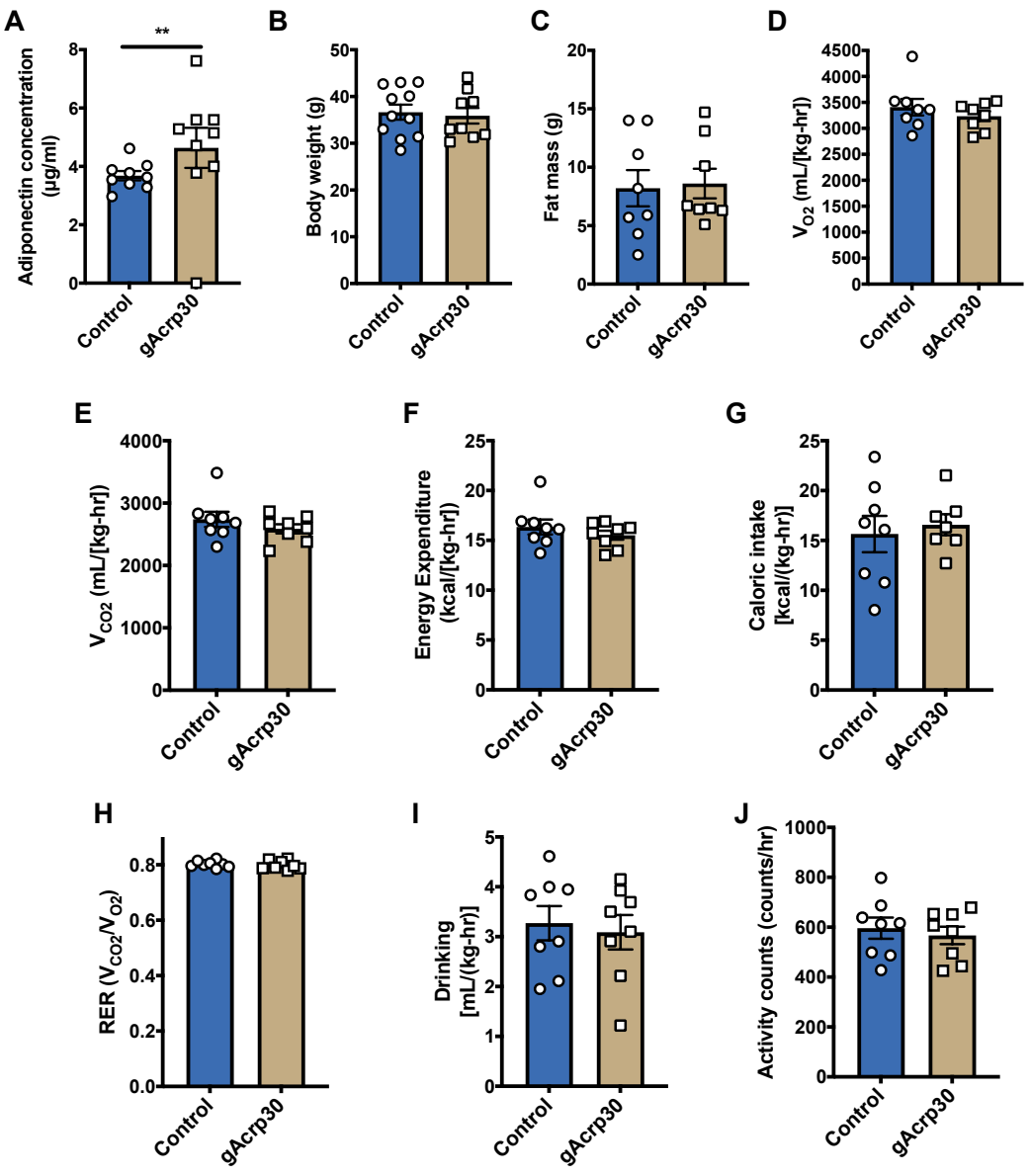

Figure 1. Two-week adiponectin treatment has no effect on whole-body energy metabolism of control and gAcrp30-treated mice. (*A*) Plasma adiponectin concentrations after overnight fasting in HFD-fed mice treated with globular adiponectin (gAcrp30) or vehicle-control for two weeks. (*B*) Body weight of control and gAcrp30-treated mice (n = 9-11). (*C*) Fat mass of control and gAcrp30-treated mice. (*D*) Whole-body oxygen consumption. (*E*) Whole-body carbon dioxide production. (*F*) Whole-body energy expenditure. (*G*) Whole-body caloric intake. (*H*) Whole-body respiratory exchange

ratio. (*I*) Drinking. (*J*) Activity Counts. Data are shown as mean ± SEM. **p < 0.01 by unpaired Student's t-test for other panels.

While gAcrp30 did not alter whole-body energy metabolism, plasma triglyceride (TAG) concentrations as well as liver TAG content and muscle TAG content were significantly reduced by 35%, 45% and 60% respectively **(Fig. 2*A*-2*C*)**. Consistent with a reduction in ectopic lipid content in liver and skeletal muscle, mice treated for two weeks with gAcrp30 exhibited a 10% reduction in plasma glucose concentrations and a 65% reduction in plasma insulin concentrations after overnight fasting **(Fig. 2*D* and 2*E*)**. In contrast, there was no difference in fasting plasma NEFA concentration between groups **(Fig. 2*F*)**. In order to determine the effects of gAcrp30 on tissue-specific insulin action, we performed hyperinsulinemic-euglycemic clamps combined with radiolabeled and stable isotopes. Basal endogenous glucose production (EGP) was reduced by 13% in the gAcrp30 group as compared with the control group **(Fig. 2*G*)**, resulting in reduced fasting plasma glucose concentrations **(Fig. 2*D*)**. During the hyperinsulinemic phase of the clamp study, gAcrp30-treated mice displayed a two-fold increase in the glucose infusion rate required to maintain euglycemia, reflecting increased whole-body insulin-sensitivity **(Fig. 2*H*-2*J*)**. The increased whole-body insulin sensitivity could be attributed to both a 2-fold increase in insulin-mediated suppression of hepatic glucose production, and a 15% increase in insulin-stimulated peripheral glucose disposal **(Fig. 2*G*, 2*K* and Fig. 2*L*)**. Specifically, our data demonstrated that glucose uptake is increased by 50-100% in all assessed tissues, including skeletal muscle, WAT and brown adipose tissue **(Fig. 2*M*-2*O*)**.

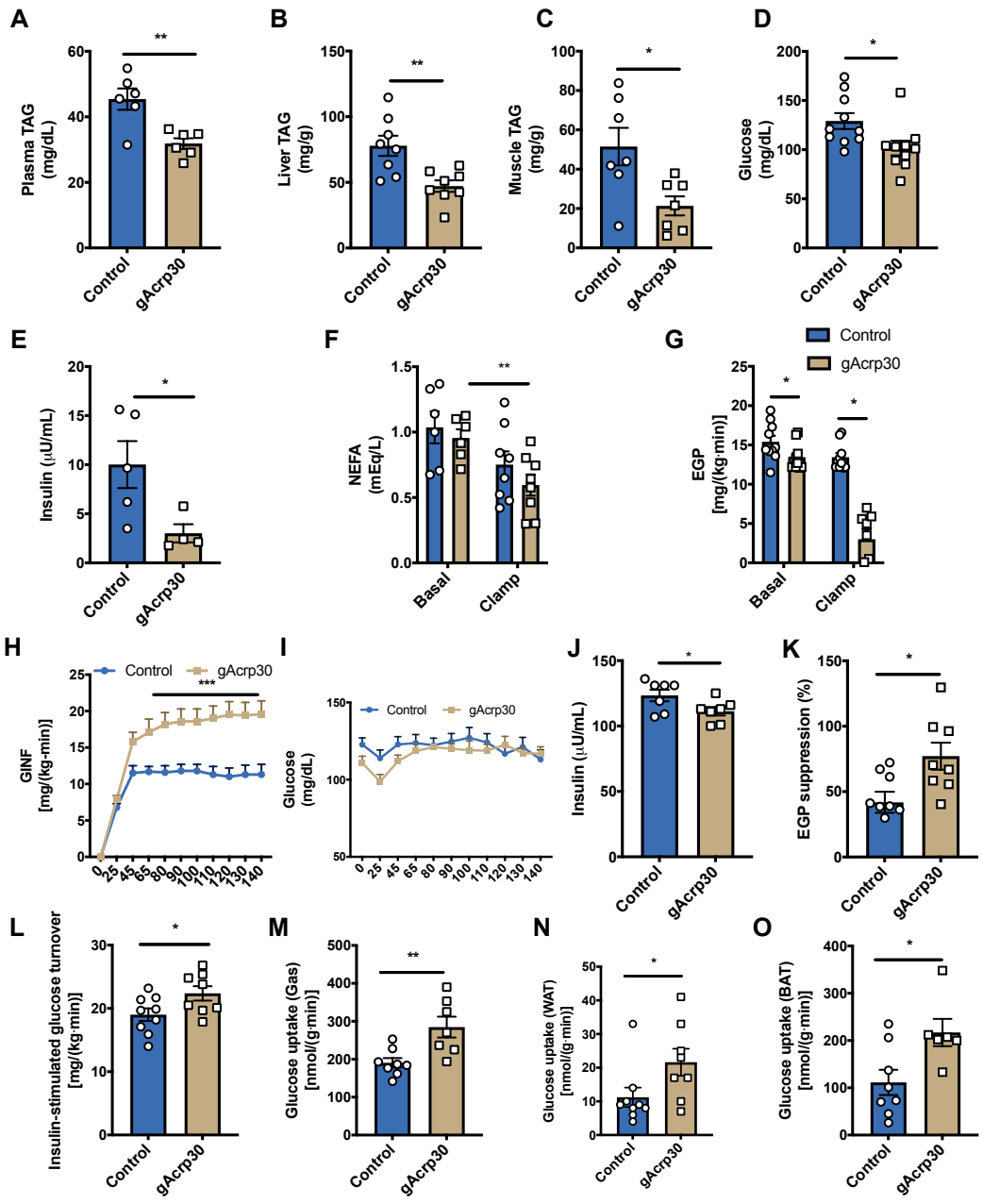

Figure 2. Globular adiponectin treatment ameliorates lipid-induced insulin resistance in high-fat diet (HFD) fed mice. (*A*) Plasma triglyceride concentrations of control and gAcrp-30 treated mice after overnight fasting. (*B*)-(*C*) Liver and muscle triglyceride content of control and gAcrp-30 treated mice. (*D*)-(*E*) Plasma glucose (n = 10) and insulin concentrations (n = 4-5) of control and gAcrp-30 treated mice after overnight fasting. (*F*) NEFA under basal and hyperinsulinemic-euglycemic conditions. (*G*)

Endogenous glucose production rate under basal and the hyperinsulinemia-euglycemia clamp states (*n* = 8-10). (*H*) Glucose infusion rate during the hyperinsulinemic-euglycemic clamp. (*I*) Glucose concentrations during the hyperinsulinemia-euglycemia clamp of control and gAcrp-30 treated mice. (*J*) Insulin concentrations after the hyperinsulinemia-euglycemia clamp. (*K*) Endogenous glucose production rate suppression during the hyperinsulinemia-euglycemia clamp. (*L*) Glucose turnover rate during the hyperinsulinemia-euglycemia clamp. (*M*)-(*O*) Insulin-stimulated glucose uptake rate in skeletal muscle, white adipose tissue and brown adipose tissue in control and gAcrp30-treated mice. Data are shown as mean ± SEM. *p < 0.05, **p < 0.01 by two-way ANOVA with Dunnett multiple comparisons for (*F*) and (*G*). *p < 0.05, **p < 0.01, ***p < 0.001 by unpaired Student's t-test for other panels.

Globular adiponectin reduces plasma membrane DAG content and nPKC activation in liver and skeletal muscle

As two weeks of gAcrp30 treatment resulted in a marked improvement in liver and muscle insulin sensitivity, we next assessed insulin signaling pathways in the liver and skeletal muscle of these mice. Consistent with increased whole-body insulin sensitivity, gAcrp30 treated mice manifested 2 to 4-fold increases in insulin-mediated insulin receptor tyrosine autophosphorylation (tyrosine 1162) in both liver and skeletal muscle **(Fig. 3*A* and 3*B*)**. We also observed four-fold increases in insulin-stimulated insulin receptor substrate-2 (IRS-2) associated phosphoinositide 3-kinase (PI3K) activity in liver and IRS-1 associated PI3K activity in muscle, as well as two-fold increases in Akt2 phosphorylation in liver and skeletal muscle of gAcrp30 treated mice as compared with vehicle-treated mice in the clamp state **(Fig. 3*C*-3*F*)**, indicating improved insulin signaling in liver and muscle. Activated c-Jun N-terminal kinase (JNK) can phosphorylate insulin receptor substrate-1 (IRS-1) serine 302, resulting in negative regulation of the insulin signaling pathway in mouse tissues (23, 215). This mechanism may play a role in the improved insulin sensitivity seen in gAcrp30 treated mice, as we observed an ~40% decrease in JNK phosphorylation in liver and muscle from animals treated with gAcrp30 vs. vehicle-treated animals **(Fig. 3*G* and 3*H*)**, which may in part be due to adiponectin's effect on reducing oxidative stress (23).

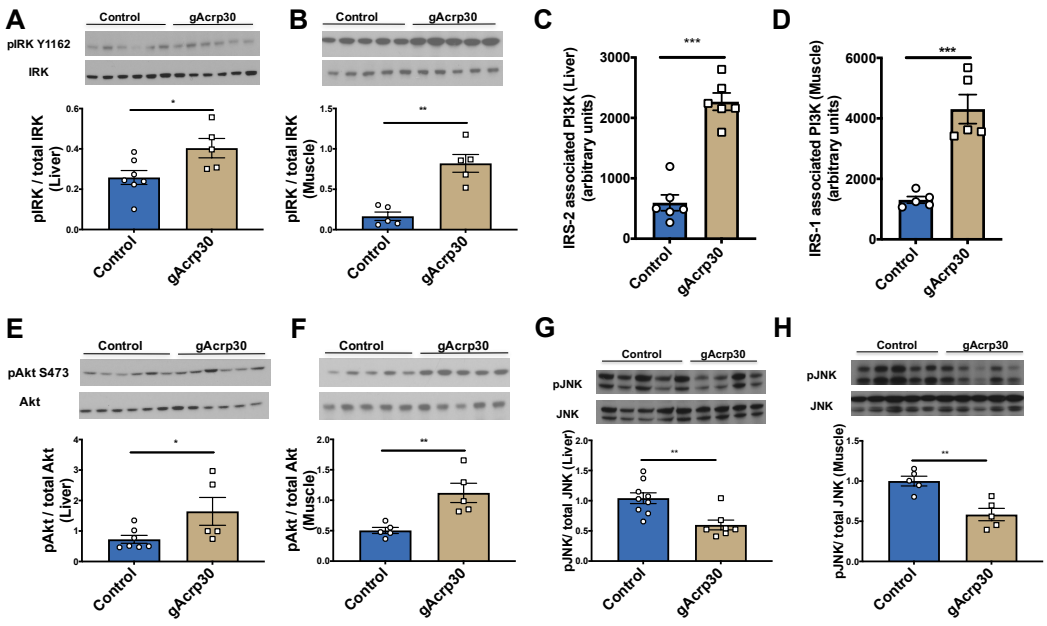

Figure 3. Globular adiponectin increases insulin signaling at the level of insulin receptor kinase in liver and skeletal muscle. (*A*)-(*B*) Western blot images for insulin receptor kinase phosphorylation (pY1162) in liver (*n* = 5-7) and skeletal muscle (*n* = 5) of control and gAcrp30-treated mice under the hyperinsulinemic-euglycemic clamp condition. Quantification is shown below. (*C*) IRS-2 associated PI3K activity in liver. (*D*) IRS-1 associated PI3K activity in muscle (*n* = 5). (*E*)-(*F*) Western blot images for Akt phosphorylation (pS473) in liver (*n* = 5-7) and skeletal muscle (*n* = 5) in the clamp state. Quantification is shown below. (*G*) Representative western blot images for JNK phosphorylation in liver of control and gAcrp30-treated mice in the clamp state. Quantification is shown below. (*H*) Western blot images for JNK phosphorylation skeletal muscle (*n* = 5) in the clamp state. Quantification is shown below. Data are shown as mean ± SEM. *p < 0.05, **p < 0.01, ***p < 0.001 by unpaired Student's t-test.

DAGs and ceramides are two well-studied bioactive lipids that have been proposed to mediate lipid-induced insulin resistance (66). Plasma membrane DAGs have been shown to mediate insulin resistance by activation of nPKCs, specifically PKCε in the liver and both PKCε and PKCθ in the skeletal muscle (17, 19, 216, 217). Among the three stereoisomers of DAG (*sn*-1,2-DAG, *sn*-1,3-DAG and *sn*-2,3-DAG), *sn*-1,2-DAG is thought to be primarily responsible for nPKC activation (218-220). To understand the mechanism by which gAcrp30 treatment ameliorates lipid-induced liver and muscle insulin resistance, DAG content, ceramide content and nPKC translocation were measured in these tissues. Hepatic plasma membrane *sn*-1,2-DAG was decreased by 35% in gAcrp30-treated mice, which was associated with an ~50% reduction in PKCε membrane translocation, reflecting reduced PKCε activation **(Fig. 4*A* and 4*B*)**. Plasma membrane *sn*-2,3-DAG content was decreased by 35% without any difference in sn-1,3-DAG content and *sn*-1,2-DAG content in other subcellular compartments **(Fig. 4*A*, 4*C* and 4*D*)**. INSR Thr1160 is a PKCε target, upon which phosphorylation impairs the tyrosine kinase activity of the insulin receptor, and thereby diminishes downstream insulin signaling (17, 219). Consistent with reductions in PKCe activity and improved hepatic insulin sensitivity, hepatic insulin receptor Thr1160 phosphorylation was decreased in gAcrp30-treated mice **(Fig. 4*E*)**. Similarly, in the gastrocnemius muscle, gAcrp30-treated mice exhibited a ~55% reduction in plasma membrane DAG content with an associated 60-80% reduction in PKCθ and PKCε translocation **(Fig. 4*F*-4*H*)**. In contrast, despite the reductions in liver and muscle TAG content, plasma membrane DAG content and marked reversal of insulin resistance in liver and skeletal muscle, there were no significant changes in total ceramide content in these tissues **(Fig. 5*A* and 5*B*)**, arguing against an important role for adiponectin-induced activation of ceramidase as the insulin sensitizing mechanism by which adiponectin would have been expected to lead to a reduction in total ceramide content (114). In addition, we did not observe any significant differences in the total content of specific ceramide species

(C16:0 and C18:0) which have been specifically hypothesized to mediate insulin resistance in rodents (78, 221) **(Fig. 5*C*-5*F*)**. While gAcrp30 treatment did not cause a reduction in total tissue ceramide content, it did result in reductions in several hepatic ceramide species (C16:0, C20:0, C22:0, C24:0 and C24:1) in the plasma membrane **(Fig. 5*G*)**, which correlated with the improved insulin sensitivity in liver.

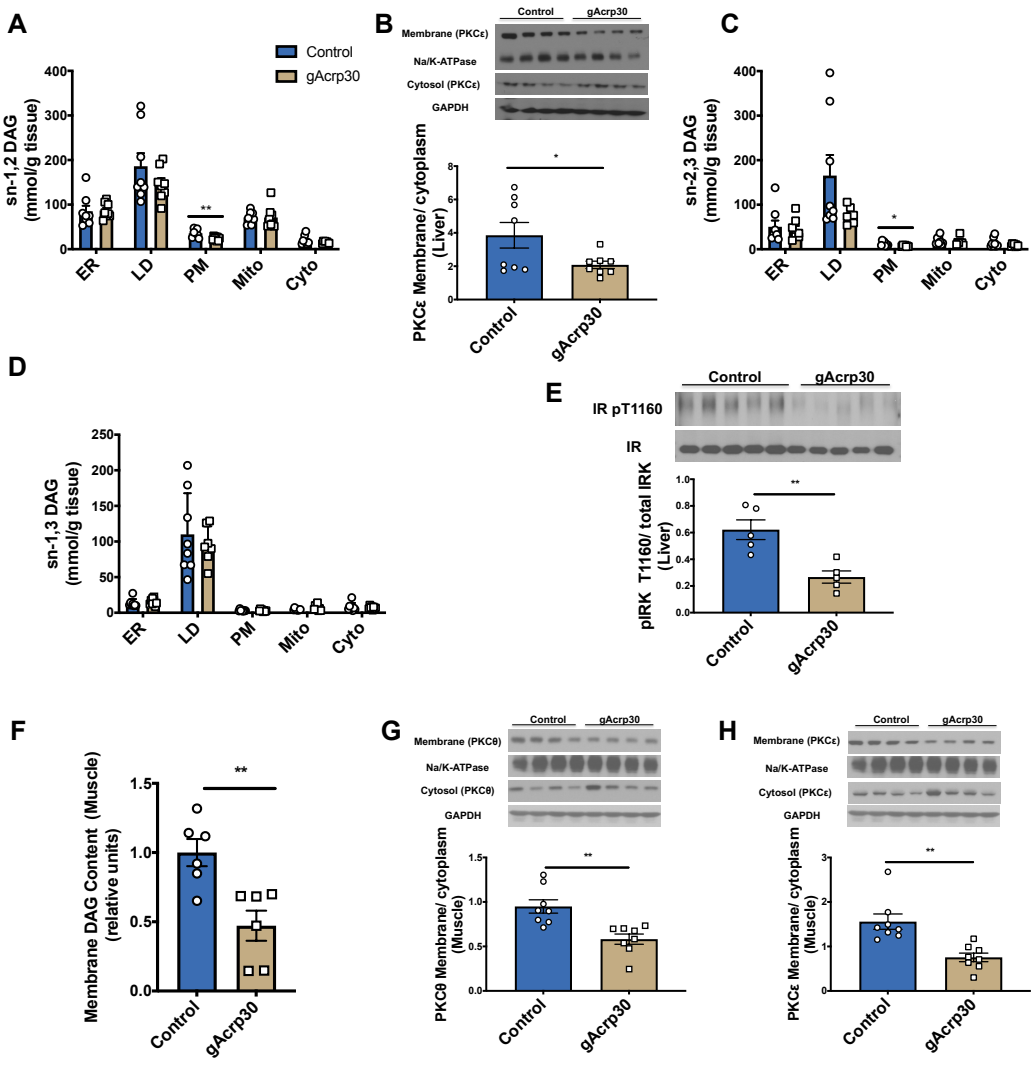

Figure 4. Globular adiponectin reduces tissue membrane DAG content and nPKC activation in liver and muscle. (*A*) Hepatic *sn*-1,2-DAG content in five subcellular compartments (ER: endoplasmic reticulum; LD: lipid droplets; PM: plasma membrane; Mito: mitochondrial; Cyto: cytosol). (*B*) Hepatic membrane/cytosolic PKCε ratio. Quantification is shown below. (*C*) Hepatic *sn*-2,3-DAG in five subcellular compartments. (*D*) Hepatic *sn*-1,3-DAG in five subcellular compartments. (*E*) Western blot images for insulin receptor kinase phosphorylation (pY1160) in liver (n = 5). Quantification is shown below. (*F*) Membrane DAG content in skeletal muscle. (*G*)-(*H*) Membrane/cytosolic PKCθ and PKCε ratio in skeletal muscle. PKCθ and PKCε were probed from the same

membrane and therefore have the same corresponding loading controls (GAPDH and Na/K-ATPase). Quantification is shown below. Data are shown as mean ± SEM. *p < 0.05, **p < 0.01 by two-way ANOVA with Dunnett multiple comparisons for (*A*), (*C*) and (*D*). *p < 0.05, **p < 0.01 by unpaired Student's t-test.

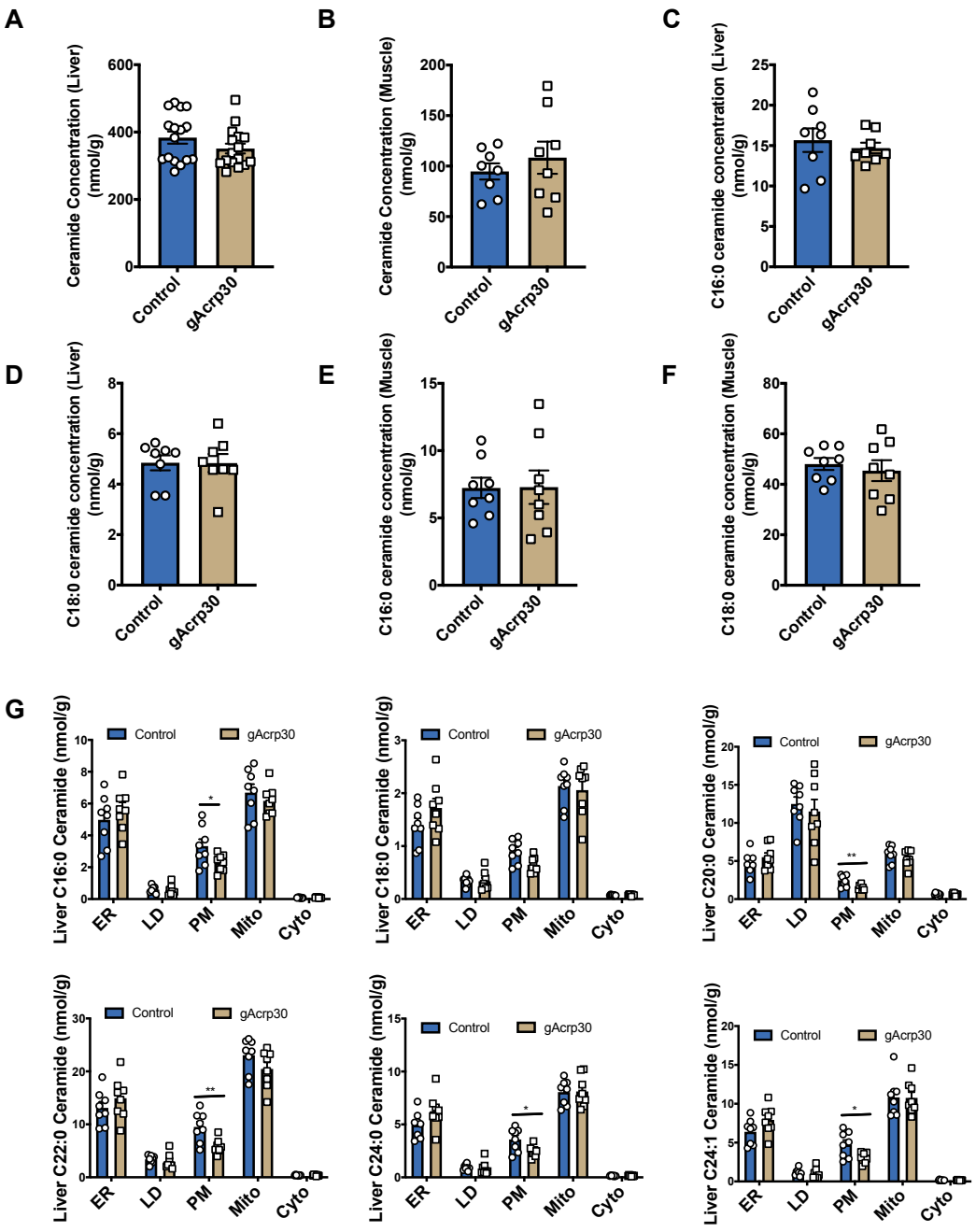

Figure 5. Globular adiponectin did not significantly affect total ceramide content but changes several plasma membrane ceramide species. (*A*)-(*B*) Total ceramide content in liver (*n* = 16) and skeletal muscle. (*C*)-(*F*) C16:0 and C18:0 ceramide concentrations in liver and skeletal muscle. (*G*) Six different hepatic ceramide species in five subcellular compartments (ER: endoplasmic reticulum; LD: lipid droplets; PM: plasma membrane;

Mito: mitochondrial; Cyto: cytosol). Data are shown as mean ± SEM. *$p < 0.05$, **$p < 0.01$ by unpaired Student's t-test for other panels.

gAcrp30 improves insulin signaling in white adipose tissue

Next, we sought to understand the effect of gAcrp30 treatment on insulin signaling in WAT and on WAT lipolysis. gAcrp30 administration increased phosphorylation of IRK and Akt2, and reduced phosphorylation of perilipin, adipose triglyceride lipase (ATGL) and hormone-sensitive lipase (HSL) in the clamp state, indicating improved insulin signaling in WAT **(Fig. 6*A*-6*E*)**. Consistent with these data, gAcrp30-treated mice had reduced whole-body glycerol turnover rate in the basal and clamp state, demonstrating that gAcrp30 treatment reduced WAT lipolysis and improved insulin signaling in WAT **(Fig. 6*F*)**. Reduced glycerol conversion to glucose may result in reduced hepatic glucose production and plasma glucose concentrations (222). However, surprisingly there were no differences in the whole-body fatty acid turnover rate or plasma non-esterified fatty acids (NEFA) concentrations **(Fig. 6*G* and 2*F*)**, suggesting that gAcrp30 may also promote WAT re-esterification. Consistent with the lack of differences in fatty acid turnover, we observed no differences in hepatic acetyl-CoA, malonyl-CoA, or long-chain acyl-CoA concentrations **(Fig. 6*H*-6*G*)**. Taken together, these data indicate that gAcrp30 treatment also improves insulin signaling in WAT and may affect WAT lipolysis and re-esterification.

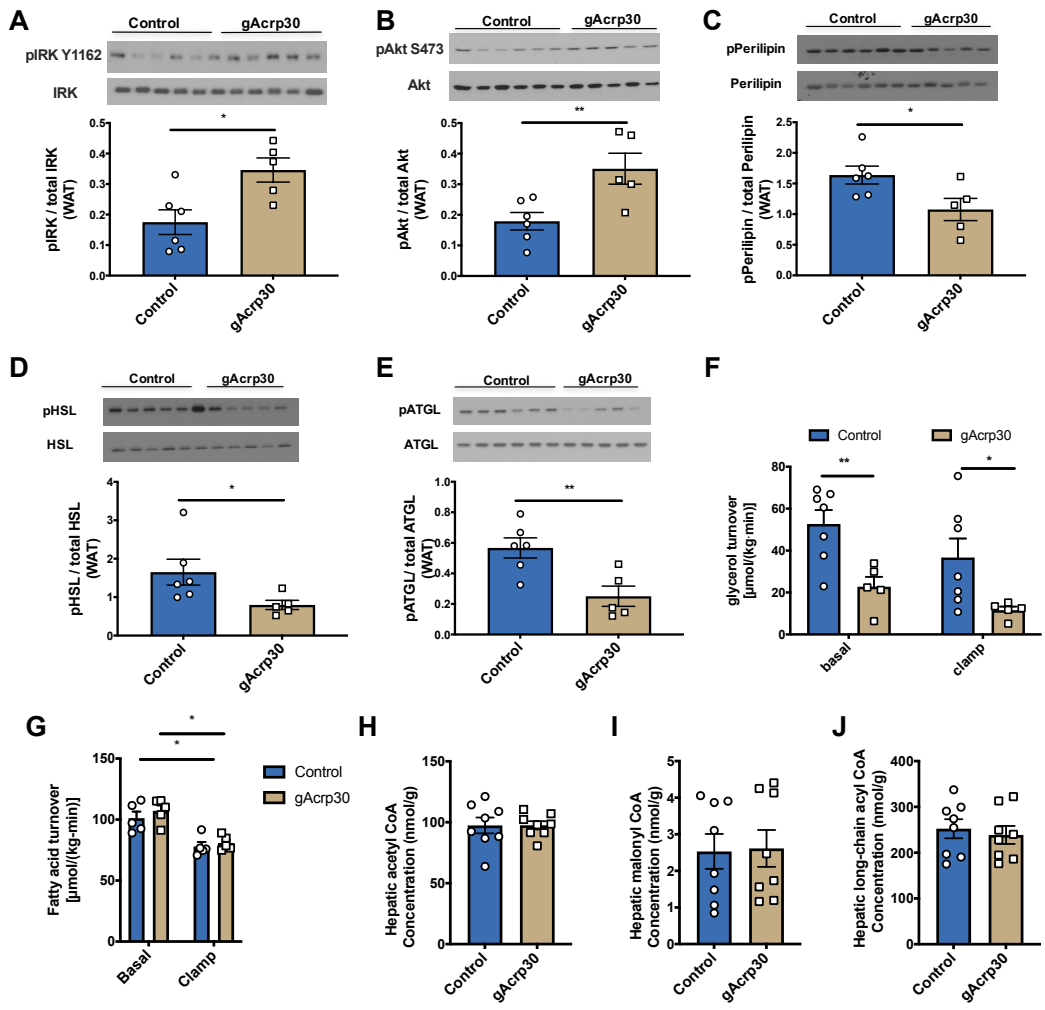

Figure 6. gAcrp30 improves insulin signaling in white adipose tissue and may affect WAT lipolysis and re-esterification. (*A*) Western blot images for insulin receptor kinase phosphorylation (pY1162) in white adipose tissue (*n* = 5-6) in the clamp state. Quantification is shown below. (*B*) Western blot images for Akt phosphorylation (pS473) in white adipose tissue (*n* = 5-6) in the clamp state. Quantification is shown below. (*C*)-(*E*) Western blot images for perilipin, hormone-sensitive lipase (HSL) and adipose triglyceride lipase (ATGL) phosphorylation in white adipose tissue (*n* = 5-6) in the clamp state. Quantification is shown below. (*F*) Glycerol turnover rate under basal and hyperinsulinemic-euglycemic conditions (*n* = 5-7). (*G*) Fatty acid turnover rate under basal and hyperinsulinemic-euglycemic conditions (*n* = 5). (*H*)-(*J*) Basal hepatic acetyl CoA,

Malonyl CoA and Long-chain acyl CoA concentrations. Data are shown as mean ± SEM. *p < 0.05, **p < 0.01 by two-way ANOVA with Dunnett multiple comparisons for (*F*) and (*G*). *p < 0.05, **p < 0.01 by unpaired Student's t-test for other panels.

Globular adiponectin treatment promotes a switch from glucose to fat oxidation in slow-twitch gastrocnemius and soleus muscles

In order to determine whether the reduction in ectopic lipid (TAG/DAG) content could be attributed to increased fatty acid oxidation in liver and muscle, we assessed mitochondrial function *in vivo* and *ex vivo*. We employed positional isotopomer NMR tracer analysis (PINTA) to assess the effects of gArcp30 on *in vivo* hepatic citrate synthase flux (V_{CS}, i.e. mitochondrial oxidation) and hepatic pyruvate carboxylase flux (V_{PC}, i.e. gluconeogenesis from pyruvate) (223) and observed no significant differences in hepatic V_{PC} or V_{CS} in gAcrp30 treated mice **(Fig. 7*A* and 7*B*)**. In addition, there was no difference in the phosphorylation of two key regulators of hepatic fatty acid oxidation and biosynthesis: AMPK and ACC with gAcrp30 treatment **(Fig. 7*C* and 7*D*)**. In summary, no differences were observed in hepatic mitochondrial oxidation rate or its upstream regulators or downstream outflow (V_{PC}) in the gAcrp30 treated mice.

Relative rates of mitochondrial ketone oxidation and β-oxidation (V_{FAO}) normalized to citrate synthase flux (V_{CS}) were determined *in vivo* in multiple tissues. gAcrp30 treatment promoted a shift away from glucose to other substrates (fatty acids, ketones, ketogenic amino acids) in gastrocnemius muscle **(Fig. 7*E*)**, despite no effect on liver or quadriceps muscles **(Fig. 7*F* and 7*G*)**. To further examine the effects of gAcrp30 on absolute rates of fatty acid oxidation and glucose oxidation in muscle, we assessed rates of $^{14}CO_2$ production in isolated soleus muscle with [1-^{14}C]palmitic acid and [$^{14}C_6$]D-glucose as substrates. Consistent with the *in vivo* gastrocnemius data, both fatty acid oxidation and glucose oxidation were increased in the Acrp30-treated and gAcrp30-treated soleus muscles **(Fig. 7*H* and 7*I*)**. To understand the potential molecular mechanisms by which fatty acid oxidation was increased in the soleus muscle, we measured phosphorylation of AMPK, ACC and endothelial nitric oxide synthase (eNOS). Previous studies have shown that there is a positive feedback loop between nitric oxide production and AMPK activation

(224). Consistent with these studies, we observed significant increases in phosphorylation of AMPK, ACC and eNOS in the skeletal muscle of both Acrp30-treated and gAcrp30-treated mice **(Fig. 7*J*-7*L*)**. These data suggest that gAcrp30 and Acrp30 treatment activates the eNOS/AMPK/ACC pathway and promotes a switch from glucose oxidation to fatty acid oxidation in predominately slow-twitch gastrocnemius and soleus muscles but does not impact hepatic mitochondrial fat oxidation.

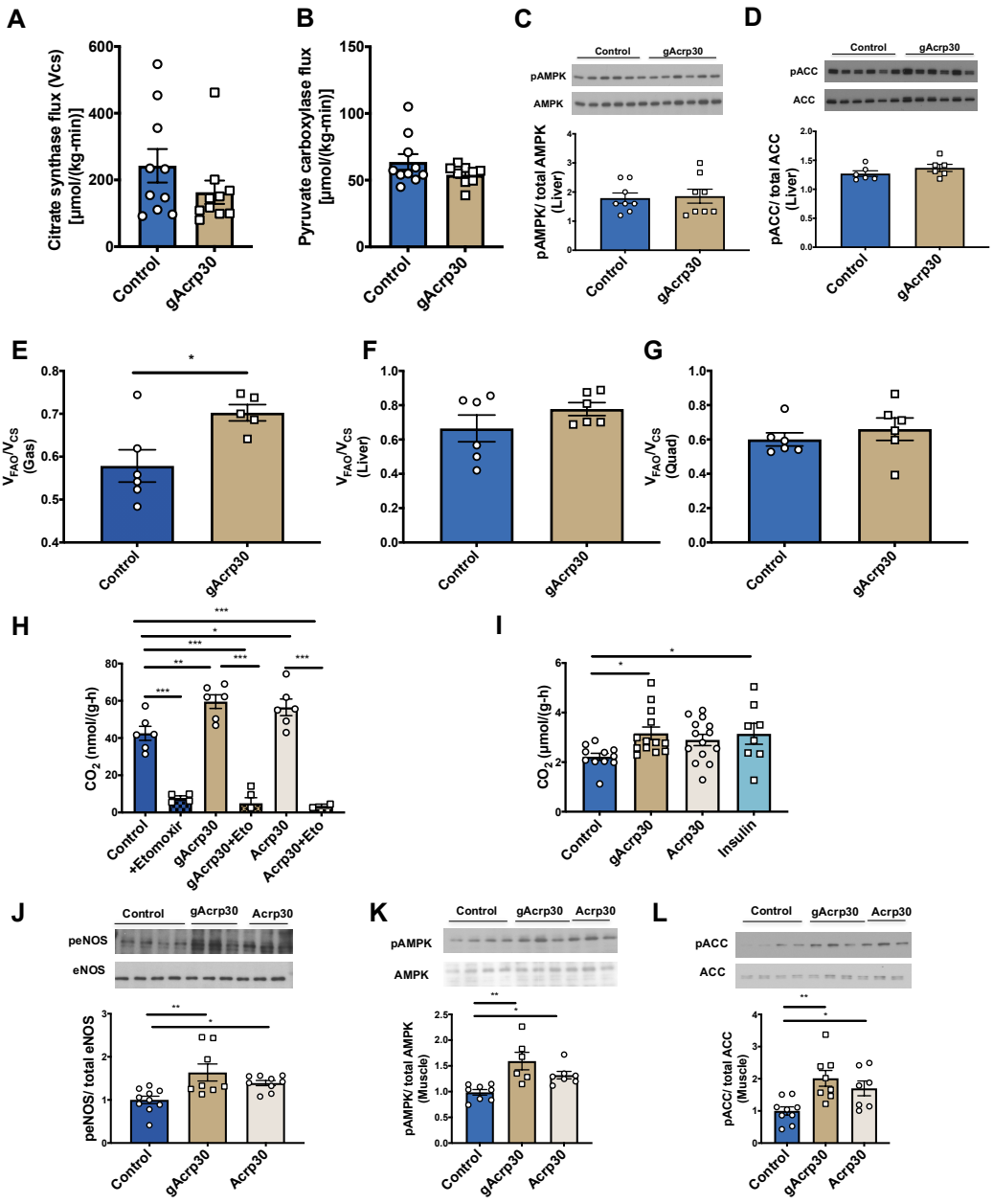

Figure 7. gAcrp30 increases the switch from glucose to fat oxidation in skeletal muscle *in vivo*. (*A*) Hepatic citrate synthase flux rate in control and gAcrp30-treated mice (*n* = 10). (*B*) Hepatic pyruvate carboxylase flux rate (*n* = 10). (*C*)-(*D*) Western blot images for basal 5' AMP-activated protein kinase (AMPK) and acetyl-CoA carboxylase (ACC) phosphorylation in liver. Quantification is shown below. (*E*)-(*G*) Ratio of mitochondrial ketone oxidation and β-oxidation (V_{FAO}) to citrate synthase flux (V_{CS}) in soleus muscle (*n*

= 5-6), liver and quadriceps femoris muscle. (*H*) Fatty acid oxidation rates of solus muscles with no treatment (control), control + etomoxir, gAcrp30 treatment, gAcrp30 + etomoxir, Acrp30 treatment, Acrp30 + etomoxir (*n* = 2-6). (*I*) Glucose oxidation rates of soleus muscles with no treatment (control), gAcrp30 treatment, Acrp30 treatment and insulin treatment (*n* = 8-14). (*J*)-(*L*) Representative western blot images for non-treated, gAcrp30-treated and Acrp30-treated AMPK, ACC and endothelial nitric-oxide synthase phosphorylation in soleus muscle. Quantification is shown below. Data are shown as mean ± SEM. *p<0.05, **p<0.01, ***p<0.001 by one-way ANOVA with Tukey multiple comparisons for (*H*)-(*L*). *p<0.05 by unpaired Student's t-test for other panels.

Globular adiponectin and full-length adiponectin increase lipoprotein lipase activity and lipid uptake in epididymal white adipose tissue

To determine whether adiponectin treatment alters ectopic lipid deposition by changing triglyceride rich lipoprotein metabolism, we performed a series of studies assessing very-low-density lipoprotein (VLDL) production and chylomicron clearance. We first measured the rates of hepatic VLDL-TAG production to evaluate whether hepatic VLDL-TAG production contributed to the reduced plasma TAG in the gAcrp30-treated mice. No significant difference in the hepatic VLDL-TAG production rate with gAcrp30 treatment was observed **(Fig. 8*A* and 8*B*)**. Then we tested the hypothesis that the reductions in TAGs and membrane DAGs in liver and skeletal muscle may be explained by increased uptake of lipids into WAT, thereby diverting circulating triglycerides away from storage in liver and skeletal muscle. Consistent with the hypothesis, plasma lipid clearance was increased during an oral lipid tolerance test in the gAcrp30-treated mice **(Fig. 8*C* and 8*D*)**. gAcrp30 treatment promoted increased lipid uptake in epididymal adipose tissue (eWAT) despite no significant difference in lipid uptake in subcutaneous WAT (sWAT) or skeletal muscle **(Fig. 8*E*-8*G*)**.

Lipoprotein lipase (LPL) plays an important role in the clearance of plasma TAG and the import of TAG-derived fatty acid to muscle and heart for utilization and adipose tissues for storage (225). We measured plasma and tissue-specific LPL activity to assess whether gAcrp30 alters adipose chylomicron clearance via alterations in LPL activity. gAcrp30 treated mice have increased heparin-releasable LPL activity in plasma and increased LPL activity in eWAT and heart **(Fig. 8*H*-8*J*)**. In contrast, there were no significant effects of gAcrp30 treatment on sWAT, brown adipose tissue (BAT) or skeletal muscle LPL activity **(Fig. 8*K*-8*M*)**.

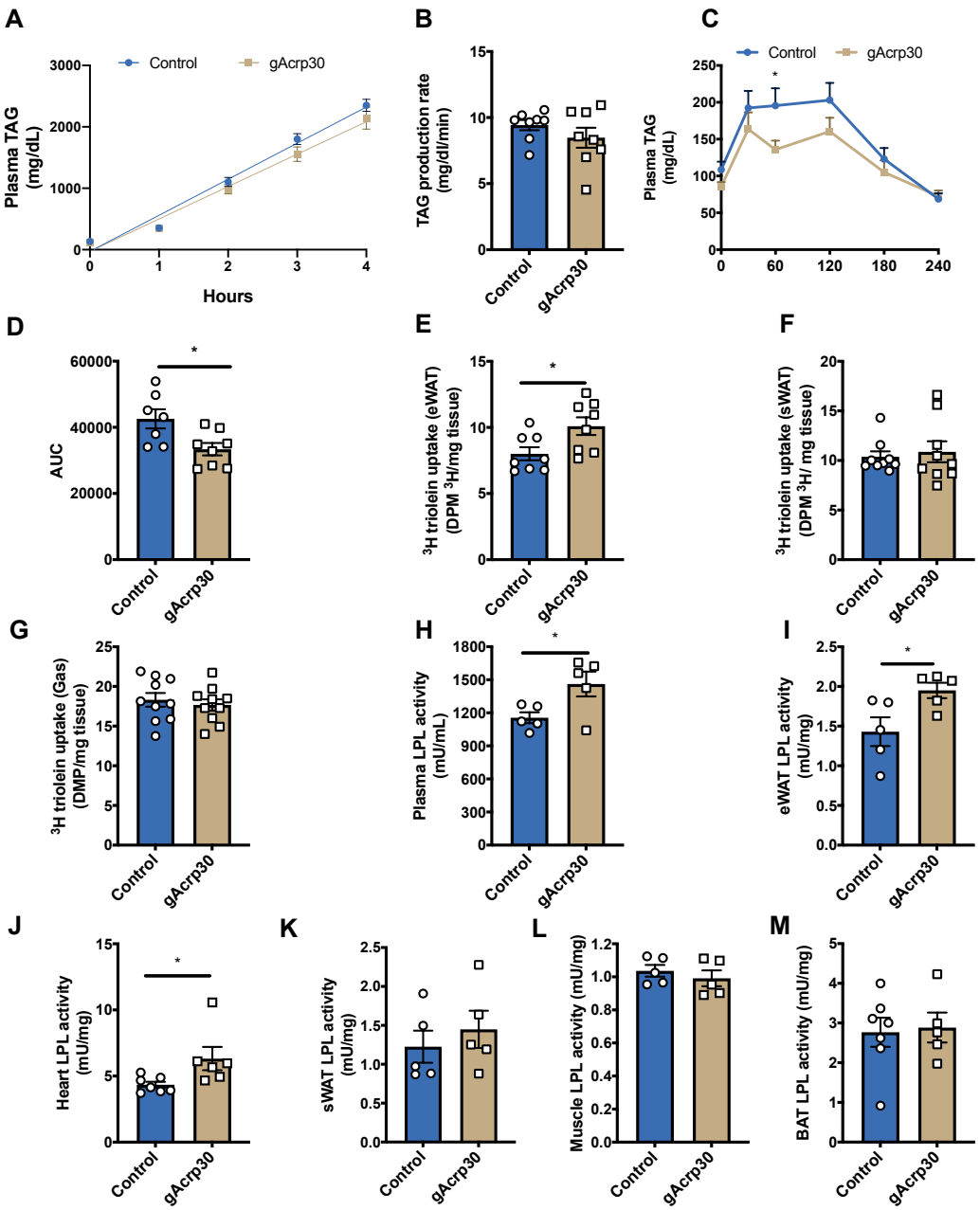

Figure 8. Globular adiponectin increases lipoprotein lipase activity and lipid uptake in epididymal white adipose tissue. (*A*) Plasma triglyceride levels in overnight-fasted control and gAcrp30 treated mice after an intraperitoneal injection of poloxamer. (*B*) Liver triglyceride production rate in control and gAcrp30 treated mice. (*C*) Plasma triglyceride concentrations of control and gAcrp30-treated mice during oral lipid tolerance test. (*D*) Area under the plasma triglycerides curve of control and gAcrp30-treated mice. (*E*)-(*G*)

Triglyceride uptake in epididymal white adipose tissue (*n* = 8-10), subcutaneous white adipose tissue and skeletal muscle (*n* = 10) of control and gAcrp30-treated mice. (*H*) Post-heparin plasma LPL activity of control and gAcrp30-treated mice (*n* = 5). (*I*) Epididymal white adipose tissue LPL activity of control and gAcrp30-treated mice (*n* = 5). (*J*) Heart LPL activity of control and gAcrp30-treated mice. (*K*) Subcutaneous white adipose LPL activity of control and gAcrp30-treated mice (*n* = 5). (*L*) Brown adipose tissue LPL activity of control and gAcrp30-treated mice (*n* = 5-7). (*M*) Skeletal muscle LPL activity of control and gAcrp30-treated mice (*n* = 5). Data are shown as mean ± SEM. *$p < 0.05$ by unpaired Student's t-test.

It has previously been shown that Acrp30 also reduces plasma and tissue TAG content in mice liver and skeletal muscle (112, 226). To determine whether the decreased TAG content by Acrp30 could be explained by similar mechanisms as gAcrp30 treatment, we performed continuous subcutaneous Acrp30 infusions (10μg/day) in HFD-fed mice for two weeks and a series of studies assessing chylomicron clearance and LPL activity. As expected, plasma TAG was decreased with Acrp30 treatment **(Fig. 9*A*)**. Analogous to what we observed in gAcrp30 treated mice, two-week Acrp30 treatment increased lipid clearance during the oral lipid tolerance test and improved lipid uptake in eWAT, without significant difference in lipid uptake in sWAT or skeletal muscle **(Fig. 9*A*-9*E*)**. Acrp30 infusion also increased heparin-releasable plasma LPL activity and increased LPL activity in eWAT and BAT **(Fig. 9*F*-9*H*)**. No significant differences in sWAT, heart and muscle were observed **(Fig. 9*I*-9*K*)**. Taken together, these data demonstrate that both full-length and globular adiponectin treatment enhances lipid uptake in eWAT, which may be attributed to localized stimulation of LPL activity in eWAT.

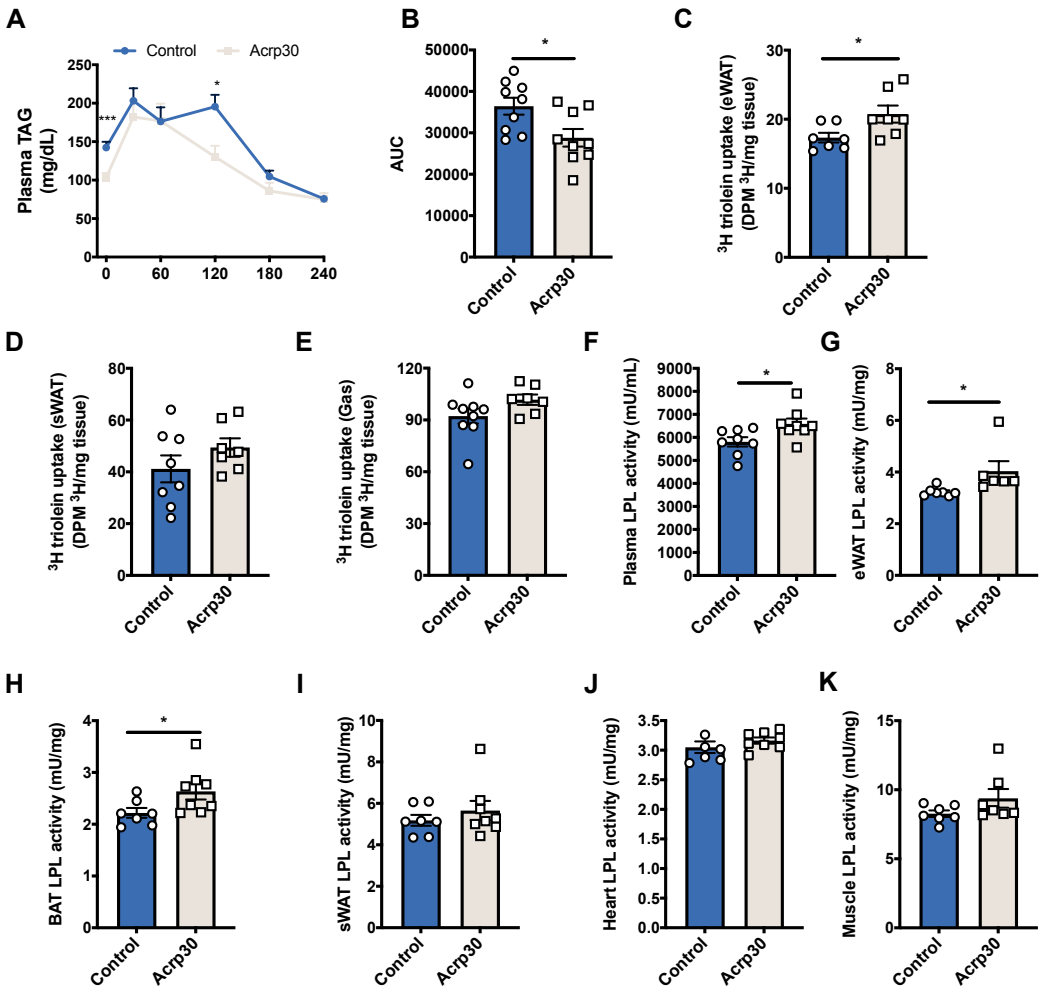

Figure 9. Globular adiponectin and full-length adiponectin increase lipoprotein lipase activity and lipid uptake in epididymal white adipose tissue. (*A*) Plasma triglyceride concentrations of control and Acrp30-treated mice during oral lipid tolerance test. (*B*) Area under the plasma triglycerides curve of control and Acrp30-treated mice. (*C*)-(*E*) Triglyceride uptake in epididymal white adipose tissue, subcutaneous white adipose tissue and skeletal muscle of control and Acrp30-treated mice. (*F*) Post-heparin plasma LPL activity of control and Acrp30-treated mice. (*G*) Epididymal white adipose tissue LPL activity of control and Acrp30-treated mice. (*H*) Brown adipose tissue LPL activity of control and Acrp30-treated mice. (*I*) Subcutaneous white adipose LPL activity of control and Acrp30-treated mice. (*J*) Heart LPL activity of control and Acrp30-treated

mice. (*K*) Skeletal muscle LPL activity of control and Acrp30-treated mice. Data are shown as mean ± SEM. *p < 0.05, ***p<0.001 by unpaired Student's t-test.

DISCUSSION

White adipose tissue is not only a critical energy storage depot, but it also acts as an endocrine organ sensing metabolic signals and secreting hormones and adipocytokines (e.g. leptin and adiponectin) that regulate whole-body energy homeostasis (196, 227-229). Consistent with previous reports (111, 115, 208), we have demonstrated that administration of globular adiponectin results in an improvement in whole-body glucose homeostasis. Despite great interest in adiponectin, the mechanism by which adiponectin reverses insulin resistance had remained unclear. To address this question, we performed a comprehensive series of studies including hyperinsulinemic-euglycemic clamp studies combined with stable- and radio-labeled isotopic tracers to characterize adiponectin's effects on endogenous glucose production and tissue-specific insulin sensitivity and followed these studies up by measuring bioactive lipid metabolites and cellular insulin signaling phosphorylation events in liver, skeletal muscle and WAT.

Adiponectin receptor associated ceramidase activity, promoting decreased total hepatic ceramide content and ceramide-induced insulin resistance, has been proposed to mediate adiponectin's insulin-sensitizing properties (114). However, in contrast to this hypothesis, we dissociated changes in total ceramide content in the liver and skeletal muscle from gAcrp30-induced improvements in liver and muscle insulin sensitivity. The results are different possibly because 1) the mouse models we used are different. Scherer's group used *ob/ob* mice and transgenic mice, but we used HFD-fed WT mice; 2) the treatment and dose of adiponectin are different. They performed an acute (60-min) intravenous injection of full-length adiponectin and the dose they used (2 μg/g) is unphysiological large dose, while we did a relatively long-term (2-week) subcutaneous administration of both full-length or globular adiponectin, and the doses (Acrp30: 10 μg/day and gAcrp30: 2.5 μg/day) we used are more physiological relevant dose. The chronic treatment may be more relevant for human therapy. We also did not observe any

significant differences in the content of specific ceramide species (C16:0 and C18:0) which have been specifically hypothesized to mediate insulin resistance in rodents (78, 221). While gAcrp30 treatment did not cause a reduction in total tissue ceramide content or in changes in C16:0 or C18:0 ceramides, it did result in reductions in several hepatic ceramide species (C16:0, C20:0, C22:0, C24:0 and C24:1) in the plasma membrane which correlated with improved insulin sensitivity in liver. Whether these specific plasma-membrane associated ceramide species also contributed to alterations in insulin action will need to be examined in future studies.

Nevertheless, ceramide-induced insulin resistance is thought to alter downstream insulin signaling at the level of Akt; however we observed that gAcrp30 improved insulin action at the level of the insulin receptor, which is not compatible with the putative mechanisms by which adiponectin is thought to mediate insulin resistance at the level of AKT2 phosphorylation.

In contrast with ceramide-induced insulin resistance, DAG-PKCe induced insulin resistance can explain improved insulin signaling at the level of the insulin receptor. By this mechanism, *sn*-1,2-DAG accumulation in the plasma membrane of liver and muscle results in nPKC translocation from the cytoplasm to the plasma membrane, leading to decreased insulin signaling at the level of the insulin receptor due to PKCe activation and at the level of IRS-1 and IRS-2 associated PI3-kinase due to PKCq activation (17-19). We observed that 2 weeks of gAcrp30 treatment reduced plasma membrane *sn*-1,2-DAG in liver and membrane associated DAG in muscle, leading to decreased PKCε activity in liver and both PKCθ and PKCε activity in skeletal muscle. As a result, insulin signaling at the level of insulin receptor kinase increased in both of these tissues. As such, the effect of globular adiponectin on tissue-specific insulin action appears to occur through reductions in liver and muscle plasma membrane DAG content resulting in reduced PKCe activation in liver and reduction in both PKCe and PKCq activation in skeletal muscle.

In both *in vitro* and *ex vivo* studies, adiponectin has been suggested to reduce triglyceride content in the liver and muscle by enhancing fatty acid oxidation in an AMPK dependent manner (23, 115, 117, 118, 230). However, Yamauchi et al. found that globular adiponectin cannot activate hepatic AMPK signaling pathways (112). No competing hypothesis has yet been published, and so the underlying physiological mechanisms by which gAcrp30 reduces hepatic TAG are still debated. Further complicating this question, most mechanistic studies examining adiponectin's mechanism of action have been performed purely *in vitro* and *ex vivo*, although *in vivo* studies are critical to understand the complex inter-organ crosstalk that regulates metabolic physiology. Reduced ectopic lipid content in liver and skeletal muscle may be due to several factors including: 1) decreased NEFA flux to these tissues from reduced WAT lipolysis; 2) increased rates of tissue mitochondrial fatty acid oxidation; and 3) decreased lipid delivered to tissues from circulating lipoproteins. We evaluated each of these potential mechanisms for the gAcrp30-induced reductions in ectopic lipids in HFD-fed mice using a comprehensive series of *in vivo* metabolic studies. While gAcrp30 appeared to suppress rates of WAT lipolysis, as reflected by reduced rates of glycerol turnover and increased WAT insulin sensitivity, as reflected by increased insulin-stimulated glucose uptake, it did not affect whole-body fatty acid turnover potentially due to compensatory changes in re-esterification. Additionally, hepatic mitochondrial fatty acid oxidation and the regulation of fat oxidation in liver were unchanged. In gastrocnemius and soleus muscle, gAcrp30 treatment increases muscle fatty oxidation *in vivo* and *ex vivo*, an effect that was correlated with increased phosphorylation of ACC in a manner consistent with previously described eNOS/AMPK-dependent regulation of ACC (224). This increase in skeletal muscle fatty acid oxidation could account, in part, for the reduced ectopic lipid deposition seen in several tissues in gAcrp30 treated mice, and the improvement in muscle insulin sensitivity.

In addition to promoting increased muscle fatty acid oxidation, we also found that both gAcrp30 and Acrp30 treatment reduces ectopic lipid (TAG/plasma membrane DAG) accumulation in liver and skeletal muscle by improving WAT triglyceride uptake and further increasing WAT storage capacity. Adiponectin-treated mice displayed increased LPL activity in post-heparin plasma and eWAT, and improved adipose postprandial triacylglycerol uptake. These results are consistent with our observations that two weeks of gAcrp30 or Acrp30 treatment increased eWAT mass but did not change total fat mass, as assessed by ^{1}H NMR.

Our findings also imply an important role for decreased plasma adiponectin in the development of lipid-induced liver and skeletal muscle insulin resistance. In humans and monkeys, plasma adiponectin levels correlate significantly with whole-body insulin sensitivity (25, 26). Overexpression or administration of adiponectin in mice results in a decrease in hyperglycemia and improvement in systemic insulin sensitivity (23, 27), whereas adiponectin-deficient mice exhibit impaired insulin sensitivity and are prone to diabetes (24, 28). Tying all of this together, circulating adiponectin may be a reflection of the presence of functioning adipose tissue, a part of the machinery the WAT uses in its fat-storing operation. In normal physiology, healthy adipose tissue secretes sufficient adiponectin to promote storage of circulating triglyceride in WAT, and signal a shift to increase fatty acid oxidation in skeletal muscle. However, in obesity, as adipose tissue has limited storage capacity, WAT secretion of adiponectin decreases. This derangement in fat storage and muscle fat oxidation may then lead to increased ectopic lipid (TAGs/ plasma membrane DAGs) accumulation in liver and skeletal muscle and the subsequent development of insulin resistance in these organs leading to the metabolic syndrome, hepatic steatosis/NASH, and atherosclerosis.

Taken together, these results suggest that chronic adiponectin administration ameliorates insulin resistance in an HFD-fed mouse model of obesity, NAFLD and insulin

resistance by two major mechanisms. First, adiponectin treatment promotes increased WAT LPL activity, which may lead to increased uptake of triglyceride into WAT thus diverting circulating triglyceride away from storage in liver and skeletal muscle. Second, adiponectin treatment promotes increased fatty acid oxidation in skeletal muscle, which in turn may be attributed to the activation of AMPK and eNOS. These two effects of adiponectin in turn lead to reductions in liver and muscle membrane associated *sn*-1,2-DAG content, resulting in decreased PKCε activity in liver and decreased PKCε and PKCθ in muscle resulting in increased insulin signaling and insulin action in these tissues. Furthermore adiponectin-induced improvement in liver and muscle insulin sensitivity in insulin resistant HFD-fed mice occurred independently of changes in total ceramide content in these tissues. Taken together, these studies provide new insights into the mechanisms by which adiponectin reverses HFD-induced liver and muscle insulin resistance in mice.

METHODS

Animals and diets

All rodent studies were approved by the Yale University Institutional Animal Care and Use Committee. Male C57BL/6J mice (Jackson Laboratory) were group housed at the animal care facility at Yale University Animal Research Center and maintained under controlled temperature (23°C) and lighting (12:12 h light/dark cycle, lights on at 7:00 AM) with free access to water and food. Diet-induced obesity studies were carried out by feeding mice a high fat diet (60% calories from fat, Research Diets D12492). To study the effects of adiponectin treatment, following 2 weeks or 10 weeks of HFD, mini-osmotic pumps (Alzet) containing recombinant mouse globular adiponectin protein (Abcam), recombinant mouse full-length adiponectin (Abcam) or vehicle (saline) were implanted subcutaneously. Adiponectin was released at a rate of 2.5 μg/day (globular adiponectin) or 10 μg/day (full-length adiponectin) for 14 days based on previous literature (112, 115). Food and water intake measurements and indirect calorimetry were performed using Columbus Lab Animal Monitoring System metabolic cages (Columbus Instruments). During this time, food intake and body weight were regularly monitored. The mice used for euglycemic clamp and *in vivo* tracer studies underwent surgery under isoflurane anesthesia to place catheters in the jugular vein and single-housed mice were allowed to recover 6-7 days before planned experiments.

Hyperinsulinemic-euglycemic clamps

Clamps were performed as previously described (9, 18). Briefly, after an overnight fast, a 120-min basal infusion with [3-^{3}H] glucose (PerkinElmer) at a rate of 0.05 μCi/min, [1,1,2,3,3-D_5] glycerol (Sigma Aldrich) at a rate of 1.5 μmol/(kg-min)and potassium [$^{13}C_{16}$] palmitate (Cambridge Isotopes) at a rate of 0.7 μmol/(kg-min) was performed. After the basal period, mice underwent a 140 min hyperinsulinemic-euglycemic clamp by infusing

[3-^{3}H] glucose, [1,1,2,3,3-D_5] glycerol and potassium [$^{13}C_{16}$] palmitate at the rates indicated above, and in the last 55 minutes of the clamp period, 2-deoxy-[1-^{14}C] glucose (2-DG) (PerkinElmer) was given to estimate tissue-specific glucose uptake. 20% dextrose (Hospira) at a variable rate and insulin at a rate of 3mU/[kg-min] was infused through the jugular venous catheter to maintain a steady state plasma glucose concentration of ~120 mg/dL. Plasma glucose concentrations were measured every 10-15 min during the hyperinsulinemic-euglycemic clamp period. At the end of the study, mice were euthanized with intravenous pentobarbital and tissues were obtained following the clamp study using freeze-clamps pre-cooled in liquid nitrogen. The specific activity of glucose was measured in plasma samples collected at the steady state during basal and clamp by liquid scintillation counting.

Flux measurement

Positional isotopomer NMR tracer analysis (PINTA) was applied to measure rates of hepatic mitochondrial citrate synthase flux (V_{CS}) and pyruvate carboxylase flux (V_{PC}) as previously described(223). Infusion of [3-^{3}H] glucose (PerkinElmer) at a rate of 0.05 μCi/min and [3-^{13}C] sodium lactate (Cambridge Isotopes) at a rate of 40 μmol/(kg-min) was performed for a total of 120 min to measure V_{PC}/V_{CS} and V_{PC}/V_{EGP} as we previously described(223).

The ratio of pyruvate dehydrogenase flux to citrate synthase flux (V_{PDH}/V_{CS}) was used to indicate tissue-specific metabolic substrate oxidation after a 2 hr infusion of [1,2,3,4,5,6-$^{13}C_6$]glucose (16.7 μmol/[kg-min] prime for 5 min, 5.6 μmol/[kg-min] continuous infusion) as previously described (231). Briefly, V_{PDH}/V_{CS} was measured as the ratio of [4,5-$^{13}C_2$]glutamate/[$^{13}C_3$]alanine. [$^{13}C_3$]alanine enrichment was measured by GC-MS and [4,5-$^{13}C_2$]glutamate enrichment was measured by liquid chromatography-tandem mass spectrometry (LC-MS/MS) as previously described (211).

[1,1,2,3,3-D_5]glycerol and [$^{13}C_{16}$]palmitate enrichments were measured using gas chromatography-mass spectrometry (GC/MS) as previously described (231). Briefly, glycerol turnover = ([1,1,2,3,3-D_5] glycerol tracer enrichment/[1,1,2,3,3-D_5] glycerol plasma enrichment-1) x infusion rate. Palmitate turnover = ([$^{13}C_{16}$] palmitate tracer enrichment/[$^{13}C_{16}$] palmitate plasma enrichment-1) x infusion rate. Fatty acid turnover = Palmitate turnover rate/ (palmitate/total fatty acids).

Palmitate and glucose oxidation measurement ex vivo

Ex vivo muscle oxidation measurements were performed as previously described (232) with minor modifications. Briefly, mice were fasted overnight (12 h) before the procedure. Animals were euthanized during tissue collection under isoflurane anesthesia; intact soleus muscles were rapidly removed and pinned in stainless steel clips to maintain resting tension. Muscles were preincubated in Krebs-Ringer bicarbonate buffer (KRBB), with 10 mM glucose and 0.5 % BSA, pH 7.4, at 35°C, for 30-45 min. Soleus muscles were then incubated in the same buffer containing either radiolabeled palmitic acid [0.1 mM palmitic acid (Sigma Aldrich) and 0.2 µCi/mL [1-^{14}C]palmitic acid (PerkinElmer)] or radiolabeled glucose [10 mM glucose (Sigma Aldrich) and 0.2 µCi/mL [$^{14}C_6$]D-glucose (PerkinElmer)] for one hour. $^{14}CO_2$ produced was trapped in NaOH (0.3 mL at 2 N) during incubation. Muscles were removed, washed in cold saline for one min, blotted on filter paper, and weighed. Incubation vials were tightly capped and 0.5 mL of 2 N HCl added directly to the KRBB using a syringe; vials were incubated for 2 h at 37°C. $^{14}CO_2$ absorbed in NaOH solution was then quantified by scintillation counting.

Biochemical analysis

Plasma glucose was measured enzymatically using a YSI Glucose Analyzer (YSI). Plasma insulin concentrations were measured by radioimmunoassay (EMD Millipore) at

the Yale Diabetes Research Center. Plasma NEFA and triglyceride concentrations were measured by standard spectrophotometric assays (NEFA: Wako Diagnostics; Triglyceride: Sekisui/Fujifilm). Plasma adiponectin (full-length and globular adiponectin) concentrations were measured by enzyme-linked immunoassay (ELISA) (Abcam).

Tissue analysis

Liver DAG stereoisomers in five subcellular compartments were measured as previously described (219, 233). Briefly, liver tissues were first homogenized with a Doucne-type homogenizer in cold (4°C) TES buffer (250 mM sucrose, 10 mM Tris - pH 7.4, 0.5 mM EDTA). Then the homogenate was centrifuged (at 12,000 rpm with SS-34 rotor or 17,000 g, 15 min, 4°C) to obtain pellet A and supernatant A. The top lipid layer was collected as the lipid droplet fraction. The supernatant A was washed, centrifuged and then resuspended in TES buffer and gently layered on top of 1.12 M sucrose buffer cushion in ultracentrifuge tubes. Then it was centrifuged (at 35,000 rpm with TLS-55 rotor or 105,000 g, 20 min, 4°C) to obtain pellet B, interface B and supernatant B. The interface B was collected, washed and centrifuged to get plasma membrane fraction. The pellet B was washed and centrifuged to obtain mitochondria fraction. The supernatant B was centrifuged (at 65,000 rpm with Ti-70.1 rotor or 390,000 g, 75 min, 4°C) to separate pellet C and supernatant C. Pellet C was washed, centrifuged and collected as the endoplasmic reticulum fraction. Supernatant C was collected as the cytosol fraction. DAG and ceramide concentrations (19), hepatic long-chain acyl-CoA (19), acetyl- and malonyl-CoA (9) were measured as previously described.

Tissue TAG content was measured by a standard kit (Sekisui/Fujifilm) after extraction by the method of Bligh and Dyer (194). For nPKC translocation, cytoplasm and plasma membrane fractions were separated by ultracentrifugation as previously described (67, 71).

Insulin signaling and Western blotting

IRS-1 and IRS-2 associated PI3K activity were determined as previously described (217). Briefly, IRS-1 and IRS-2 associated PI3K activities were measured in liver and muscle extracts after immunoprecipitation with IRS-1 antibody (BD Transduction Laboratories) or IRS-2 antibody (Cell Signaling)/agarose conjugate overnight at 4 °C. Then the incorporation of ^{32}P into PI to yield phosphatidylinositol-3-monophosphate was measured to determine the IRS-1 and IRS-2 associated PI3K activity.

Proteins from tissue lysate were separated by 4–12% sodium dodecyl sulfate polyacrylamide gel electrophoresis (SDS-PAGE) (Invitrogen) and then transferred onto polyvinylidene difluoride membranes (Millipore). After blocking in 5% bovine serum albumin (BSA)/tris buffered saline with tween (TBST) (10 mM Tris, 100 mM NaCl, and 0.1% Tween-20) solution, membranes were incubated overnight at 4°C with antibodies obtained from Cell Signaling Technology (pIRK-Y1162, IRK, GAPDH, pAkt-S473, Akt, pJNK, peNOS, AMPK, pAMPK, ACC, pACC, Perilipin, ATGL, pHSL and HSL), BD Transduction Laboratories (PKCε, PKCθ and eNOS), Shulman Lab (pIRK T1160)(219), EMD Millipore (JNK), VALAsciences (pPerilipin)and Abcam (Na/K ATPase and pATGL). After washing with TBST, membranes were incubated with horseradish peroxidase-conjugated secondary antibodies and detection was performed with enhanced chemiluminescence. For assaying the IRK-T1160 phosphorylation, after protein concentration quantitation, protein samples were first immunoprecipitated by Dynabeads M-270 Epoxy (Invitrogen) conjugated with D2 anti-IR alpha-subunit antibody. The primary antibody solution was diluted 1:100 – 1:200 for pIRK-T1160 detection.

Hepatic VLDL-TG production

Hepatic VLDL-TG production was assessed as previously described (234). In order to determine the basal plasma TAG level, after overnight fasting, blood samples were collected. Mice were injected intraperitoneally with poloxamer 407 (1g/ kg of body weight; Sigma Aldrich) to inhibit tissue LPL activity and blood samples were collected at 1, 2, 3, 4 hours after injection. The VLDL-TG production rate was calculated by the resultant increase in plasma TAG concentrations.

Oral lipid tolerance test and tissue-specific lipid uptake

Lipid clearance and tissue-specific uptake were measured by using [9,10-^{3}H] triolein as previously described (234, 235). After overnight fasting, mice received a gavage of a mixed meal: 10ul/g 10% dextrose in Intralipid (20%; Abbott Laboratories) conjugated with 10μCi of [9,10-^{3}H]triolein (PerkinElmer). Blood was collected by tail vein massage at 0, 1, 2, 3, and 4h for plasma TAG determination. Plasma TAG concentrations was measured by a standard kit (Sekisui/Fujifilm) and ^{3}H radioactivity was measured by scintillation counter.

Lipoprotein lipase activity assay

LPL activity was assessed as previously described (236, 237). Briefly, for plasma LPL activity, blood samples were collected after overnight fasting to determine basal plasma TAG and LPL activity. Then mice were injected intravenously with heparin (50U/ kg of body weight) and blood samples were taken after 10 minutes injection. Post-heparin plasma LPL activity was assessed by a fluorometric assay (Cell Biolabs). Tissue LPL was extracted by incubation of tissue at 37°C for 1 h in phosphate-buffered saline (PBS) with 5 U/ml heparin and 2 mg/ml bovine serum albumin. Samples were centrifuged at 900g for 15 minutes and the supernatant tissue LPL activities were measured in the presence of heat-inactivated mouse serum using a fluorometric assay (Cell Biolabs).

Statistical analysis

All data are expressed as the mean ± SEM. Results were assessed using two-tailed unpaired Student's t-test or two-way ANOVA. *P<0.05, **P<0.01, *P<0.05, **P<0.01, ***P<0.001, ****P<0.0001. GraphPad Prism 8.0 was used for all statistical analyses. In most cases, n = 6-9 per group, unless otherwise indicated in the figure legends.

Chapter 7

Summary and Future directions

Multiple studies have shown that chronic low-grade inflammation in obesity is a major pathogenic factor associated with insulin resistance and type 2 diabetes in both rodents and humans. However, the molecular mechanisms by which inflammation regulates whole-body metabolic dysfunction have remained elusive. *O*-GlcNAc signaling has been shown to be involved in neutrophil chemotaxis, B cell activation, and T cell self-renewal and activation. Recent studies also show that downregulation of *O*-GlcNAc signaling promotes innate immune responses in acute microbial infection. Together, these results suggest that *O*-GlcNAc signaling plays important roles in fine-tuning immune responses under various nutritional and pathological conditions. Those findings raised the question of whether *O*-GlcNAc signaling in macrophage senses metabolic status and directly regulates whole-body metabolic homeostasis. To test the hypothesis, we developed an OGT MKO mouse model and utilized comprehensive methods to elucidate the mechanisms. For the first time, we demonstrate an anti-inflammatory, anti-diabetic role of macrophage *O*-GlcNAc signaling. Our study showed several essential roles that O-GlcNAc homeostasis plays in immune actions and metabolic actions in response to excessive calorie intake, including: 1) reduced O-GlcNAc signaling increases macrophage pro-inflammatory activation; 2) increases WAT inflammation and lipolysis; 3) increases fatty acid delivery to liver and skeletal muscle and reduces TAG, DAG content, resulting in reduced novel PKC activation and impaired insulin sensitivity. Furthermore, we found that O-GlcNAc signaling regulates mTORC1/S6K1 and AMPK pathways, which are the novel pathways to regulate macrophage activation. Taken together, this study defines *O*-GlcNAc signaling as a suppressor of pro-inflammatory macrophage activation and adds new insight into metabolic regulation of macrophage activation. O-GlcNAc signaling may serve as a novel target to treat obesity-induced insulin resistance, hepatic steatosis and type 2 diabetes.

For future work, it would be interesting to figure out why *O*-GlcNAc signaling is reduced during LPS-induced M1 polarization **(Fig. 1D and S1D)** by tracing the glucose during WT and OGT MKO macrophage polarization. A growing body of evidence emphasizes the importance of metabolism in functional activation of macrophages (238). We hypothesize that the decrease of *O*-GlcNAc signaling in pro-inflammatory macrophage may be due to increased glucose utilization (e.g., glycolysis and/or glucose oxidation). Studies have been shown that microglial inflammation determines the immunologic response of the mediobasal hypothalamus to dietary excess and regulates hypothalamic control of energy homeostasis in mice (239). We observed that HFD-fed OGT MKO mice had increased food intake **(Fig. S3L)**, suggesting that microglial inflammation may also play a role. The mechanisms linking microglia inflammation and its metabolic consequences could also be studied.

As indicated by these data, suppressing inflammation and ameliorating insulin resistance could be important to treat type 2 diabetes. Adiponectin has emerged as a promising therapeutic agent to reduce inflammation and ameliorate insulin resistance. We then performed a comprehensive set of metabolic flux analyses to assess the effects of long-term adiponectin treatment on glucose and lipid metabolism *in vivo* and understand the underlying mechanisms. I hypothesize that adiponectin administration will result in reduced ectopic lipid accumulation due to increased mitochondrial oxidation, decreased lipolysis and/or reduced lipid uptake into liver and skeletal muscle, leading to improved insulin sensitivity. By testing possible hypotheses, our results showed that adiponectin administration ameliorates insulin resistance by two major mechanisms: 1) adiponectin treatment promotes increased WAT LPL activity, which may lead to increased uptake of triglyceride into WAT thus diverting circulating triglyceride away from storage in liver and skeletal muscle; 2) adiponectin treatment promotes increased fatty acid oxidation in skeletal muscle, which may be attributed to the activation of AMPK and eNOS. The pros

for adiponectin to become a potential agent to treat type 2 diabetes are: 1) The dose for adiponectin is relatively small; 2) adiponectin has novel mechanisms of increasing insulin sensitivity by targeting WAT LPL activity, which could be used as a combination with currently available therapy. The cons for adiponectin to become a potential therapy are: 1) adiponectin is a protein, which requires a relative restricted storage requirement; 2) adiponectin could increase WAT mass.

In future studies, it will be essential to elucidate the mechanisms by which adiponectin specifically activates WAT LPL. One hypothesis is that adiponectin may bind with scaffold proteins and then bind specific LPL regulators in white adipose tissue to regulate LPL activity. Another hypothesis is that adiponectin may increase WAT LPL activity by increasing LPL and VLDL receptor mRNA levels. It has also been uncovered that one dose of adiponectin injection caused a dramatic increase in the glucose infusion rate (GINF) within 30-40 minutes in euglycemic clamp (114). However, the underlying mechanisms are still unclear. It is a very rapid process which may not involve transcriptional and translational regulation. As a result, a novel yet unknown mechanism may be involved in the acute injection of adiponectin.

REFERENCE

1. H. Wu, C. M. Ballantyne, Metabolic Inflammation and Insulin Resistance in Obesity. *Circ Res* **126**, 1549-1564 (2020).
2. N. C. D. R. F. Collaboration, Worldwide trends in body-mass index, underweight, overweight, and obesity from 1975 to 2016: a pooled analysis of 2416 population-based measurement studies in 128.9 million children, adolescents, and adults. *Lancet* **390**, 2627-2642 (2017).
3. Z. Lu, Y. Li, J. Song, Characterization and Treatment of Inflammation and Insulin Resistance in Obese Adipose Tissue. *Diabetes Metab Syndr Obes* **13**, 3449-3460 (2020).
4. J. P. Boyle, T. J. Thompson, E. W. Gregg, L. E. Barker, D. F. Williamson, Projection of the year 2050 burden of diabetes in the US adult population: dynamic modeling of incidence, mortality, and prediabetes prevalence. *Population health metrics* **8**, 29 (2010).
5. G. I. Shulman, Ectopic fat in insulin resistance, dyslipidemia, and cardiometabolic disease. *The New England journal of medicine* **371**, 1131-1141 (2014).
6. V. T. Samuel, G. I. Shulman, The pathogenesis of insulin resistance: integrating signaling pathways and substrate flux. *J Clin Invest* **126**, 12-22 (2016).
7. V. T. Samuel, G. I. Shulman, Mechanisms for insulin resistance: common threads and missing links. *Cell* **148**, 852-871 (2012).
8. Y. S. Lee, J. Wollam, J. M. Olefsky, An Integrated View of Immunometabolism. *Cell* **172**, 22-40 (2018).
9. R. J. Perry *et al.*, Hepatic acetyl CoA links adipose tissue inflammation to hepatic insulin resistance and type 2 diabetes. *Cell* **160**, 745-758 (2015).
10. L. van Beek *et al.*, Increased systemic and adipose tissue inflammation differentiates obese women with T2DM from obese women with normal glucose tolerance. *Metabolism* **63**, 492-501 (2014).
11. A. Green, S. B. Dobias, D. J. Walters, A. R. Brasier, Tumor necrosis factor increases the rate of lipolysis in primary cultures of adipocytes without altering levels of hormone-sensitive lipase. *Endocrinology* **134**, 2581-2588 (1994).
12. G. Fruhbeck, L. Mendez-Gimenez, J. A. Fernandez-Formoso, S. Fernandez, A. Rodriguez, Regulation of adipocyte lipolysis. *Nutr Res Rev* **27**, 63-93 (2014).
13. P. J. Randle, P. B. Garland, C. N. Hales, E. A. Newsholme, The glucose fatty-acid cycle. Its role in insulin sensitivity and the metabolic disturbances of diabetes mellitus. *Lancet (London, England)* **1**, 785-789 (1963).
14. G. W. Cline *et al.*, Impaired glucose transport as a cause of decreased insulin-stimulated muscle glycogen synthesis in type 2 diabetes. *The New England journal of medicine* **341**, 240-246 (1999).
15. A. Dresner *et al.*, Effects of free fatty acids on glucose transport and IRS-1-associated phosphatidylinositol 3-kinase activity. *J Clin Invest* **103**, 253-259 (1999).

16. M. Krssak *et al.*, Intramyocellular lipid concentrations are correlated with insulin sensitivity in humans: a 1H NMR spectroscopy study. *Diabetologia* **42**, 113-116 (1999).
17. M. C. Petersen *et al.*, Insulin receptor Thr1160 phosphorylation mediates lipid-induced hepatic insulin resistance. *J Clin Invest* **126**, 4361-4371 (2016).
18. V. T. Samuel *et al.*, Inhibition of protein kinase Cepsilon prevents hepatic insulin resistance in nonalcoholic fatty liver disease. *J Clin Invest* **117**, 739-745 (2007).
19. C. Yu *et al.*, Mechanism by which fatty acids inhibit insulin activation of insulin receptor substrate-1 (IRS-1)-associated phosphatidylinositol 3-kinase activity in muscle. *J Biol Chem* **277**, 50230-50236 (2002).
20. M. Roden *et al.*, Mechanism of free fatty acid-induced insulin resistance in humans. *J Clin Invest* **97**, 2859-2865 (1996).
21. R. R. Holman, S. K. Paul, M. A. Bethel, D. R. Matthews, H. A. Neil, 10-year follow-up of intensive glucose control in type 2 diabetes. *The New England journal of medicine* **359**, 1577-1589 (2008).
22. S. E. Kahn, M. E. Cooper, S. Del Prato, Pathophysiology and treatment of type 2 diabetes: perspectives on the past, present, and future. *The Lancet* **383**, 1068-1083 (2014).
23. M. Iwabu *et al.*, Adiponectin and AdipoR1 regulate PGC-1alpha and mitochondria by Ca(2+) and AMPK/SIRT1. *Nature* **464**, 1313-1319 (2010).
24. N. Maeda *et al.*, Diet-induced insulin resistance in mice lacking adiponectin/ACRP30. *Nat Med* **8**, 731-737 (2002).
25. K. Hotta *et al.*, Circulating concentrations of the adipocyte protein adiponectin are decreased in parallel with reduced insulin sensitivity during the progression to type 2 diabetes in rhesus monkeys. *Diabetes* **50**, 1126-1133 (2001).
26. C. Weyer *et al.*, Hypoadiponectinemia in obesity and type 2 diabetes: close association with insulin resistance and hyperinsulinemia. *The Journal of clinical endocrinology and metabolism* **86**, 1930-1935 (2001).
27. T. P. Combs *et al.*, A transgenic mouse with a deletion in the collagenous domain of adiponectin displays elevated circulating adiponectin and improved insulin sensitivity. *Endocrinology* **145**, 367-383 (2004).
28. N. Kubota *et al.*, Disruption of adiponectin causes insulin resistance and neointimal formation. *The Journal of biological chemistry* **277**, 25863-25866 (2002).
29. L. J. Watson *et al.*, O-linked beta-N-acetylglucosamine transferase is indispensable in the failing heart. *Proc Natl Acad Sci U S A* **107**, 17797-17802 (2010).
30. L. J. Watson *et al.*, Cardiomyocyte Ogt is essential for postnatal viability. *Am J Physiol Heart Circ Physiol* **306**, H142-153 (2014).
31. S. P. Weisberg *et al.*, Obesity is associated with macrophage accumulation in adipose tissue. *J Clin Invest* **112**, 1796-1808 (2003).
32. H. Xu *et al.*, Chronic inflammation in fat plays a crucial role in the development of obesity-related insulin resistance. *J Clin Invest* **112**, 1821-1830 (2003).

33. D. Cai *et al.*, Local and systemic insulin resistance resulting from hepatic activation of IKK-beta and NF-kappaB. *Nat Med* **11**, 183-190 (2005).
34. E. J. Park *et al.*, Dietary and genetic obesity promote liver inflammation and tumorigenesis by enhancing IL-6 and TNF expression. *Cell* **140**, 197-208 (2010).
35. M. Saghizadeh, J. M. Ong, W. T. Garvey, R. R. Henry, P. A. Kern, The expression of TNF alpha by human muscle. Relationship to insulin resistance. *J Clin Invest* **97**, 1111-1116 (1996).
36. H. Wu, C. M. Ballantyne, Skeletal muscle inflammation and insulin resistance in obesity. *J Clin Invest* **127**, 43-54 (2017).
37. J. A. Ehses *et al.*, Increased number of islet-associated macrophages in type 2 diabetes. *Diabetes* **56**, 2356-2370 (2007).
38. K. Eguchi, R. Nagai, Islet inflammation in type 2 diabetes and physiology. *J Clin Invest* **127**, 14-23 (2017).
39. C. T. De Souza *et al.*, Consumption of a fat-rich diet activates a proinflammatory response and induces insulin resistance in the hypothalamus. *Endocrinology* **146**, 4192-4199 (2005).
40. P. J. Pistell *et al.*, Cognitive impairment following high fat diet consumption is associated with brain inflammation. *J Neuroimmunol* **219**, 25-32 (2010).
41. C. B. de La Serre *et al.*, Propensity to high-fat diet-induced obesity in rats is associated with changes in the gut microbiota and gut inflammation. *Am J Physiol Gastrointest Liver Physiol* **299**, G440-448 (2010).
42. P. D. Cani *et al.*, Changes in gut microbiota control inflammation in obese mice through a mechanism involving GLP-2-driven improvement of gut permeability. *Gut* **58**, 1091-1103 (2009).
43. K. T. Uysal, S. M. Wiesbrock, M. W. Marino, G. S. Hotamisligil, Protection from obesity-induced insulin resistance in mice lacking TNF-alpha function. *Nature* **389**, 610-614 (1997).
44. G. S. Hotamisligil, N. S. Shargill, B. M. Spiegelman, Adipose expression of tumor necrosis factor-alpha: direct role in obesity-linked insulin resistance. *Science* **259**, 87-91 (1993).
45. S. Talukdar *et al.*, Neutrophils mediate insulin resistance in mice fed a high-fat diet through secreted elastase. *Nat Med* **18**, 1407-1412 (2012).
46. S. Nishimura *et al.*, CD8+ effector T cells contribute to macrophage recruitment and adipose tissue inflammation in obesity. *Nat Med* **15**, 914-920 (2009).
47. D. A. Winer *et al.*, B cells promote insulin resistance through modulation of T cells and production of pathogenic IgG antibodies. *Nat Med* **17**, 610-617 (2011).
48. T. S. Nielsen, N. Jessen, J. O. Jorgensen, N. Moller, S. Lund, Dissecting adipose tissue lipolysis: molecular regulation and implications for metabolic disease. *J Mol Endocrinol* **52**, R199-222 (2014).
49. C. N. Lumeng, J. L. Bodzin, A. R. Saltiel, Obesity induces a phenotypic switch in adipose tissue macrophage polarization. *J Clin Invest* **117**, 175-184 (2007).
50. R. J. Perry *et al.*, Hepatic acetyl CoA links adipose tissue inflammation to hepatic insulin resistance and type 2 diabetes. *Cell* **160**, 745-758 (2015).

51. H. Kane, L. Lynch, Innate Immune Control of Adipose Tissue Homeostasis. *Trends Immunol* **40**, 857-872 (2019).
52. J. Chmelar, K. J. Chung, T. Chavakis, The role of innate immune cells in obese adipose tissue inflammation and development of insulin resistance. *Thromb Haemost* **109**, 399-406 (2013).
53. W. Trim, J. E. Turner, D. Thompson, Parallels in Immunometabolic Adipose Tissue Dysfunction with Ageing and Obesity. *Front Immunol* **9**, 169 (2018).
54. Y. Wang, P. M. Nishina, J. K. Naggert, Degradation of IRS1 leads to impaired glucose uptake in adipose tissue of the type 2 diabetes mouse model TALLYHO/Jng. *J Endocrinol* **203**, 65-74 (2009).
55. K. W. Cho *et al.*, Adipose Tissue Dendritic Cells Are Independent Contributors to Obesity-Induced Inflammation and Insulin Resistance. *J Immunol* **197**, 3650-3661 (2016).
56. K. J. Chung, M. Nati, T. Chavakis, A. Chatzigeorgiou, Innate immune cells in the adipose tissue. *Rev Endocr Metab Disord* **19**, 283-292 (2018).
57. M. Stefanovic-Racic *et al.*, Dendritic cells promote macrophage infiltration and comprise a substantial proportion of obesity-associated increases in CD11c+ cells in adipose tissue and liver. *Diabetes* **61**, 2330-2339 (2012).
58. J. Liu *et al.*, Genetic deficiency and pharmacological stabilization of mast cells reduce diet-induced obesity and diabetes in mice. *Nat Med* **15**, 940-945 (2009).
59. D. E. Lackey, J. M. Olefsky, Regulation of metabolism by the innate immune system. *Nat Rev Endocrinol* **12**, 15-28 (2016).
60. S. Sun, Y. Ji, S. Kersten, L. Qi, Mechanisms of inflammatory responses in obese adipose tissue. *Annu Rev Nutr* **32**, 261-286 (2012).
61. V. Dam, T. Sikder, S. Santosa, From neutrophils to macrophages: differences in regional adipose tissue depots. *Obes Rev* **17**, 1-17 (2016).
62. L. Ding *et al.*, Akt3 deficiency in macrophages promotes foam cell formation and atherosclerosis in mice. *Cell Metab* **15**, 861-872 (2012).
63. S. Winer *et al.*, Normalization of obesity-associated insulin resistance through immunotherapy. *Nat Med* **15**, 921-929 (2009).
64. R. Zhou, A. Tardivel, B. Thorens, I. Choi, J. Tschopp, Thioredoxin-interacting protein links oxidative stress to inflammasome activation. *Nat Immunol* **11**, 136-140 (2010).
65. G. I. Shulman, Ectopic fat in insulin resistance, dyslipidemia, and cardiometabolic disease. *N Engl J Med* **371**, 2237-2238 (2014).
66. M. C. Petersen, G. I. Shulman, Roles of Diacylglycerols and Ceramides in Hepatic Insulin Resistance. *Trends Pharmacol Sci* **38**, 649-665 (2017).
67. N. Kumashiro *et al.*, Cellular mechanism of insulin resistance in nonalcoholic fatty liver disease. *Proc Natl Acad Sci U S A* **108**, 16381-16385 (2011).
68. J. Szendroedi *et al.*, Role of diacylglycerol activation of PKCtheta in lipid-induced muscle insulin resistance in humans. *Proc Natl Acad Sci U S A* **111**, 9597-9602 (2014).

69. F. Magkos *et al.*, Intrahepatic diacylglycerol content is associated with hepatic insulin resistance in obese subjects. *Gastroenterology* **142**, 1444-1446 e1442 (2012).
70. P. K. Luukkonen *et al.*, Hepatic ceramides dissociate steatosis and insulin resistance in patients with non-alcoholic fatty liver disease. *J Hepatol* **64**, 1167-1175 (2016).
71. V. T. Samuel *et al.*, Mechanism of hepatic insulin resistance in non-alcoholic fatty liver disease. *J Biol Chem* **279**, 32345-32353 (2004).
72. A. Karasik, P. L. Rothenberg, K. Yamada, M. F. White, C. R. Kahn, Increased protein kinase C activity is linked to reduced insulin receptor autophosphorylation in liver of starved rats. *J Biol Chem* **265**, 10226-10231 (1990).
73. M. Kellerer, J. Mushack, H. Mischak, H. U. Haring, Protein kinase C (PKC) epsilon enhances the inhibitory effect of TNF alpha on insulin signaling in HEK293 cells. *FEBS Lett* **418**, 119-122 (1997).
74. S. Timmers, P. Schrauwen, J. de Vogel, Muscular diacylglycerol metabolism and insulin resistance. *Physiol Behav* **94**, 242-251 (2008).
75. S. A. Summers, B. H. Goodpaster, CrossTalk proposal: Intramyocellular ceramide accumulation does modulate insulin resistance. *J Physiol* **594**, 3167-3170 (2016).
76. S. M. Turpin *et al.*, Obesity-induced CerS6-dependent C16:0 ceramide production promotes weight gain and glucose intolerance. *Cell Metab* **20**, 678-686 (2014).
77. S. Raichur *et al.*, CerS2 Haploinsufficiency Inhibits beta-Oxidation and Confers Susceptibility to Diet-Induced Steatohepatitis and Insulin Resistance. *Cell Metab* **20**, 919 (2014).
78. T. Hla, R. Kolesnick, C16:0-ceramide signals insulin resistance. *Cell Metab* **20**, 703-705 (2014).
79. M. Salinas, R. Lopez-Valdaliso, D. Martin, A. Alvarez, A. Cuadrado, Inhibition of PKB/Akt1 by C2-ceramide involves activation of ceramide-activated protein phosphatase in PC12 cells. *Mol Cell Neurosci* **15**, 156-169 (2000).
80. K. M. Schubert, M. P. Scheid, V. Duronio, Ceramide inhibits protein kinase B/Akt by promoting dephosphorylation of serine 473. *J Biol Chem* **275**, 13330-13335 (2000).
81. S. Stratford, K. L. Hoehn, F. Liu, S. A. Summers, Regulation of insulin action by ceramide: dual mechanisms linking ceramide accumulation to the inhibition of Akt/protein kinase B. *J Biol Chem* **279**, 36608-36615 (2004).
82. V. Bermudez *et al.*, Prevalence and Associated Factors of Insulin Resistance in Adults from Maracaibo City, Venezuela. *Adv Prev Med* **2016**, 9405105 (2016).
83. W. H. O. (WHO) (2017) The top ten causes of death.
84. M. Laakso, J. Kuusisto, Insulin resistance and hyperglycaemia in cardiovascular disease development. *Nat Rev Endocrinol* **10**, 293-302 (2014).
85. J. J. Marin-Penalver, I. Martin-Timon, C. Sevillano-Collantes, F. J. Del Canizo-Gomez, Update on the treatment of type 2 diabetes mellitus. *World J Diabetes* **7**, 354-395 (2016).

86. N. R. Shin *et al.*, An increase in the Akkermansia spp. population induced by metformin treatment improves glucose homeostasis in diet-induced obese mice. *Gut* **63**, 727-735 (2014).
87. H. An, L. He, Current understanding of metformin effect on the control of hyperglycemia in diabetes. *J Endocrinol* **228**, R97-106 (2016).
88. R. Song, Mechanism of Metformin: A Tale of Two Sites. *Diabetes Care* **39**, 187-189 (2016).
89. J. Bryan, A. Crane, W. H. Vila-Carriles, A. P. Babenko, L. Aguilar-Bryan, Insulin secretagogues, sulfonylurea receptors and K(ATP) channels. *Curr Pharm Des* **11**, 2699-2716 (2005).
90. R. Eldor, I. Raz, Diabetes therapy--focus on Asia: second-line therapy debate: insulin/secretagogues. *Diabetes Metab Res Rev* **28 Suppl 2**, 85-89 (2012).
91. A. Takahashi *et al.*, Sulfonylurea and glinide reduce insulin content, functional expression of K(ATP) channels, and accelerate apoptotic beta-cell death in the chronic phase. *Diabetes Res Clin Pract* **77**, 343-350 (2007).
92. K. Maedler *et al.*, Sulfonylurea induced beta-cell apoptosis in cultured human islets. *J Clin Endocrinol Metab* **90**, 501-506 (2005).
93. Anonymous, Intensive blood-glucose control with sulphonylureas or insulin compared with conventional treatment and risk of complications in patients with type 2 diabetes (UKPDS 33). UK Prospective Diabetes Study (UKPDS) Group. *Lancet* **352**, 837-853 (1998).
94. P. C. Lim, C. P. Chong, What's next after metformin? focus on sulphonylurea: add-on or combination therapy. *Pharm Pract (Granada)* **13**, 606 (2015).
95. L. J. Scott, Repaglinide: a review of its use in type 2 diabetes mellitus. *Drugs* **72**, 249-272 (2012).
96. C. L. Morgan, J. Mukherjee, S. Jenkins-Jones, S. E. Holden, C. J. Currie, Association between first-line monotherapy with sulphonylurea versus metformin and risk of all-cause mortality and cardiovascular events: a retrospective, observational study. *Diabetes Obes Metab* **16**, 957-962 (2014).
97. F. A. van de Laar *et al.*, Alpha-glucosidase inhibitors for patients with type 2 diabetes: results from a Cochrane systematic review and meta-analysis. *Diabetes Care* **28**, 154-163 (2005).
98. M. Abe, K. Okada, M. Soma, Antidiabetic agents in patients with chronic kidney disease and end-stage renal disease on dialysis: metabolism and clinical practice. *Curr Drug Metab* **12**, 57-69 (2011).
99. C. C. Kao *et al.*, Risk of liver injury after alpha-glucosidase inhibitor therapy in advanced chronic kidney disease patients. *Sci Rep* **6**, 18996 (2016).
100. I. Bogacka, H. Xie, G. A. Bray, S. R. Smith, The effect of pioglitazone on peroxisome proliferator-activated receptor-gamma target genes related to lipid storage in vivo. *Diabetes Care* **27**, 1660-1667 (2004).
101. R. W. Nesto *et al.*, Thiazolidinedione use, fluid retention, and congestive heart failure: a consensus statement from the American Heart Association and American Diabetes Association. October 7, 2003. *Circulation* **108**, 2941-2948 (2003).

102. M. R. Weir, The kidney and type 2 diabetes mellitus: therapeutic implications of SGLT2 inhibitors. *Postgrad Med* **128**, 290-298 (2016).
103. S. Sarnoski-Brocavich, O. Hilas, Canagliflozin (invokana), a novel oral agent for type-2 diabetes. *P T* **38**, 656-666 (2013).
104. S. E. Kahn, M. E. Cooper, S. Del Prato, Pathophysiology and treatment of type 2 diabetes: perspectives on the past, present, and future. *Lancet* **383**, 1068-1083 (2014).
105. R. H. Tuligenga, Intensive glycaemic control and cognitive decline in patients with type 2 diabetes: a meta-analysis. *Endocr Connect* **4**, R16-24 (2015).
106. T. Kadowaki, T. Yamauchi, Adiponectin and adiponectin receptors. *Endocrine reviews* **26**, 439-451 (2005).
107. Q. Liu *et al.*, Adiponectin regulates expression of hepatic genes critical for glucose and lipid metabolism. *Proc Natl Acad Sci U S A* **109**, 14568-14573 (2012).
108. K. Hotta *et al.*, Plasma concentrations of a novel, adipose-specific protein, adiponectin, in type 2 diabetic patients. *Arteriosclerosis, thrombosis, and vascular biology* **20**, 1595-1599 (2000).
109. C. M. Halleux *et al.*, Secretion of adiponectin and regulation of apM1 gene expression in human visceral adipose tissue. *Biochem Biophys Res Commun* **288**, 1102-1107 (2001).
110. J. Fruebis *et al.*, Proteolytic cleavage product of 30-kDa adipocyte complement-related protein increases fatty acid oxidation in muscle and causes weight loss in mice. *Proc Natl Acad Sci U S A* **98**, 2005-2010 (2001).
111. A. H. Berg, T. P. Combs, X. Du, M. Brownlee, P. E. Scherer, The adipocyte-secreted protein Acrp30 enhances hepatic insulin action. *Nat Med* **7**, 947-953 (2001).
112. T. Yamauchi *et al.*, The fat-derived hormone adiponectin reverses insulin resistance associated with both lipoatrophy and obesity. *Nat Med* **7**, 941-946 (2001).
113. X. Hui, K. S. Lam, P. M. Vanhoutte, A. Xu, Adiponectin and cardiovascular health: an update. *Br J Pharmacol* **165**, 574-590 (2012).
114. W. L. Holland *et al.*, Receptor-mediated activation of ceramidase activity initiates the pleiotropic actions of adiponectin. *Nat Med* **17**, 55-63 (2011).
115. T. Yamauchi *et al.*, Adiponectin stimulates glucose utilization and fatty-acid oxidation by activating AMP-activated protein kinase. *Nat Med* **8**, 1288-1295 (2002).
116. A. Xu *et al.*, The fat-derived hormone adiponectin alleviates alcoholic and nonalcoholic fatty liver diseases in mice. *Journal of Clinical Investigation* **112**, 91-100 (2003).
117. M. Awazawa *et al.*, Adiponectin suppresses hepatic SREBP1c expression in an AdipoR1/LKB1/AMPK dependent pathway. *Biochem Biophys Res Commun* **382**, 51-56 (2009).
118. E. Tomas *et al.*, Enhanced muscle fat oxidation and glucose transport by ACRP30 globular domain: acetyl-CoA carboxylase inhibition and AMP-activated protein kinase activation. *Proc Natl Acad Sci U S A* **99**, 16309-16313 (2002).

119. F. Magkos *et al.*, Intrahepatic diacylglycerol content is associated with hepatic insulin resistance in obese subjects. *Gastroenterology* **142**, 1444-1446.e1442 (2012).
120. N. Turner *et al.*, Distinct patterns of tissue-specific lipid accumulation during the induction of insulin resistance in mice by high-fat feeding. *Diabetologia* **56**, 1638-1648 (2013).
121. S. E. Kahn, R. L. Hull, K. M. Utzschneider, Mechanisms linking obesity to insulin resistance and type 2 diabetes. *Nature* **444**, 840-846 (2006).
122. M. F. Gregor, G. S. Hotamisligil, Inflammatory mechanisms in obesity. *Annu Rev Immunol* **29**, 415-445 (2011).
123. A. R. Saltiel, J. M. Olefsky, Inflammatory mechanisms linking obesity and metabolic disease. *J Clin Invest* **127**, 1-4 (2017).
124. S. M. Reilly, A. R. Saltiel, Adapting to obesity with adipose tissue inflammation. *Nat Rev Endocrinol* **13**, 633-643 (2017).
125. A. Asghar, N. Sheikh, Role of immune cells in obesity induced low grade inflammation and insulin resistance. *Cell Immunol* **315**, 18-26 (2017).
126. K. J. Chung, M. Nati, T. Chavakis, A. Chatzigeorgiou, Innate immune cells in the adipose tissue. *Rev Endocr Metab Disord* 10.1007/s11154-018-9451-6 (2018).
127. L. Russo, C. N. Lumeng, Properties and functions of adipose tissue macrophages in obesity. *Immunology* **155**, 407-417 (2018).
128. E. L. Pearce, E. J. Pearce, Metabolic pathways in immune cell activation and quiescence. *Immunity* **38**, 633-643 (2013).
129. B. A. Olenchock, J. C. Rathmell, M. G. Vander Heiden, Biochemical Underpinnings of Immune Cell Metabolic Phenotypes. *Immunity* **46**, 703-713 (2017).
130. A. K. Jha *et al.*, Network integration of parallel metabolic and transcriptional data reveals metabolic modules that regulate macrophage polarization. *Immunity* **42**, 419-430 (2015).
131. P. K. Langston, M. Shibata, T. Horng, Metabolism Supports Macrophage Activation. *Front Immunol* **8**, 61 (2017).
132. M. R. Bond, J. A. Hanover, A little sugar goes a long way: the cell biology of O-GlcNAc. *J Cell Biol* **208**, 869-880 (2015).
133. S. Hardiville, G. W. Hart, Nutrient regulation of gene expression by O-GlcNAcylation of chromatin. *Curr Opin Chem Biol* **33**, 88-94 (2016).
134. X. Yang, K. Qian, Protein O-GlcNAcylation: emerging mechanisms and functions. *Nat Rev Mol Cell Biol* **18**, 452-465 (2017).
135. X. Yang *et al.*, Phosphoinositide signalling links O-GlcNAc transferase to insulin resistance. *Nature* **451**, 964-969 (2008).
136. A. Golks, T. T. Tran, J. F. Goetschy, D. Guerini, Requirement for O-linked N-acetylglucosaminyltransferase in lymphocytes activation. *EMBO J* **26**, 4368-4379 (2007).
137. K. Kawauchi, K. Araki, K. Tobiume, N. Tanaka, Loss of p53 enhances catalytic activity of IKKbeta through O-linked beta-N-acetyl glucosamine modification. *Proc Natl Acad Sci U S A* **106**, 3431-3436 (2009).

138. H. B. Ruan *et al.*, Calcium-dependent O-GlcNAc signaling drives liver autophagy in adaptation to starvation. *Genes Dev* **31**, 1655-1665 (2017).
139. J. P. Singh, K. Zhang, J. Wu, X. Yang, O-GlcNAc signaling in cancer metabolism and epigenetics. *Cancer Lett* **356**, 244-250 (2015).
140. S. Olivier-Van Stichelen, J. A. Hanover, You are what you eat: O-linked N-acetylglucosamine in disease, development and epigenetics. *Curr Opin Clin Nutr Metab Care* **18**, 339-345 (2015).
141. S. B. Peterson, G. W. Hart, New insights: A role for O-GlcNAcylation in diabetic complications. *Crit Rev Biochem Mol Biol* **51**, 150-161 (2016).
142. J. N. Wright, H. E. Collins, A. R. Wende, J. C. Chatham, O-GlcNAcylation and cardiovascular disease. *Biochem Soc Trans* **45**, 545-553 (2017).
143. D. A. McClain *et al.*, Altered glycan-dependent signaling induces insulin resistance and hyperleptinemia. *Proc Natl Acad Sci U S A* **99**, 10695-10699 (2002).
144. K. Vosseller, L. Wells, M. D. Lane, G. W. Hart, Elevated nucleocytoplasmic glycosylation by O-GlcNAc results in insulin resistance associated with defects in Akt activation in 3T3-L1 adipocytes. *Proc Natl Acad Sci U S A* **99**, 5313-5318 (2002).
145. H. B. Ruan *et al.*, O-GlcNAc transferase/host cell factor C1 complex regulates gluconeogenesis by modulating PGC-1alpha stability. *Cell Metab* **16**, 226-237 (2012).
146. R. Dentin, S. Hedrick, J. Xie, J. Yates, 3rd, M. Montminy, Hepatic glucose sensing via the CREB coactivator CRTC2. *Science* **319**, 1402-1405 (2008).
147. M. P. Housley *et al.*, O-GlcNAc regulates FoxO activation in response to glucose. *J Biol Chem* **283**, 16283-16292 (2008).
148. C. R. Torres, G. W. Hart, Topography and polypeptide distribution of terminal N-acetylglucosamine residues on the surfaces of intact lymphocytes. Evidence for O-linked GlcNAc. *J Biol Chem* **259**, 3308-3317 (1984).
149. H. Goldberg, C. Whiteside, I. G. Fantus, O-linked beta-N-acetylglucosamine supports p38 MAPK activation by high glucose in glomerular mesangial cells. *Am J Physiol Endocrinol Metab* **301**, E713-726 (2011).
150. M. Jiang *et al.*, Elevated O-GlcNAcylation promotes gastric cancer cells proliferation by modulating cell cycle related proteins and ERK 1/2 signaling. *Oncotarget* **7**, 61390-61402 (2016).
151. A. Chawla, K. D. Nguyen, Y. P. Goh, Macrophage-mediated inflammation in metabolic disease. *Nat Rev Immunol* **11**, 738-749 (2011).
152. D. Thomas, C. Apovian, Macrophage functions in lean and obese adipose tissue. *Metabolism* **72**, 120-143 (2017).
153. X. Y. Zhu *et al.*, Functional Plasticity of Adipose-Derived Stromal Cells During Development of Obesity. *Stem Cells Transl Med* **5**, 893-900 (2016).
154. P. J. Murray *et al.*, Macrophage activation and polarization: nomenclature and experimental guidelines. *Immunity* **41**, 14-20 (2014).
155. A. Shapouri-Moghaddam *et al.*, Macrophage plasticity, polarization, and function in health and disease. *J Cell Physiol* **233**, 6425-6440 (2018).

156. P. Italiani *et al.*, Transcriptomic profiling of the development of the inflammatory response in human monocytes in vitro. *PLoS One* **9**, e87680 (2014).
157. D. J. Westcott *et al.*, MGL1 promotes adipose tissue inflammation and insulin resistance by regulating 7/4hi monocytes in obesity. *J Exp Med* **206**, 3143-3156 (2009).
158. N. V. Serbina, E. G. Pamer, Monocyte emigration from bone marrow during bacterial infection requires signals mediated by chemokine receptor CCR2. *Nat Immunol* **7**, 311-317 (2006).
159. C. N. Lumeng, J. B. DelProposto, D. J. Westcott, A. R. Saltiel, Phenotypic switching of adipose tissue macrophages with obesity is generated by spatiotemporal differences in macrophage subtypes. *Diabetes* **57**, 3239-3246 (2008).
160. G. Schoiswohl *et al.*, Impact of Reduced ATGL-Mediated Adipocyte Lipolysis on Obesity-Associated Insulin Resistance and Inflammation in Male Mice. *Endocrinology* **156**, 3610-3624 (2015).
161. P. Morigny, M. Houssier, E. Mouisel, D. Langin, Adipocyte lipolysis and insulin resistance. *Biochimie* **125**, 259-266 (2016).
162. R. W. Grant, J. M. Stephens, Fat in flames: influence of cytokines and pattern recognition receptors on adipocyte lipolysis. *Am J Physiol Endocrinol Metab* **309**, E205-213 (2015).
163. B. Yan *et al.*, HDAC6 deacetylase activity is critical for lipopolysaccharide-induced activation of macrophages. *PLoS One* **9**, e110718 (2014).
164. Y. Lavin *et al.*, Tissue-resident macrophage enhancer landscapes are shaped by the local microenvironment. *Cell* **159**, 1312-1326 (2014).
165. Y. Chu *et al.*, Tet2 Regulates Osteoclast Differentiation by Interacting with Runx1 and Maintaining Genomic 5-Hydroxymethylcytosine (5hmC). *Genomics Proteomics Bioinformatics* **16**, 172-186 (2018).
166. W. B. Dias, W. D. Cheung, G. W. Hart, O-GlcNAcylation of kinases. *Biochem Biophys Res Commun* **422**, 224-228 (2012).
167. H. J. Kao *et al.*, A two-layered machine learning method to identify protein O-GlcNAcylation sites with O-GlcNAc transferase substrate motifs. *BMC Bioinformatics* **16 Suppl 18**, S10 (2015).
168. R. Gupta, S. Brunak, Prediction of glycosylation across the human proteome and the correlation to protein function. *Pac Symp Biocomput*, 310-322 (2002).
169. M. Mahalingam, D. J. Templeton, Constitutive activation of S6 kinase by deletion of amino-terminal autoinhibitory and rapamycin sensitivity domains. *Mol Cell Biol* **16**, 405-413 (1996).
170. Z. Hou, L. He, R. Z. Qi, Regulation of s6 kinase 1 activation by phosphorylation at ser-411. *J Biol Chem* **282**, 6922-6928 (2007).
171. B. Magnuson, B. Ekim, D. C. Fingar, Regulation and function of ribosomal protein S6 kinase (S6K) within mTOR signalling networks. *Biochem J* **441**, 1-21 (2012).
172. W. Ptak, M. Klimek, K. Bryniarski, M. Ptak, P. Majcher, Macrophage function in alloxan diabetic mice: expression of adhesion molecules, generation of monokines and oxygen and NO radicals. *Clin Exp Immunol* **114**, 13-18 (1998).

173. Y. Wen *et al.*, Elevated glucose and diabetes promote interleukin-12 cytokine gene expression in mouse macrophages. *Endocrinology* **147**, 2518-2525 (2006).
174. B. Sears, M. Perry, The role of fatty acids in insulin resistance. *Lipids Health Dis* **14**, 121 (2015).
175. I. H. Ryu, S. I. Do, Denitrosylation of S-nitrosylated OGT is triggered in LPS-stimulated innate immune response. *Biochem Biophys Res Commun* **408**, 52-57 (2011).
176. G. M. Zheng, C. Yu, Z. Yang, Puerarin suppresses production of nitric oxide and inducible nitric oxide synthase in lipopolysaccharide-induced N9 microglial cells through regulating MAPK phosphorylation, O-GlcNAcylation and NF-kappaB translocation. *Int J Oncol* **40**, 1610-1618 (2012).
177. J. S. Hwang *et al.*, Glucosamine improves survival in a mouse model of sepsis and attenuates sepsis-induced lung injury and inflammation. *J Biol Chem* 10.1074/jbc.RA118.004638 (2018).
178. M. S. Han *et al.*, JNK expression by macrophages promotes obesity-induced insulin resistance and inflammation. *Science* **339**, 218-222 (2013).
179. D. Patsouris *et al.*, Ablation of CD11c-positive cells normalizes insulin sensitivity in obese insulin resistant animals. *Cell Metab* **8**, 301-309 (2008).
180. V. Elgazar-Carmon, A. Rudich, N. Hadad, R. Levy, Neutrophils transiently infiltrate intra-abdominal fat early in the course of high-fat feeding. *J Lipid Res* **49**, 1894-1903 (2008).
181. G. S. Hotamisligil, E. Erbay, Nutrient sensing and inflammation in metabolic diseases. *Nat Rev Immunol* **8**, 923-934 (2008).
182. V. Byles *et al.*, The TSC-mTOR pathway regulates macrophage polarization. *Nat Commun* **4**, 2834 (2013).
183. L. Zhu *et al.*, TSC1 controls macrophage polarization to prevent inflammatory disease. *Nat Commun* **5**, 4696 (2014).
184. M. S. Yoon, The Role of Mammalian Target of Rapamycin (mTOR) in Insulin Signaling. *Nutrients* **9** (2017).
185. S. H. Um *et al.*, Absence of S6K1 protects against age- and diet-induced obesity while enhancing insulin sensitivity. *Nature* **431**, 200-205 (2004).
186. V. L. Sodi *et al.*, mTOR/MYC Axis Regulates O-GlcNAc Transferase Expression and O-GlcNAcylation in Breast Cancer. *Mol Cancer Res* **13**, 923-933 (2015).
187. J. Xu, J. Ji, X. H. Yan, Cross-talk between AMPK and mTOR in regulating energy balance. *Crit Rev Food Sci Nutr* **52**, 373-381 (2012).
188. R. Gelinas *et al.*, AMP-Activated Protein Kinase and O-GlcNAcylation, Two Partners Tightly Connected to Regulate Key Cellular Processes. *Front Endocrinol (Lausanne)* **9**, 519 (2018).
189. K. Man, V. I. Kutyavin, A. Chawla, Tissue Immunometabolism: Development, Physiology, and Pathobiology. *Cell Metab* **25**, 11-26 (2017).
190. P. Petrus *et al.*, Glutamine Links Obesity to Inflammation in Human White Adipose Tissue. *Cell Metabolism* https://doi.org/10.1016/j.cmet.2019.11.019 (2019).

191. E. C. Opara, A. Petro, A. Tevrizian, M. N. Feinglos, R. S. Surwit, L-glutamine supplementation of a high fat diet reduces body weight and attenuates hyperglycemia and hyperinsulinemia in C57BL/6J mice. *J Nutr* **126**, 273-279 (1996).
192. C. Barrientos, R. Racotta, L. Quevedo, Glucosamine attenuates increases of intraabdominal fat, serum leptin levels, and insulin resistance induced by a high-fat diet in rats. *Nutr Res* **30**, 791-800 (2010).
193. R. Shafi *et al.*, The O-GlcNAc transferase gene resides on the X chromosome and is essential for embryonic stem cell viability and mouse ontogeny. *Proc Natl Acad Sci U S A* **97**, 5735-5739 (2000).
194. E. G. Bligh, W. J. Dyer, A rapid method of total lipid extraction and purification. *Can J Biochem Physiol* **37**, 911-917 (1959).
195. J. S. Bogan, A. E. McKee, H. F. Lodish, Insulin-responsive compartments containing GLUT4 in 3T3-L1 and CHO cells: regulation by amino acid concentrations. *Mol Cell Biol* **21**, 4785-4806 (2001).
196. R. J. Perry *et al.*, Leptin Mediates a Glucose-Fatty Acid Cycle to Maintain Glucose Homeostasis in Starvation. *Cell* **172**, 234-248 e217 (2018).
197. D. F. Vatner *et al.*, Insulin-independent regulation of hepatic triglyceride synthesis by fatty acids. *Proc Natl Acad Sci U S A* **112**, 1143-1148 (2015).
198. P. Cohen *et al.*, Ablation of PRDM16 and beige adipose causes metabolic dysfunction and a subcutaneous to visceral fat switch. *Cell* **156**, 304-316 (2014).
199. X. Zhang, R. Goncalves, D. M. Mosser, The isolation and characterization of murine macrophages. *Curr Protoc Immunol* **Chapter 14**, Unit 14 11 (2008).
200. C. Trapnell, L. Pachter, S. L. Salzberg, TopHat: discovering splice junctions with RNA-Seq. *Bioinformatics* **25**, 1105-1111 (2009).
201. S. Anders, P. T. Pyl, W. Huber, HTSeq--a Python framework to work with high-throughput sequencing data. *Bioinformatics* **31**, 166-169 (2015).
202. M. D. Robinson, G. K. Smyth, Moderated statistical tests for assessing differences in tag abundance. *Bioinformatics* **23**, 2881-2887 (2007).
203. M. D. Robinson, G. K. Smyth, Small-sample estimation of negative binomial dispersion, with applications to SAGE data. *Biostatistics* **9**, 321-332 (2008).
204. O. A. MacDougald, Methods in Enzymology. Methods of adipose tissue biology, part B. Preface. *Methods Enzymol* **538**, xv (2014).
205. Y. Zheng, S. H. Ley, F. B. Hu, Global aetiology and epidemiology of type 2 diabetes mellitus and its complications. *Nat Rev Endocrinol* **14**, 88-98 (2018).
206. H. N. Jones, T. Jansson, T. L. Powell, Full-length adiponectin attenuates insulin signaling and inhibits insulin-stimulated amino Acid transport in human primary trophoblast cells. *Diabetes* **59**, 1161-1170 (2010).
207. R. A. Miller *et al.*, Adiponectin suppresses gluconeogenic gene expression in mouse hepatocytes independent of LKB1-AMPK signaling. *J Clin Invest* **121**, 2518-2528 (2011).
208. A. Xu *et al.*, The fat-derived hormone adiponectin alleviates alcoholic and nonalcoholic fatty liver diseases in mice. *J Clin Invest* **112**, 91-100 (2003).

209. M. Pagadala, T. Kasumov, A. J. McCullough, N. N. Zein, J. P. Kirwan, Role of ceramides in nonalcoholic fatty liver disease. *Trends in endocrinology and metabolism: TEM* **23**, 365-371 (2012).
210. A. U. Blachnio-Zabielska, M. Chacinska, M. H. Vendelbo, P. Zabielski, The Crucial Role of C18-Cer in Fat-Induced Skeletal Muscle Insulin Resistance. *Cell Physiol Biochem* **40**, 1207-1220 (2016).
211. J. D. Song *et al.*, Dissociation of Muscle Insulin Resistance from Alterations in Mitochondrial Substrate Preference. *Cell Metab* 10.1016/j.cmet.2020.09.008 (2020).
212. A. Guilherme, F. Henriques, A. H. Bedard, M. P. Czech, Molecular pathways linking adipose innervation to insulin action in obesity and diabetes mellitus. *Nat Rev Endocrinol* **15**, 207-225 (2019).
213. J. Y. Kim *et al.*, Obesity-associated improvements in metabolic profile through expansion of adipose tissue. *J Clin Invest* **117**, 2621-2637 (2007).
214. Y. Fu, N. Luo, R. L. Klein, W. T. Garvey, Adiponectin promotes adipocyte differentiation, insulin sensitivity, and lipid accumulation. *Journal of lipid research* **46**, 1369-1379 (2005).
215. G. S. Hotamisligil, Inflammation and metabolic disorders. *Nature* **444**, 860-867 (2006).
216. M. E. Griffin *et al.*, Free fatty acid-induced insulin resistance is associated with activation of protein kinase C theta and alterations in the insulin signaling cascade. *Diabetes* **48**, 1270-1274 (1999).
217. J. K. Kim *et al.*, PKC-theta knockout mice are protected from fat-induced insulin resistance. *J Clin Invest* **114**, 823-827 (2004).
218. L. T. Boni, R. R. Rando, The nature of protein kinase C activation by physically defined phospholipid vesicles and diacylglycerols. *J Biol Chem* **260**, 10819-10825 (1985).
219. K. Lyu *et al.*, A Membrane-Bound Diacylglycerol Species Induces PKC-Mediated Hepatic Insulin Resistance. *Cell Metab* 10.1016/j.cmet.2020.08.001 (2020).
220. H. Nomura *et al.*, Stereospecificity of diacylglycerol for stimulus-response coupling in platelets. *Biochem Biophys Res Commun* **140**, 1143-1151 (1986).
221. E. Sokolowska, A. Blachnio-Zabielska, The Role of Ceramides in Insulin Resistance. *Front Endocrinol (Lausanne)* **10**, 577 (2019).
222. H. Bays, L. Mandarino, R. A. DeFronzo, Role of the adipocyte, free fatty acids, and ectopic fat in pathogenesis of type 2 diabetes mellitus: peroxisomal proliferator-activated receptor agonists provide a rational therapeutic approach. *J Clin Endocrinol Metab* **89**, 463-478 (2004).
223. R. J. Perry *et al.*, Non-invasive assessment of hepatic mitochondrial metabolism by positional isotopomer NMR tracer analysis (PINTA). *Nat Commun* **8**, 798 (2017).
224. V. A. Lira *et al.*, Nitric oxide and AMPK cooperatively regulate PGC-1 in skeletal muscle cells. *J Physiol* **588**, 3551-3566 (2010).
225. P. H. Weinstock *et al.*, Lipoprotein lipase controls fatty acid entry into adipose tissue, but fat mass is preserved by endogenous synthesis in mice deficient in

adipose tissue lipoprotein lipase. *Proc Natl Acad Sci U S A* **94**, 10261-10266 (1997).
226. A. E. Achari, S. K. Jain, Adiponectin, a Therapeutic Target for Obesity, Diabetes, and Endothelial Dysfunction. *Int J Mol Sci* **18** (2017).
227. R. S. Ahima, J. S. Flier, Adipose tissue as an endocrine organ. *Trends Endocrinol Metab* **11**, 327-332 (2000).
228. V. Mohamed-Ali, J. H. Pinkney, S. W. Coppack, Adipose tissue as an endocrine and paracrine organ. *International journal of obesity and related metabolic disorders : journal of the International Association for the Study of Obesity* **22**, 1145-1158 (1998).
229. R. J. Perry *et al.*, Leptin mediates postprandial increases in body temperature through hypothalamus-adrenal medulla-adipose tissue crosstalk. *J Clin Invest* **130**, 2001-2016 (2020).
230. M. Awazawa *et al.*, Adiponectin enhances insulin sensitivity by increasing hepatic IRS-2 expression via a macrophage-derived IL-6-dependent pathway. *Cell Metab* **13**, 401-412 (2011).
231. R. J. Perry *et al.*, Leptin Mediates a Glucose-Fatty Acid Cycle to Maintain Glucose Homeostasis in Starvation. *Cell* **172**, 234-248.e217 (2018).
232. G. S. Cuendet, E. G. Loten, B. Jeanrenaud, A. E. Renold, Decreased basal, noninsulin-stimulated glucose uptake and metabolism by skeletal soleus muscle isolated from obese-hyperglycemic (ob/ob) mice. *J Clin Invest* **58**, 1078-1088 (1976).
233. A. Abulizi *et al.*, Membrane bound diacylglycerols explain the dissociation of hepatic insulin resistance from steatosis in MTTP(-/-) mice. *J Lipid Res* 10.1194/jlr.RA119000586 (2020).
234. J. P. Camporez *et al.*, ApoA5 knockdown improves whole-body insulin sensitivity in high-fat-fed mice by reducing ectopic lipid content. *J Lipid Res* **56**, 526-536 (2015).
235. H. Y. Lee *et al.*, Apolipoprotein CIII overexpressing mice are predisposed to diet-induced hepatic steatosis and hepatic insulin resistance. *Hepatology* **54**, 1650-1660 (2011).
236. D. F. Vatner *et al.*, Angptl8 antisense oligonucleotide improves adipose lipid metabolism and prevents diet-induced NAFLD and hepatic insulin resistance in rodents. *Diabetologia* **61**, 1435-1446 (2018).
237. H. Yagyu *et al.*, Lipoprotein lipase (LpL) on the surface of cardiomyocytes increases lipid uptake and produces a cardiomyopathy. *J Clin Invest* **111**, 419-426 (2003).
238. B. Thapa, K. Lee, Metabolic influence on macrophage polarization and pathogenesis. *BMB Rep* **52**, 360-372 (2019).
239. M. Valdearcos *et al.*, Microglial Inflammatory Signaling Orchestrates the Hypothalamic Immune Response to Dietary Excess and Mediates Obesity Susceptibility. *Cell Metab* **27**, 1356 (2018).